University of Alberta

Dynamics of Cosmic Strings in Black Hole Spacetimes

by

Jean-Pierre De Villiers

A thesis submitted to the Faculty of Graduate Studies and Research in partial fulfillment of the requirements for the degree of Doctor of Philosophy.

Department of Physics

Edmonton, Alberta
Fall 1998

National Library of Canada
Acquisitions and Bibliographic Services
395 Wellington Street
Ottawa ON K1A 0N4
Canada

Bibliothèque nationale du Canada
Acquisitions et services bibliographiques
395, rue Wellington
Ottawa ON K1A 0N4
Canada

Your file Votre référence

Our file Notre référence

The author has granted a non-exclusive licence allowing the National Library of Canada to reproduce, loan, distribute or sell copies of this thesis in microform, paper or electronic formats.

The author retains ownership of the copyright in this thesis. Neither the thesis nor substantial extracts from it may be printed or otherwise reproduced without the author's permission.

L'auteur a accordé une licence non exclusive permettant à la Bibliothèque nationale du Canada de reproduire, prêter, distribuer ou vendre des copies de cette thèse sous la forme de microfiche/film, de reproduction sur papier ou sur format électronique.

L'auteur conserve la propriété du droit d'auteur qui protège cette thèse. Ni la thèse ni des extraits substantiels de celle-ci ne doivent être imprimés ou autrement reproduits sans son autorisation.

0-612-34754-0

Canada

University of Alberta

Library Release Form

Name of Author: Jean-Pierre De Villiers

Title of Thesis: Dynamics of Cosmic Strings in Black Hole Spacetimes

Degree: Doctor of Philosophy

Year this Degree Granted: 1998

Permission is hereby granted to the University of Alberta to reproduce single copies of this thesis and to lend or sell such copies for private, scholarly, or scientific research purposes only.

The author reserves all other publication and other rights in association with the copyright in the thesis, and except as hereinbefore provided, neither the thesis nor any substantial portion thereof may be printed or otherwise reproduced in any material form whatever without the author's prior written permission.

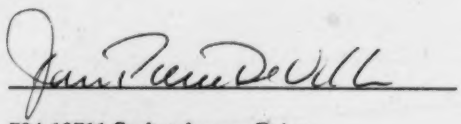

704-10711 Saskatchewan Drive
Edmonton, Alberta
T6E 4S4

October 2, 1998

University of Alberta

Faculty of Graduate Studies and Research

The undersigned certify that they have read, and recommend to the Faculty of Graduate Studies and Research for acceptance, a thesis entitled "Dynamics of Cosmic Strings in Black Hole Spacetimes" submitted by Jean-Pierre De Villiers in partial fulfillment of the requirements for the degree of Doctor of Philosophy.

Dr. V.P. Frolov, Supervisor

Dr. D. Hobill, External Examiner

Dr. H.-P. Kunzle

Dr. D.N. Page

Dr. J.C. Samson

Dr. R. Sydora

Abstract:

The gravitational interaction of a cosmic string with a black hole is studied by considering a scattering "experiment" where a straight cosmic string, initially at a great distance from a black hole of mass M and angular momentum $a = J/M$, approaches at some initial velocity v $(0 < v < c)$ and impact parameter b. Both numerical and analytical methods are used to study this problem. There are two possible outcomes, either the string is trapped by the black hole, or it is scattered. It is shown that, for the case where the string is scattered, the string is displaced towards the black hole, in the direction perpendicular to the velocity. The late-time solution is represented by a kink and anti-kink, propagating in opposite directions at the speed of light, and leaving behind them the string in a new "phase". String scattering data is also obtained in the case of strong-field scattering. When the string approaches the black hole at near-critical impact parameters, numerical results reveal that the string can partially wrap the black hole before being trapped, or scattering to infinity. The dynamics of the string are highly sensitive to initial data, and small changes in impact parameter affect the details of the final plunge of the cosmic string into a black hole. Near-critical scattering where the string manages to avoid capture gives rise to many transient phenomena while portions of the string dwell in the strong gravitational field near the event horizon of the black hole. The problem of string capture is further studied to determine the dependence of the capture impact parameter on initial velocity and is used to plot of a capture curve, $b(v)$. Motion of a captured string in the interior of a black hole is also discussed, and the final picture that emerges from this study is a comprehensive view of cosmic string dynamics over the full range of velocities and impact parameters.

Acknowledgement:

Numerical projects in General Relativity tend to consume a large amount of computing resources. This project could not have been undertaken without the co-operation of Dr. John Samson who kindly provided access to a Silicon Graphics Power Challenge computer on which a substantial amount of the numerical work for this project was carried out. Neither could this project have been completed without the help of the members of the University of Alberta cosmic string team, Shaun Hendy, Arne Larsen, and especially Valeri Frolov. For its continued financial support, the Natural Sciences and Engineering Research Council of Canada deserve special recognition for the NSERC undergraduate and post-graduate programs that have sustained me over the years.

Contents

1 Introduction 1
- 1.1 Organization of Thesis . . . 3
- 1.2 Notation . . . 4

2 Physics of Cosmic Strings and Black Holes 5
- 2.1 Cosmic Strings . . . 5
  - 2.1.1 Broken Symmetries . . . 6
  - 2.1.2 Topological Defects . . . 8
  - 2.1.3 Nielsen-Olesen Vortices . . . 8
  - 2.1.4 More General Cosmic String Solutions . . . 10
  - 2.1.5 The Nambu-Goto Action . . . 10
- 2.2 Black Holes . . . 11
  - 2.2.1 Spacetime of a Stationary Black Hole . . . 11
  - 2.2.2 Gravitational Scattering of Particles . . . 12

3 Motion of a Cosmic String in Curved Spacetime 15
- 3.1 Polyakov form of the Nambu-Goto Action and Equations of Motion . . . 16
- 3.2 Equations of Motion for String with Massive Particles at its Ends . . . 18
- 3.3 String Motion in a Weak Gravitational Field (non-rotating source) . . . 20
  - 3.3.1 Weak-Field Approximation . . . 20
  - 3.3.2 First-Order Corrections . . . 22
  - 3.3.3 Low-Velocity Limit . . . 25
- 3.4 Ultra-relativistic String Motion in a Weak Gravitational Field . . . 27
- 3.5 String Motion in a Weak Gravitational Field (rotating source) . . . 30
- 3.6 Numerical Schemes . . . 31
  - 3.6.1 Computational Grid . . . 32
  - 3.6.2 Discretization . . . 33
  - 3.6.3 Initial Data and Boundary Conditions . . . 33
  - 3.6.4 Role of Constraints . . . 34
- 3.7 Chapter Summary . . . 35

4 Gravitational Scattering of Cosmic Strings by a Black Hole **36**
4.1 Weak-field String Scattering by a Non-rotating Black Hole 37
4.1.1 Late-time Properties 39
4.1.2 Energy of Kinks 41
4.1.3 Comparison to Numerical Results 42
4.2 Strong-field Scattering by a Non-rotating Black Hole 43
4.3 Ultra-relativistic Scattering and Loop Formation 45
4.3.1 Condition for Loop Formation 47
4.3.2 String Self-intersection 48
4.4 Role of Tension - Dust String Model 49
4.5 Scattering by a Rotating Black Hole 51
4.5.1 Weak-field Scattering 51
4.5.2 Ultra-relativistic Scattering 53
4.5.3 Strong-field Scattering 53
4.6 Chapter Summary 54

5 Cosmic String Scattering at Near-Critical Impact Parameters **56**
5.1 Near-critical Scattering by a Non-rotating Black Hole 56
5.1.1 String Capture 59
5.1.2 String Winding Effect 59
5.2 Near-critical Scattering by a Rotating Black Hole 61
5.3 Chapter Summary 63

6 Capture of Cosmic Strings by a Black Hole **65**
6.1 Description of the Numerical Method 66
6.2 Cosmic String Capture by a Non-rotating Black Hole 67
6.2.1 Results from Numerical Scheme B 67
6.2.2 Results from Numerical Scheme A and Perturbative Calculations . . 69
6.3 Cosmic string Capture by a Rotating Black Hole 70
6.4 Chapter Summary 72

7 Motion of a Trapped String in the Black Hole Interior **74**
7.1 Description of the Numerical Method 74
7.2 Case of Non-rotating Black Hole 74
7.3 Case of Rotating Black Hole 75

8 Discussion **77**
8.1 Summary of Findings 77
8.2 Future Research 79

A Variational Calculations **86**
A.1 Variations on Interior Region 87
A.2 Variations on Boundary 89

B Discretization of the Equations of Motion and Constraints **92**
B.1 Von Neumann's Method - Linear Case 93
B.2 Vector-Matrix Notation for Equations of Motion 94
B.3 Discretization of the Derivatives 95
B.4 Handling the Non-linear Terms 96
B.4.1 Spatial non-linear term 96
B.4.2 Temporal non-linear term 98
B.5 Discretized Equations of Motion 99
B.5.1 Boundary Conditions 101
B.6 Discretization of the Constraints 101

C Coding Issues **103**
C.1 Overview of the Von Neumann Solver 103
C.2 Initializing Block Tridiagonal Matrices 105
C.2.1 Jacobian matrices 106
C.3 Christoffel Symbols and their Derivatives 109
C.4 Optimizations and Parallelization 109
C.5 Testing Accuracy and Longevity 111

D Metrics and Christoffel Symbols **113**
D.1 Minkowski Metric 113
D.1.1 Cartesian Coordinates 113
D.1.2 Spherical-Polar Coordinates 114
D.2 Schwarzschild Metric 114
D.2.1 Schwarzschild Coordinates 114
D.2.2 Eddington-Finkelstein Coordinates 115
D.2.3 Isotropic Coordinates 115
D.3 Kerr Metric 116
D.3.1 Boyer-Lindquist Coordinates 116
D.3.2 Kerr Coordinates 118

E Spacetime Coordinate Transformations **121**
E.1 Transformations for Schwarzschild and Boyer-Lindquist Coordinates 121
E.2 Transformations for Eddington-Finkelstein In-going Coordinates 122
E.3 Transformations for Kerr In-going Coordinates 122

List of Tables

4.1 Scattering Parameters - Schwarzschild Weak-field. 43
4.2 Scattering Parameters - Schwarzschild Strong-field. 44
4.3 Scattering Parameters - Schwarzschild Ultra-relativistic. 47
4.4 Scattering Parameters - Kerr Weak-field. 52
4.5 Scattering Parameters - Kerr Ultra-relativistic. 53
4.6 Scattering Parameters - Kerr Strong-field. 54

6.1 Comparison of Critical Impact Parameters - $v = 0.995c$ (Kerr). 72

List of Figures

1.1 Illustration of cosmic string scattering. 2
1.2 Cosmic String Scattering: Two-dimensional Parameter Space. 2

2.1 Temperature dependence of $V_T(\phi)$, $A = \eta = 1$ and $\lambda = 2$. 7
2.2 Gravitational Scattering of a Test Particle. 12
2.3 Effective potential in General Relativity. 13
2.4 Scattering for a Rotating Black Hole - Sense of Rotation. (North Pole, $\theta = 0$. is out of the page.) 14

3.1 Equations of Motion as a Map from Parameter Space to Spacetime. 16

4.1 $\chi_{(3)}$ perturbation. 37
4.2 $\chi_{(1)}$ perturbation. 38
4.3 $\chi_{(0)}$ and $\chi_{(2)}$ perturbations. 38
4.4 Reconstruction of perturbed string (Cartesian coordinates). 39
4.5 A straight cosmic string scattered by a Schwarzschild black hole. Weak-field case. 40
4.6 Time sequence of string scattering in weak-field regime (numerical results). Black hole lies at origin of coordinate system. Initial velocity, 0.76c, impact parameter 40 r_g. 43
4.7 Time sequence of string scattering in strong-field regime (numerical results). Black hole lies at origin of coordinate system. Initial velocity, 0.29c, impact parameter 2.5 r_g. 44
4.8 Breakdown of weak-field approximation. 45
4.9 Time sequence of string scattering in ultra-relativistic regime (numerical results). Black hole lies at origin of coordinate system. Initial velocity, 0.995c, impact parameter 4.0 r_g. 46
4.10 Time sequence of string scattering in ultra-relativistic regime (analytic). Black hole lies at origin of coordinate system. Initial velocity, 0.995c, impact parameter 4.0 r_g. 47
4.11 Loop formation region. 48
4.12 Time sequence of dust string scattering in ultra-relativistic regime. Black hole lies at origin of coordinate system. Left: Initial velocity, 0.995c, impact parameter 4.0 r_g. Right: Initial velocity, 0.76c, impact parameter 40 r_g. . . 50

4.13 $\chi_{(3)}$ perturbation. 51
4.14 Time sequence of string scattering in weak-field regime (numerical results). Kerr black hole lies at origin of coordinate system. Initial velocity, 0.76c, impact parameter $80M$. 52
4.15 Time sequence of string scattering in ultra-relativistic regime (numerical results). Black hole lies at origin of coordinate system. Initial velocity, 0.995c, impact parameter $8.0M$. 53
4.16 Time sequence of string scattering in strong-field regime (numerical results). Black hole lies at origin of coordinate system. Initial velocity, 0.29c, impact parameter $5.0M$. 54

5.1 Near-critical scattering for string and test particle. $v = 0.987c$ and $r_g = 1$. . 57
5.2 String worldsheet near $Z = 0$ plane, $v = 0.987c$. 58
5.3 String worldsheet at late proper time, $v = 0.987c$. Loops dissipate and kinks emerge. 59
5.4 Near-critical scattering for string at $\gamma = 10$, $v = 0.995c$. Impact parameters are $b = 2.579$, 2.580, 2.582, and 2.585, and $r_g = 1$. 60
5.5 Near-critical scattering for string and test particle. $v = 0.987c$, $r_g = 1$, and $a = +M/2$. Black hole rotation is counter-clockwise. 62
5.6 Near-critical scattering for string and test particle. $v = 0.987c$, and $a = -M/2$. Black hole rotation is clockwise. 63

6.1 Cosmic string capture curve for Schwarzschild black hole - data from numerical scheme B. 68
6.2 Cosmic string capture curve for Schwarzschild black hole - data from numerical scheme A and perturbative results. 70
6.3 Cosmic string capture curve for Kerr black hole - Ultra-relativistic data. . . 71
6.4 Cosmic string capture curve for Kerr black hole - non-relativistic data (preliminary). 72

7.1 Motion in interior of Schwarzschild Black Hole. $v = 0.987c$ and $b = 2M$. Axes are in dimensionless units X^i/M. 75
7.2 Motion in interior of Kerr and Schwarzschild Black Holes (equatorial plane). $v = 0.987c$ and $b = 2M$. 76

C.1 Scalability graph for SGI Power Challenge. 111
C.2 Accuracy of Solver. 111

List of Symbols:

General:

c	Speed of light
G	Universal gravitational constant

Co-ordinates/metrics:

x^μ	General spacetime co-ordinates
$g_{\mu\nu}$	Metric of general spacetime, signature $(-+++)$
$\eta_{\mu\nu}$	Metric of Minkowski spacetime, signature $(-+++)$
$\Gamma^\mu_{\rho\eta}$	Christoffel symbol
ζ^A	String worldsheet co-ordinates
G_{AB}	Induced metric on string worldsheet, signature $(-+)$

Black holes:

a	Specific angular momentum of a rotating (Kerr) black hole
φ	Newtonian gravitational potential
r_g	Gravitational radius (horizon) of Schwarzschild black hole
r_+	Event horizon of Kerr black hole
r_{static}	Static limit of Kerr black hole

Cosmic Strings:

μ	Linear mass density of cosmic string
b	Impact parameter for scattering
v	Initial velocity for scattering (measured at infinity)
X^μ	Equations of motion of straight string - Minkowski spacetime
$\mathcal{X}^\mu$	Equations of motion of straight string - general spacetime

Notation:

$\equiv$	Equivalent expressions
$:=$	Definition of special symbol
$\frac{\partial F}{\partial x^\mu} \equiv F_{,\mu} \equiv \partial_\mu F$	Equivalent expressions for partial derivatives

Chapter 1

Introduction

Cosmic strings are topological defects that are predicted by various grand-unified theories to have arisen in the early life of the universe. Cosmic strings are thought to have formed during cosmological phase transitions and their parameters, mass per unit length μ and thickness ρ, are determined by the energy that characterizes the phase transition. The earlier the transition, the greater the energy and hence the greater the parameters μ and ρ^{-1}. Cosmic strings formed at GUT-scale phase transitions, with a characteristic energy of $\sim 10^{15}$ GeV, are massive enough to have produced cosmologically significant effects. If such objects exist and persist in the portions of the universe that can be probed by scientific instruments, then a study of the interaction of cosmic strings with the constituents of galaxies and especially black holes is of considerable interest.

The study described here deals with the gravitational scattering and capture of cosmic strings by black holes. Cosmic strings are either infinite in length or they form closed loops. If the size of such a loop is much greater than the size of the black hole, as is expected for astrophysically realistic cases, then the portion of the loop of string that will interact with the black hole can be treated as part of an infinitely long and effectively straight cosmic string. For this reason, the straight-string approximation is used exclusively in this study.

The scattering of straight cosmic strings by a black hole bears some similarity to the scattering of test particles, which is well understood[1]. One important difference is that a cosmic string is an extended one-dimensional object with internal degrees of freedom that can be excited during scattering. For this reason, the detailed dynamics of string scattering by a black hole are expected to be far more complicated than for particle scattering. In order to describe the main features of string scattering, it is convenient to think of string scattering in terms of the two-dimensional parameter space of initial velocity (v) and impact parameter (b), where the initial velocity is the velocity of the string at large distance from the black hole (mass M and specific angular momentum $a = J/M$), and the impact parameter is perpendicular distance of the cosmic string relative to a line passing through the center of the black hole, as shown in Fig. 1.1 (some aspects of this figure will be discussed in more

[1]See Misner, Thorne, and Wheeler [40] or Frolov and Novikov [27] for a comprehensive survey and references to the literature.

detail in subsequent chapters).

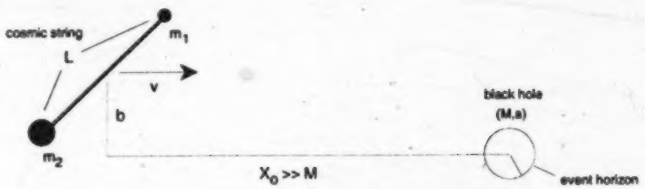

Figure 1.1: Illustration of cosmic string scattering.

The (b, v) parameter space of a string can be divided into a number of regions, as sketched in Fig. 1.2. The most basic division of the parameter space separates the regions of weak and strong gravitational fields. The **weak-field scattering region** is characterized by large impact parameters, where no part of the string ever strays close to the black hole. The strong field region is subdivided into two regions, depending on the fate of the cosmic string. The **strong-field scattering region** represents the range of parameters for which a string can come close to the black hole, yet still scatter to infinity. The **trapped region**, on the other hand, is the region of parameter space representing strings that are trapped by the black hole. The boundary between these two regions is known as the **capture curve**. The edges of parameter space represent various limiting cases: the **slow motion limit**, where $v \to 0$, the **Minkowski limit**, where $b \to \infty$, and the **ultra-relativistic limit**, where $v \to c$.

The study of string motion in the various regions of parameter space requires different approaches; the purpose of this thesis is to present the results of this study.

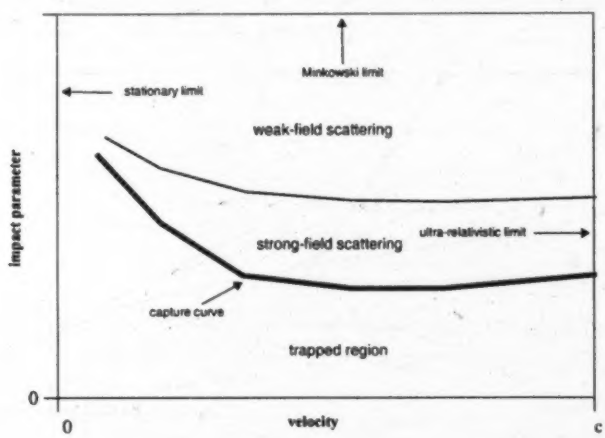

Figure 1.2: Cosmic String Scattering: Two-dimensional Parameter Space.

1.1 Organization of Thesis

The study of string scattering, at its fundamental level, involves finding solutions to the equations of motion of the string on a curved background. Analytic and/or numerical solutions have been derived for the various regions of parameter space discussed above; the numerical results, especially, are quite technical. In order to present results without cumbersome details, main physical results are emphasized in the body of the document, while details of derivations are deferred to a series of Appendices. The thesis is organized into the following chapters:

- **Overview of Cosmic String and Black Hole Physics** - A cursory review of the field-theoretic background required to postulate the existence of cosmic strings, combined with a brief review of physical properties of black holes and gravitational scattering.
- **Motion of a Cosmic String on a Curved Background** - The motion of a cosmic string in the spacetime of a black hole is governed by a set of coupled partial differential equations, the *equations of motion*. A perturbation method is developed that allows solving the equations of motion where the gravitational field is weak. This chapter also outlines the numerical schemes used to study string motion where perturbative methods break down.
- **Scattering of Cosmic Strings** - This chapter formulates the scattering problem for straight cosmic strings and describes the results of inelastic scattering by non-rotating and rotating black holes in the weak-field and strong-field regimes. The role played by string tension in determining the detailed dynamics of the scattering is also discussed.
- **Scattering at Near-Critical Impact Parameter** - A special case of scattering, deals with the scattering of strings with near-critical impact parameters that pass extremely close to the event horizon. Interesting dynamical effects are observed under these conditions that shed light on the capture of strings.
- **The Capture Curve** - The capture curve for the motion of straight strings in the gravitational field of non-rotating and rotating black holes is derived and discussed.
- **Motion in the Interior** - This chapter discusses the evolution in the interior of a black hole for the portion of the string that has been captured.
- **Summary of Findings** - Review of key results, including an outline of future work.
- **Appendices** - Provide supplementary details on the following topics: variational calculations (equations of motion), discretization of the equations of motion, implementation of numerical solvers, metrics for black hole spacetimes, and coordinate transformations.

Some portions of this thesis have been published previously. Material for some chapters has been adapted from:

1. De Villiers, J.P., *Dynamics of Cosmic Strings in Schwarzschild Spacetime.* Proceedings of Seventh Canadian Conference on General Relativity and Relativistic Astrophysics (Fall 1997). **gr-qc9706040.**

2. De Villiers, J.P., and Frolov, V.P., *Gravitational Capture of Cosmic Strings by a Black Hole.* To appear in Int. J. Mod. Phys. **D7** No. 6 (December 1998).

3. De Villiers, J.P., and Frolov, V.P., *Scattering of Straight Cosmic Strings by Black Holes: Weak Field Approximation.* To appear in Phys. Rev. **D58** No. 6 (October 1998).

4. De Villiers, J.P., and Frolov, V.P. *Gravitational Scattering of Cosmic Strings by Non-Rotating Black Holes.* (paper under preparation).

1.2 Notation

The equations presented in this thesis make implicit use of a few notational conventions.

- The sign conventions of Misner, Thorne, and Wheeler [40] for metric tensors and curvatures are followed in this thesis.
- Unless otherwise stated, natural units, where $G = c = 1$, are also used.
- In dealing with spacetime quantities, two types of indices are used: Greek indices (e.g. x^μ) take on the values $\mu = 0, 1, 2, 3$, and roman indices (e.g. x^i) take on the values $i = 1, 2, 3$. Indices related to the worldsheet of cosmic strings use the upper-case indices A or B (e.g. ζ^A) which take on the values $A, B = 0, 1$.
- The Einstein summation convention, whereby repeated covariant (lower) and contravariant (upper) indices are implicitly summed over, is used throughout. For instance,

$$g^{\nu\mu}\, g_{\rho\mu,\sigma} \equiv \sum_{\mu=0}^{3} g^{\nu\mu}\, g_{\rho\mu,\sigma}. \tag{1.1}$$

Chapter 2

Physics of Cosmic Strings and Black Holes

This chapter provides a cursory review of the field-theoretic concepts that are used to postulate the existence of cosmic strings, and the role of the Nambu-Goto action as the fundamental action for cosmic strings. This chapter also discusses the necessary concepts from black hole physics that are required to study motion of strings in black hole spacetimes.

2.1 Cosmic Strings

The currently held view is that our universe, after beginning its expansion, passed through a very hot, very dense state. The various grand-unified theories that have been put forward to explain how the universe evolved in the primordial seconds involve broken symmetries that can give rise to extended structures known as topological defects. For various reasons that will be touched upon in this chapter, linear topological defects are especially appealing for the role they may have played in galaxy formation. Cosmic strings were first discussed by Kibble [37] and first proposed by Zeldovich [55] and Vilenkin [49] as possible sources of density fluctuations in the primordial universe.

Cosmic strings (and other topological defects) are thought to have formed during cosmological phase transitions as the early universe expanded and cooled. In principle, cosmic strings can form at a number of phase transitions; however, only strings formed at GUT-scale phase transitions are capable of producing astrophysically significant gravitational effects. Strings formed at other, lower-energy phase transitions can give rise to many interesting (non-gravitational) effects [34], but their gravitational interactions are negligible.

In order to understand the nature of cosmic strings, field-theoretic concepts are required [46]. The modern physics of elementary particles is described in the language of gauge theories. Such theories feature broken symmetries, symmetries that can be restored at sufficiently high temperatures. It is assumed that the universe, after a possible stage of inflation and subsequent reheating, during which the main matter of the universe was created, began in an extremely hot, extremely dense and highly homogeneous state where

the fundamental interactions were unified under some large symmetry group. As the universe expanded and cooled, it passed through a sequence of critical temperatures at which a particular symmetry was broken. A broken symmetry can give rise to extended structures, topological defects, that can be sheet-like (domain walls), line-like (cosmic strings), or point-like (monopoles). Textures, which are three-dimensional structures, can also arise, as can hybrid defects, such as walls bounded by strings. The structural parameters of these defects are mainly determined by the energy characterising the cosmological phase transition.

In order to determine the suitability of a given topological defect in structure formation, there are some key considerations: the defects must be stable and they must have sufficient (but not excessive) energy density to perform this important astrophysical role. Not all topological defects are suitable candidates for accounting for structure formation. For instance, domain walls forming even at the relatively low energies of the electro-weak phase transition have been ruled out, as discussed by Kibble [38]. If such a structure were to have formed, it would dominate the mass of the universe. On the other hand, it is thought that cosmic strings, formed during a GUT-scale phase transition, and moving through the initially homogeneous matter could have given rise to the density fluctuations necessary to initiate the formation of galaxies.

A proper survey of the entire subject of cosmic strings is quite an undertaking. Fortunately, survey papers are available by Vilenkin [50] and Hindmarsh and Kibble [34]. More recently the monograph of Vilenkin and Shellard [52] provides a thorough exposition of the subject. What is required here is a cursory review expanding on some of the key points raised above, the main objective being to arrive at a low-energy effective action for cosmic strings. This effective action is the foundation upon which all calculations in this thesis are based.

2.1.1 Broken Symmetries

The motivation for the study of topological defects has its origins in the Higgs mechanism. Since it is believed that there is only one massless spin-1 particle in nature, the photon which mediates the electromagnetic interaction, a problem arises as soon as a gauge theory is formulated with a symmetric Lagrangian and symmetric vacuum states. The problem is that the gauge symmetries built into the Lagrangian are associated with massless spin-1 particles. So, any Lagrangian that contains symmetries that require the existence of such massless particles (other than the photon) must be "incorrect". The remedy is to give these other spin-1 particles a mass (i.e. making their interactions short-range). The Higgs mechanism introduces spin-0 (scalar) fields in a Lagrangian that transform non-trivially under the symmetry group of the Lagrangian and give the gauge particles a mass. This scalar field, denote it ϕ, takes on minima at non-zero values ($\phi_0 \neq 0$), and hence breaks the vacuum symmetry.

The symmetry breaking mechanism is associated with quantum field theories where the effective potential contains temperature-dependent terms ($V_T(\phi)$) . These temperature-dependent terms arise in developing the quantum field theory from a classical potential by perturbative expansion in powers of the Planck constant $\hbar$. The nature of the effective

potential fixes critical temperatures associated with symmetry breaking. In the cosmological context, these critical temperatures are associated with cosmological phase transitions.

How this comes about can be understood by a simple example. Taking the case of a scalar field theory (with complex scalar field ϕ) having the $U(1)$ symmetry (field invariant under transformation $\phi \to e^{i\alpha}\phi$), and temperature-dependent potential

$$V_T(\phi) = A T^2 \phi^* \phi + \frac{1}{2}\lambda\left(\phi^*\phi - \eta^2\right)^2 , \tag{2.1}$$

where $A > 0$ is assumed. At $T = 0$, the minima of this potential do not occur at $\phi = 0$ but rather describe a ring; this is an example of a broken symmetry since the vacuum expectation value of the field $\langle\phi\rangle = \eta e^{i\theta}$ is of a model-dependent amplitude (η) but arbitrary phase (θ); the vacuum is not invariant under the U(1) transformation (it maps the one vacuum state to another). The original $U(1)$ symmetry can be restored, however, given a suitably high temperature. How this comes about can be seen by rearranging the expression for the potential,

$$V_T(\phi) = \left(A T^2 - \lambda\eta^2\right)\phi^*\phi + \frac{\lambda}{2}\left((\phi^*\phi)^2 + \eta^4\right) \tag{2.2}$$

$$\equiv m^2(T)\,\phi^*\phi + \frac{\lambda}{2}\left((\phi^*\phi)^2 + \eta^4\right) , \tag{2.3}$$

where the critical temperature $T_c = (\lambda/A)^{1/2}\eta$ restores the potential minimum to $\phi = 0$, so that for $T \geq T_c$, the symmetry is restored and for $T < T_c$, the symmetry is broken. These cases are shown in Fig. 2.1.

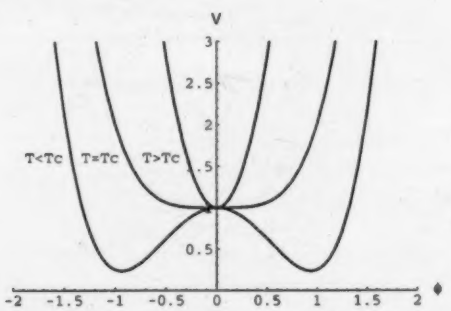

Figure 2.1: Temperature dependence of $V_T(\phi)$, $A = \eta = 1$ and $\lambda = 2$.

In this simple model, a phase transition would occur as the temperature dropped below the critical value T_c. This transition may generate topological defects in the vacuum. The study and classification of topological defects is systematic, and the general procedure is described in the next section.

2.1.2 Topological Defects

The investigation of topological defects in field theories involves a series of steps that establish the properties of the vacuum manifold and seek stable solutions for topological defects.

1. Write the Lagrangian for the field theory of interest;
2. Determine the symmetry group;
3. Find the minima of the potential and determine the structure of the vacuum manifold;
4. Characterize the types of topological defects (this requires knowledge of homotopy [42]);
5. Derive the field equations from the Lagrangian through the Euler-Lagrange equations, e.g. for a scalar field ϕ,

$$\frac{\partial L}{\partial \phi} - \partial_\mu \frac{\partial L}{\partial \left[\partial_\mu \phi\right]} = 0 \tag{2.4}$$

6. Compute solutions for the topological defects;
7. Compute the energy-momentum tensor of the field, e.g.

$$T_{\mu\nu} = \partial_\mu \phi \, \partial_\nu \phi - g_{\mu\nu} \, L \,, \tag{2.5}$$

   where $g_{\mu\nu}$ is the Minkowski metric, and from this the energy density (T_{00}) of the topological defect.

Most of the calculations in the above procedure are outside the scope of this document, and are covered in the reviews cited above. What is relevant here is that linear defects are predicted by a large number of field-theoretic models, and it is possible to formulate a common low-energy effective action for these string solutions, the Nambu-Goto action to be described shortly. Linear defects arise when the vacuum manifold M is not simply connected, containing unshrinkable loops. In the language of homotopy, a non-trivial first homotopy group, $\pi_1(M) \neq I$, is the condition for string formation. The first homotopy group counts the equivalence classes of loops in the manifold. To illustrate the above procedure, one of the simplest models leading to cosmic string solutions is discussed next.

2.1.3 Nielsen-Olesen Vortices

One of the simplest models leading to string solutions is that of the Nielsen-Olesen vortex [43] which can arise when a local (gauge) symmetry is broken. The Lagrangian of interest contains a complex scalar field (ϕ) and a gauge field (A_μ),

$$L = D_\mu \phi^* \, D^\mu \phi - \frac{1}{4} F_{\mu\nu} \, F^{\mu\nu} - \frac{1}{2} \lambda \left(\phi^* \, \phi - \eta^2 \right)^2 , \tag{2.6}$$

where $D_\mu = \partial_\mu + i\,g\,A_\mu$ and $F_{\mu\nu} = \partial_\mu A_\nu - \partial_\nu A_\mu$. The Lagrangian is invariant under the local $U(1)$ symmetry

$$\begin{aligned} \phi &\rightarrow e^{i\,\Lambda(x)}\,\phi, \\ A_\mu &\rightarrow A_\mu - \frac{1}{g}\,\partial_\mu\,\Lambda(x). \end{aligned} \tag{2.7}$$

The minima of the field occur when $\langle\phi_0\rangle = \eta\,e^{i\,\theta}$. The vacuum manifold, M, consists of points lying on the circle (S^1) of radius η. The vacuum manifold is not invariant under the action of the U(1) transformation for values of the rotation parameter that are not integer multiples of 2π. It is possible to construct arcs on the manifold, which are distinguished by their winding direction and the number of turns, so $\pi_1(M) = Z$, a non-trivial group. The general methods of homotopy predict the existence of strings (they also exclude domain walls and monopoles).

The string solutions begin with the derivation of the field equations for the scalar and gauge fields. The Euler-Lagrange equations yield,

$$\begin{aligned} D^2\,\phi + \lambda\,\phi\left(\phi^2 - \frac{\eta^2}{2}\right) &= 0, \\ \partial_\nu F^{\mu\nu} + ig\,(\phi^*\,D^\mu\phi - D^\mu\phi^*\,\phi) &= 0. \end{aligned} \tag{2.8}$$

Using cylindrical coordinates (ρ, ϕ, z), the radial gauge ($A_\rho = 0$), and making the ansatz that a straight string lying in the z-direction exists and is described by

$$\begin{aligned} \phi(\rho,\varphi,z) &= \frac{\eta}{\sqrt{2}}\,f\,(m_v\,\rho)\;e^{i\,n\,\varphi} \\ A^\varphi &= \frac{n}{g\rho}\,a\,(m_v\,\rho) \end{aligned} \tag{2.9}$$

reduces the field equations to two coupled non-linear ODEs for the radial function and angular functions. Here, $m_v = g\,\eta$ is the mass of the vector boson, $m_s = \sqrt{\lambda}\,\eta$ the mass of the scalar. Asymptotic solutions can be obtained [34] by assuming power-law and exponential dependence for f, the radial function, and a, the angular function, yielding the asymptotic solutions

$$f\,(\xi) = \begin{cases} f_0\,\xi^{|n|} & \text{for } \xi \rightarrow 0^+ \\ 1 - f_1\,\xi^{-1/2}e^{-\sqrt{\beta}\xi} & \text{for } \xi \rightarrow \infty \end{cases}, \tag{2.10}$$

and

$$a\,(\xi) = \begin{cases} a_0\,\xi^2 - \frac{|n|f_0^2}{4(|n|+1)}\xi^{2|n|+2} & \text{for } \xi \rightarrow 0^+ \\ 1 - a_1\,\xi^{1/2}e^{-\xi} & \text{for } \xi \rightarrow \infty \end{cases}, \tag{2.11}$$

where $\xi = m_v\rho$ and $\beta = \lambda/g^2 = \left(\frac{m_s}{m_v}\right)^2$, and n is a parameter known as the winding number.

The energy density (T_{00}) of the string can be computed as outlined above. The important observation here is that the energy density of the string solution is localized in the core of the string ($\mu \sim n^2\,\eta^2$). The radius of the string's core is given by the Compton wavelength of the scalar, $\rho_s \sim m_s^{-1}$ and the radius of the tube of magnetic flux is given by the Compton wavelength of the vector boson, $\rho_v \sim m_v^{-1}$.

2.1.4 More General Cosmic String Solutions

The above simple example can be expanded upon, taking under consideration more realistic field-theoretic models and their corresponding symmetry groups. The important fact for the present discussion is that plausible models featuring string solutions arising from a GUT-scale phase transition are possible. Although the above example dealt with an infinite string solution, strings forming closed loops are also possible. GUT-scale strings are characterized by a large energy density ($\mu \sim 10^{21}\, kg/m$) that is equal to their tension (disturbances on the strings propagate at the speed of light); their energy is also highly localized in a very thin core ($\rho \sim 10^{-31}\, m$).

If such strings exist, they form a random network permeating an expanding (Friedmann-Robertson-Walker) universe [52]. Infinite strings expand with the universe. Closed loops behave like infinite strings if their size is greater than the cosmological horizon; if they are smaller than the horizon, they collapse [49]. Loops of irregular shape oscillate and radiate gravitational waves. Strings can also self-interact and interact with other strings. When strings self-intersect or intersect other strings, they can split and reconnect. Consequently, the evolution of a large network of strings is a very complicated process.

In this study, the interaction of a string with a black hole of mass M involves a characteristic length scale (on the order of the event horizon of the black hole) that is exceedingly small when compared to the cosmological horizon size, or the radius of the loop of string. It is therefore possible to simplify matters considerably by treating the string as infinite. Also, the gravitational field created by the string can be neglected because the dimensionless parameter which characterizes the strength of the field $\mu^* = G\mu/c^2$ is negligibly small (for GUT-scale strings one has $\mu^* \sim 10^{-6}$). It means that the string is a test object moving in the background of a black hole metric. Furthermore, as discussed above, the radius of the core of the cosmic string is much less than any other parameters that enter the problem, such as the length of the string or the size of inhomogeneity of the gravitational field in which it is moving, so that one can idealize the motion of the string in the spacetime as a two-dimensional worldsheet. In order to describe this string mathematically, an effective action is required, and this issue is discussed next.

2.1.5 The Nambu-Goto Action

In astrophysically realistic situations the thickness of the string is small with respect to other length-related parameters and can be neglected. The string can be idealized as a one-dimensional line where the energy-momentum of the string is concentrated. In this approach, string motion is described by a two-dimensional surface in spacetime.

Starting with a field-theoretical description, one can derive the approximate equation for this two-dimensional surface. The corresponding analysis can be found in Vilenkin and Shellard [52], who demonstrate that the equations of motion of a cosmic string in the test string approximation follow from the Nambu-Goto action,

$$I = -\mu \int d^2\zeta \sqrt{-\det(G)}\,, \quad G_{AB} = g_{\mu\nu} \frac{\partial x^\mu}{\partial \zeta^A} \frac{\partial x^\nu}{\partial \zeta^B}\,, \tag{2.12}$$

where $g_{\mu\nu}$ is the spacetime metric, ζ^A denote the worldsheet coordinates ($A, B = 0, 1$; $\zeta^0 = \tau$, $\zeta^1 = \sigma$), and G_{AB} is the induced metric on the worldsheet of the string. A two-dimensional worldsheet which provides an extremum to the Nambu-Goto action is a minimal surface.

The thickness of the string and the small radius of curvature of its bending result in corrections to this action involving extrinsic curvature and terms of higher order in extrinsic curvature. These terms are neglected in this study[1].

2.2 Black Holes

Astrophysical black holes are the remnants of the collapse of massive stars, or the supermassive entities at the core of many galaxies. Black holes are dynamical objects; they can increase their mass by the capture of external material, through accretion of dust and plasmas from the neighbouring stars or the interstellar medium, or through coalescence (the capture of whole stars, neutron stars, or other black holes). Realistic black holes are highly complex systems. Theoretical models that are more amenable to study of these objects can be obtained from vacuum solutions to the Einstein field equations of General Relativity.

2.2.1 Spacetime of a Stationary Black Hole

The most general vacuum solution of the Einstein equations describing an isolated, stationary uncharged black hole was given by Kerr [36]. The Kerr metric, in Boyer-Lindquist coordinates (t, r, θ, ϕ) [12], has the form

$$\begin{aligned} ds^2 &= -\left(1 - \frac{2Mr}{\Sigma}\right) dt^2 - \frac{4aMr\sin^2\theta}{\Sigma}\, dt\, d\phi + \frac{\Sigma}{\Delta}\, dr^2 \\ &+ \Sigma\, d\theta^2 + \frac{A\sin^2\theta}{\Sigma}\, d\phi^2 , \end{aligned} \tag{2.13}$$

where

$$\begin{aligned} \Delta &:= r^2 - 2Mr + a^2 , \\ \Sigma &:= r^2 + a^2\cos^2\theta , \\ A &:= \left(r^2 + a^2\right)^2 - a^2\sin^2\theta\,\Delta , \end{aligned}$$

M is the mass of the black hole, and $a = J/M$ its specific angular momentum.

In this study, the Kerr solution will be applied to rotating black holes ($a \neq 0$) and also to non-rotating black holes ($a = 0$), where the above metric simplifies considerably (it reduces to the Schwarzschild solution; see Appendix D).

The properties of the Kerr and Schwarzschild solutions are discussed in many works, notably those of Misner, Thorne and Wheeler [40] and Frolov and Novikov [27]. For the present purposes, only a few basic facts about these objects need to be considered.

[1] Shellard and Vilenkin demonstrate that the Nambu-Goto action arises as the natural low-energy effective action for strings in a wide variety (if not in all cases) of field-theoretic models.

Schwarzschild (non-rotating) black holes are stationary (time-independent), spherically symmetric solutions to the Einstein equations and are characterized by an event horizon at

$$r_g = 2\,M. \tag{2.14}$$

Particles or photons crossing the event horizon cannot return to the exterior of the black hole and are quickly pulled to the central singularity (at $r = 0$) by the strong gravitational field in the interior of the black hole.

The Kerr solutions are also characterized by an event horizon at

$$r_+ = \left(M + \sqrt{M^2 - a^2}\right). \tag{2.15}$$

Kerr black holes also have ergosphere that extends outward from horizon up to static limit, the distance below which objects cannot avoid rotating with the black hole,

$$r_{static} = M + \sqrt{M^2 - a^2 \cos^2\theta}. \tag{2.16}$$

The static limit and the horizon coincide at the poles ($\theta = 0, \pi$) and $r_{static} = 2\,M$ in the equatorial plane ($\theta = \pi/2$).

2.2.2 Gravitational Scattering of Particles

Since the problem under study is that of gravitational scattering (and trapping) of cosmic strings, it is necessary to briefly review the simpler problem of particle scattering and record here some results that will be used later to provide a basis for discussing the results for strings.

The general picture of gravitational scattering is given in Fig. 2.2, where a particle of mass m approaches a massive object, of mass M ($M \gg m$), with an initial velocity v measured at infinity and a corresponding kinetic energy $E > 0$. The particle approaches the central mass at some initial impact parameter b, measured as shown in the illustration. Initial velocity can range from 0 to the speed of light, c. Although the detailed dynamics of the particle depend on the effective potential that characterises motion in the gravitational field of the central mass, the scattering problem can be characterised by the choice of initial velocity and impact parameter.

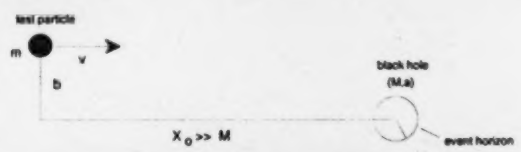

Figure 2.2: Gravitational Scattering of a Test Particle.

In Newtonian gravity, the scattering of test particles can be described in terms of hyperbolic (Keplerian) orbits of the particle about the central mass [31]. In General Relativity, where the central mass is taken to be a black hole, scattering is a far more interesting

process. Black holes, with their compact size and extreme surface gravity, have very special properties that make them unique and fascinating objects. In the context of gravitational scattering, black holes have a unique signature, in part due to their ability to trap objects that stray too close, and in part because particles can orbit the black hole many times before scattering to infinity (glory scattering, where the particle turns through an angle of 180^o, is a special case).

The effective potential of a black hole (see Chapter 25, [40]) has the form

$$\tilde{V}^2(r) = \left(1 - \frac{2M}{r}\right)\left(1 + \frac{\tilde{L}^2}{r^2}\right). \tag{2.17}$$

where $\tilde{L} = L/m$, the angular momentum per unit mass. Figure 2.3 shows a plot of $\tilde{V}(r)$. The figure shows that the potential has a long-range $1/r$ character and, for sufficiently large values of $\tilde{L}/M$, a contribution from the "centrifugal barrier", as in Newtonian gravity. However, the general relativistic character of the potential manifests itself at small r where the potential makes an abrupt downward turn.

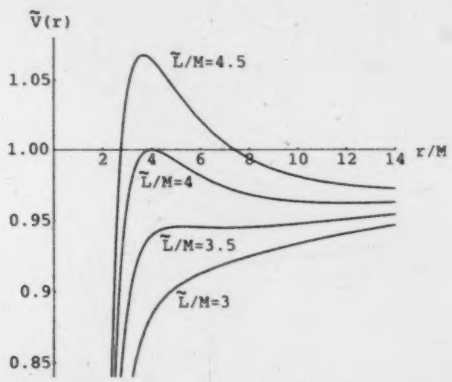

Figure 2.3: Effective potential in General Relativity.

This new feature of the potential has a drastic effect on the scattering problem. It is now possible for particles incident on the black hole with a given velocity v and impact parameter b to be trapped. Expressions can be derived for the critical impact parameter for capture of test particles [27]. For non-relativistic velocities,

$$b_{\text{capture}} = \frac{4M}{v}, \tag{2.18}$$

and for ultra-relativistic velocities ($v \to c$),

$$b_{\text{capture}} = 3\sqrt{3}\,M. \tag{2.19}$$

Similar expressions can be derived for the critical impact parameter in Kerr spacetime. However, the angular momentum of the black hole introduces an additional complication

in that the initial position of the string and the sense of rotation affect the value of the critical impact parameter. The sign convention for the rotation of a black hole is taken to be that of Misner, Thorne and Wheeler [40]; positive angular momentum denotes rotation in direction of increasing azimuthal angular coordinate ϕ. The particle can move in any one of the four quadrants shown in Fig. 2.4; however, there are only two possibilities: in the *retrograde* case (R), the particle approaches the black hole going "against" the sense of rotation; while in the *prograde* case (P), it approaches with the sense of rotation.

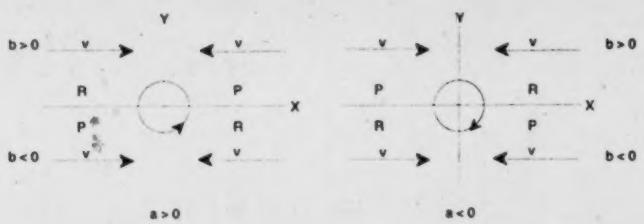

Figure 2.4: Scattering for a Rotating Black Hole - Sense of Rotation. (North Pole, $\theta = 0.$ is out of the page.)

For non-relativistic velocities [27], the critical impact parameter for a particle moving in the equatorial plane of the black hole is given by

$$b^{P}_{\text{capture}} \sim \frac{2M}{v}\left(1+\sqrt{1-\left|\frac{a}{M}\right|}\right) \tag{2.20}$$

for the prograde case, and

$$b^{R}_{\text{capture}} = \frac{2M}{v}\left(1+\sqrt{1+\left|\frac{a}{M}\right|}\right) \tag{2.21}$$

for the retrograde case. For ultra-relativistic velocities, again restricting to motion in the equatorial plane,

$$b^{P}_{\text{capture}} = \left(8\cos^3\left[\frac{1}{3}(\pi - \arccos\left|\frac{a}{M}\right|)\right] + \left|\frac{a}{M}\right|\right) M \tag{2.22}$$

for the prograde case, and,

$$b^{R}_{\text{capture}} = \left(8\cos^3\left[\frac{1}{3}\arccos\left|\frac{a}{M}\right|\right] - \left|\frac{a}{M}\right|\right) M \tag{2.23}$$

for the retrograde case.

Chapter 3

Motion of a Cosmic String in Curved Spacetime

This chapter[1] discusses the main analytical perturbative methods and numerical schemes that were used to obtain physical results concerning the motion of a straight cosmic string. The solution of the equations of motion of a cosmic string in the spacetime of a black hole is is a map from a two-dimensional parameter space to the four-dimensional spacetime manifold, as shown in Fig. 3.1. Solutions to these equations describe the world surface (or *worldsheet*) Σ of the string as functions $\mathcal{X}^\mu(\zeta^0,\zeta^1)$ of the string parameters $\zeta^A (A = 0, 1)$ conventionally taken as $(\zeta^0,\zeta^1) = (\tau,\sigma)$, where τ is a time-like parameter playing the role of proper time on the string and σ is a space-like parameter parametrizing points along the string.

The equations of motion can be derived from the Nambu-Goto action discussed in Chapter 2. For infinite cosmic strings, the equations of motion have been derived previously, and known analytic solutions to these equations deal mostly with stationary strings [29], [24], uniformly accelerated strings in Minkowski spacetime [28], or other special cases. Here, solutions to the equations of motion in weak gravitational fields were found using perturbative techniques, and numerical methods were used to study the motion of strings in strong gravitational fields, yielding a fairly comprehensive view of the dynamics of cosmic strings in the gravitational field of a black hole.

The derivation of the equations of motion, weak-field solutions, and the numerical scheme are the subjects of this chapter, with technical details deferred to the Appendices where necessary.

[1] Portions of this chapter have been previously published. Sections 3.1 and 3.3 are adapted from Ref. [22]. Sections 3.2 and 3.6 are adapted from Ref. [21]. Section 3.4 is adapted from Ref. [23].

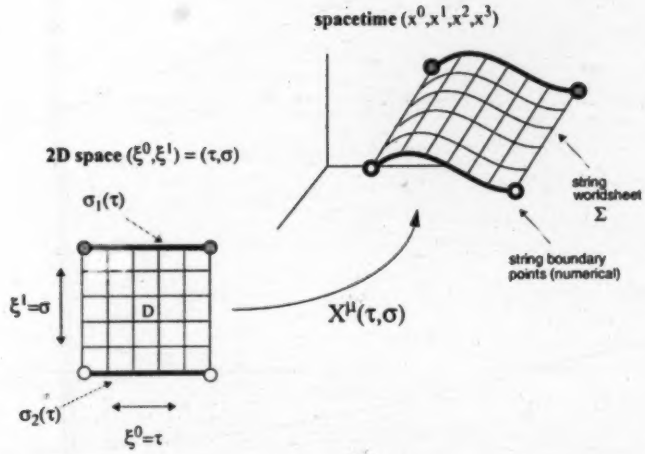

Figure 3.1: Equations of Motion as a Map from Parameter Space to Spacetime.

3.1 Polyakov form of the Nambu-Goto Action and Equations of Motion

As discussed in the previous chapter, the **Nambu-Goto action** (2.12) is the fundamental action for cosmic strings. Polyakov [45] writes the action for a relativistic string in the following equivalent form:

$$S[\mathcal{X}^\mu, h_{AB}] = -\mu \int d^2\zeta \sqrt{-h}\, h^{AB} G_{AB}\,, \tag{3.1}$$

where h_{AB} is the internal metric (with determinant h) of the two-dimensional parameter space of the string, G_{AB} is the induced metric (with determinant G) given by

$$G_{AB} = g_{\mu\nu}(\mathcal{X}^\lambda)\, \frac{\partial \mathcal{X}^\mu}{\partial \zeta^A}\, \frac{\partial \mathcal{X}^\nu}{\partial \zeta^B}\,, \tag{3.2}$$

and $g_{\mu\nu}(\mathcal{X}^\lambda)$ is the spacetime metric.

The Polyakov action is a quadratic action that introduces the additional freedom to extremize with respect to the internal metric, h_{AB}. Polyakov shows that this action is equivalent to the Nambu-Goto action in that they yield the same equations of motion; however, the Polyakov action is generally easier to manipulate and is used here.

To extremize the Polyakov action, the following variational expressions must hold. First, the variation with respect to $\mathcal{X}^\mu$, which yields the equations of motion, gives

$$\frac{\delta S[\mathcal{X}^\mu, h_{AB}]}{\delta \mathcal{X}^\mu} = \Box\, \mathcal{X}^\mu + \Gamma^\mu_{\rho\sigma}\, h^{AB}\, \mathcal{X}^\rho_{,A}\, \mathcal{X}^\sigma_{,B} = 0\,, \tag{3.3}$$

where,

$$\Box = \frac{1}{\sqrt{-h}}\partial_A\left(\sqrt{-h}\,h^{AB}\,\partial_B\right). \tag{3.4}$$

Second, the variation with respect to h_{AB}, which yields constraint equations, gives

$$\frac{\delta S\left[\mathcal{X}^\mu, h_{AB}\right]}{\delta h^{AB}} = G^{AB} - \frac{1}{2}h^{AB}\,G^C{}_C = 0, \tag{3.5}$$

where

$$G^C{}_C = h^{BC}\,G_{BC}. \tag{3.6}$$

The constraint equations are to be considered an auxiliary condition on the equations of motion.

In the equations of motion, the Christoffel symbols

$$\Gamma^\nu_{\rho\sigma} = \frac{1}{2}g^{\nu\mu}\left(g_{\rho\mu,\sigma} - g_{\sigma\rho,\mu} + g_{\mu\sigma,\rho}\right) \tag{3.7}$$

encode all the properties of the spacetime and the particular choice of coordinates (the Christoffel symbols contain the information on the gravitational influences felt by the cosmic string). There are potentially 40 different Christoffel symbols, but the actual number is reduced by symmetries of the spacetime and/or the coordinate system chosen (for instance, in flat spacetime with Cartesian coordinates, all Christoffel symbols are identically zero; for Schwarzschild black holes in the Schwarzschild (essentially spherical-polar) coordinates, there are 9 distinct non-zero Christoffel symbols).

To derive the equations of motion in the final form used in calculations, a choice of gauge must be made by using the allowed freedoms. Since any 2D Riemannian manifold is locally conformally flat [42], it is always possible (at least locally) to parametrize the 2-dimensional worldsheet using isothermal coordinates

$$h_{AB} = e^{2\,\gamma(\tau,\sigma)}\,\eta_{AB}. \tag{3.8}$$

For this choice of metric, the box operator reduces to the usual 2D wave operator, resulting in the following equations of motion:

$$\Box\mathcal{X}^\mu + \Gamma^\mu_{\rho\sigma}\left\{-\frac{\partial\mathcal{X}^\rho}{\partial\tau}\frac{\partial\mathcal{X}^\sigma}{\partial\tau} + \frac{\partial\mathcal{X}^\rho}{\partial\sigma}\frac{\partial\mathcal{X}^\sigma}{\partial\sigma}\right\} = 0. \tag{3.9}$$

where $\Box \equiv -\partial_\tau^2 + \partial_\sigma^2$. The equations of motion express the coordinates of the string in the target spacetime manifold; they can also be thought of as four coupled scalar field equations.

Applied to Eqn. (3.5), the metric (3.8) yields two constraints

$$\begin{aligned} G_{01} &= g_{\mu\nu}\frac{\partial\mathcal{X}^\mu}{\partial\tau}\frac{\partial\mathcal{X}^\nu}{\partial\sigma} = 0, \\ G_{00} + G_{11} &= g_{\mu\nu}\left(\frac{\partial\mathcal{X}^\mu}{\partial\tau}\frac{\partial\mathcal{X}^\nu}{\partial\tau} + \frac{\partial\mathcal{X}^\mu}{\partial\sigma}\frac{\partial\mathcal{X}^\nu}{\partial\sigma}\right) = 0. \end{aligned} \tag{3.10}$$

These equations can be interpreted as orthogonality conditions on the tangent vectors to the worldsheet, $\zeta^\mu_{(\tau)} = \partial_\tau\mathcal{X}^\mu$ and $\zeta^\mu_{(\sigma)} = \partial_\sigma\mathcal{X}^\mu$.

The imposition of boundary conditions to truncate the string to a finite length suitable for numerical solution will be discussed in Section 3.6.

3.2 Equations of Motion for String with Massive Particles at its Ends

Sometimes, especially in numerical studies where boundary conditions require special care, it is convenient to consider a finite open string with massive particles at its ends. It is possible to extend the Nambu-Goto action (2.12) to include massive end points by adding to the free string action the action for two free particles (see, e.g. Barbashov [7], Barbashov and Chervyakov [8], [9]), as follows:

$$S[\mathcal{X}^\mu, \sigma_i] = -\int_{\tau_1}^{\tau_2} d\tau \left(\mu \int_{\sigma_1(\tau)}^{\sigma_2(\tau)} d\sigma \sqrt{-G} + \sum_{i=1}^{2} m_i \sqrt{\left(\frac{d\mathcal{X}_\mu(\tau, \sigma_i(\tau))}{d\tau} \right)^2} \right), \tag{3.11}$$

where the end points of the string move in the (τ, σ) plane according to the functions $\sigma_i(\tau)$, $i = 1, 2$ (see Fig. 3.1). The above action functional consists of three distinct "pieces", a functional for the string interior (the free string action) and functionals for each massive end point. Barbashov shows that the variation of the action functional with respect to σ_i does not lead to new equations of motion and that, therefore, the σ_i are not dynamical variables. This finding allows a simple choice to be made for these boundary functions. How this simplification applies to the case for arbitrary spacetimes will need to be established.

The Polyakov action for a free string (3.1) is similarly extended to include massive end points,

$$\begin{aligned} S[\mathcal{X}^\mu, h_{AB}, \sigma_i] &= -\mu \int_{\tau_1}^{\tau_2} d\tau \int_{\sigma_1(\tau)}^{\sigma_2(\tau)} d\sigma \sqrt{-h}\, h^{AB} G_{AB} \\ &\quad - \sum_{i=1}^{2} \frac{m_i}{2} \int_{\lambda_1(\tau)}^{\lambda_2(\tau)} d\lambda\, g_{\mu\nu} \frac{dX_i^\mu}{d\lambda} \frac{dX_i^\nu}{d\lambda}, \end{aligned} \tag{3.12}$$

where $X_i^\mu(\tau) = \mathcal{X}^\mu(\tau, \sigma_i(\tau))$ is a world-line of the i-particle, m_i is its mass, and $\lambda = \lambda(\tau)$ is the most general parametrization for X_i^μ on the boundaries, from which

$$\frac{dX_i^\mu}{d\lambda} = \left(\frac{\partial X_i^\mu}{\partial \tau} + \frac{\partial X_i^\mu}{\partial \sigma} \dot{\sigma}_i(\tau) \right) \dot{\lambda}^{-1}. \tag{3.13}$$

Using Eqn. (3.13), it is possible to rewrite Eqn. (3.12) as

$$\begin{aligned} S[\mathcal{X}^\mu, h_{AB}, \sigma_i] &= -\mu \int_{\tau_1}^{\tau_2} d\tau \int_{\sigma_1(\tau)}^{\sigma_2(\tau)} d\sigma \sqrt{-h}\, h^{AB} G_{AB} \\ &\quad - \sum_{i=1}^{2} \frac{m_i}{2} \int_{\tau_1}^{\tau_2} d\tau\, g_{\mu\nu} \left[\frac{\partial X_i^\mu}{\partial \tau} + \frac{\partial X_i^\mu}{\partial \sigma} \dot{\sigma}_i \right] \left[\frac{\partial X_i^\nu}{\partial \tau} + \frac{\partial X_i^\nu}{\partial \sigma} \dot{\sigma}_i \right] \dot{\lambda}^{-1} \\ &\equiv S_{string} + \sum_{i=1}^{2} S_i. \end{aligned} \tag{3.14}$$

In order to obtain the most general equations possible, it will be assumed that the extremizing functions for the free string action are not prescribed on the σ boundaries (however, the extremizing functions are assumed to vanish on the τ boundaries). When the variations are computed, this means that the equations of motion of the massive end points receive contributions from both the string action and the particle action, effectively coupling the two objects.

To extremize this action, the following variational expressions must hold on the world-sheet interior Σ (where $\tau_1 \leq \tau \leq \tau_2$, and $\sigma_1 < \sigma < \sigma_2$)[2],

$$\frac{\delta S_{string}}{\delta \mathcal{X}^\mu} = \Box \mathcal{X}^\mu + \Gamma^\mu_{\rho\sigma} h^{AB} \mathcal{X}^\rho_{,A} \mathcal{X}^\sigma_{,B} = 0, \tag{3.15}$$

$$\frac{\delta S_{string}}{\delta h_{AB}} = G^{AB} - \frac{1}{2} h^{AB} G^C{}_C = 0, \tag{3.16}$$

where the definitions given in the previous section apply.

As mentioned above, the equations motion of the boundary points receive contributions from the $\mathcal{X}^\mu$ variation of the free string action S_{string} on the boundary, and the X_i^μ variation of the particle actions S_i. The expressions obtained from the variations are quite cumbersome and are shown in Appendix A. It is shown there that the boundary functions can be taken to be constants, allowing the choice of $\sigma_i = \pm\pi/2$ to be made on the boundaries, and $-\pi/2 < \sigma < \pi/2$ for the interior. Also, under the assumption that the massive particles are very massive, $m_i \to \infty$, the boundary terms yield the following equations of motion for the massive end points of the truncated string:

$$\frac{d^2 X_i^\mu}{d\lambda^2} + \Gamma^\mu_{\rho\eta} \frac{dX_i^\rho}{d\lambda} \frac{dX_i^\eta}{d\lambda} = 0. \tag{3.17}$$

Further, conditions are obtained on the parametrization $\lambda(\tau)$ leading to the identification of the time parameters $\lambda(\tau) \equiv \tau$. This equation is a familiar result: it is the equation of motion for a test particle with λ an affine parameter.

To summarize, the complete set of equations of motion of a cosmic string with infinitely massive end points in an arbitrary spacetime are given by

$$\Box \mathcal{X}^\mu + \Gamma^\mu_{\rho\sigma} \left\{ -\frac{\partial \mathcal{X}^\rho}{\partial \tau} \frac{\partial \mathcal{X}^\sigma}{\partial \tau} + \frac{\partial \mathcal{X}^\rho}{\partial \sigma} \frac{\partial \mathcal{X}^\sigma}{\partial \sigma} \right\} = 0; \left(-\frac{\pi}{2} < \sigma < \frac{\pi}{2}\right), \tag{3.18}$$

$$\frac{d^2 X_i^\mu}{d\tau^2} + \Gamma^\mu_{\rho\eta} \frac{dX_i^\rho}{d\tau} \frac{dX_i^\eta}{d\tau} = 0; \sigma_i = \pm\frac{\pi}{2}. \tag{3.19}$$

The constraint equations read

$$g_{\mu\nu} \left[\frac{\partial \mathcal{X}^\mu}{\partial \tau} \frac{\partial \mathcal{X}^\nu}{\partial \tau} + \frac{\partial \mathcal{X}^\mu}{\partial \sigma} \frac{\partial \mathcal{X}^\nu}{\partial \sigma} \right] = 0, \tag{3.20}$$

$$g_{\mu\nu} \left[\frac{\partial \mathcal{X}^\mu}{\partial \tau} \frac{\partial \mathcal{X}^\nu}{\partial \sigma} \right] = 0.$$

[2]The results for the h_{AB} and $\mathcal{X}^\mu$ variations for the interior of the string are identical to the results for the open string, but here the domain of the equations is no longer infinite, but is bounded by the end point functions, $\sigma_i(\tau)$.

3.3 String Motion in a Weak Gravitational Field (non-rotating source)

This section discusses the motion of a straight cosmic string in a weak static gravitational field using perturbative methods developed in [22]. The perturbative approach treats the weak-field solution to the equations of motion as a correction to a solution on a flat background,

$$\mathcal{X}^\mu(\tau,\sigma) = X^\mu(\tau,\sigma) + \delta X^\mu(\tau,\sigma)\,, \tag{3.21}$$

where X^μ is the background solution, and δX^μ is the correction.

In the absence of the external gravitational field $g_{\mu\nu} = \eta_{\mu\nu}$, where $\eta_{\mu\nu}$ is the flat spacetime metric. In this case, the equations of motion have easy solutions. Taking Cartesian coordinates (T, X, Y, Z), where all Christoffel symbols are zero, it can be shown by direct computation that

$$X^\mu(\tau,\sigma) = (\cosh(\beta)\,\tau, \sinh(\beta)\,\tau + X_0, Y_0, \sigma) \tag{3.22}$$

satisfies the equations of motion (3.9) and the constraints (3.10). The solution describes the motion of a straight string oriented along the Z axis, and moving parallel to the X axis at velocity $v = \tanh\beta$. Initially, at $\tau_0 = 0$, the string is found at $X^\mu(0,\sigma) = (0, X_0, Y_0, \sigma)$, with Y_0 playing the role of impact parameter, $Y_0 \equiv b$. For definiteness we choose $Y_0 > 0$ and $X_0 < 0$, so that $\beta > 0$.

It is convenient to introduce an orthogonal tetrad $e^\mu_{(m)}$ $(m = 0,1,2,3)$ connected with the world-plane of the background solution

$$e^\mu_{(0)} = X^\mu_{,\tau} = (\cosh\beta, \sinh\beta, 0, 0)\,, \quad e^\mu_{(1)} = X^\mu_{,\sigma} = (0,0,0,1)\,, \tag{3.23}$$

$$e^\mu_{(2)} = n^\mu_{(2)} = (\sinh\beta, \cosh\beta, 0, 0)\,, \quad e^\mu_{(3)} = n^\mu_{(3)} = (0,0,1,0)\,. \tag{3.24}$$

The first two unit vectors $X^\mu_{,A}$ are tangent to the world-sheet of the string, while the other two $n^\mu_{(R)}$ $(R = 2,3)$ are orthogonal to it. In order to avoid confusion, tetrad indices will be distinguished from spacetime indices by enclosing them in parentheses, (m). It is easy to verify that the induced metric G_{AB} on the world-sheet of the string is of the form

$$G_{AB} = \overset{0}{G}_{AB} = \eta_{AB}\,. \tag{3.25}$$

3.3.1 Weak-Field Approximation

The background solution is expressed in Cartesian coordinates. To treat the Schwarzschild black hole as a source of perturbations on this background isotropic coordinates (T, X, Y, Z) are used, for which the line element of Schwarzschild spacetime is

$$ds^2 = -\frac{(1 - M/2R)^2}{(1 + M/2R)^2}\,dT^2 + \left(1 + \frac{M}{2R}\right)^4 \left(dX^2 + dY^2 + dZ^2\right)\,, \tag{3.26}$$

where $R^2 := X^2 + Y^2 + Z^2$. This metric is of the form

$$ds^2 = -(1-2\Phi)dT^2 + (1+2\Psi)(dX^2 + dY^2 + dZ^2) \tag{3.27}$$

with

$$\Phi := \frac{\varphi}{(1+\frac{1}{2}\varphi)^2}, \quad \Psi := \varphi + \frac{3}{4}\varphi^2 + \frac{1}{4}\varphi^3 + \frac{1}{32}\varphi^4, \tag{3.28}$$

and φ is the Newtonian potential, $\varphi = M/R$.

In what follows it is assumed that this potential is small and, therefore, it is possible to write[3]

$$\Phi = \overset{1}{\phi} + \overset{2}{\phi} + \ldots = \varphi + a\varphi^2 + \mathcal{O}\left(\varphi^3\right), \quad \Psi = \overset{1}{\psi} + \overset{2}{\psi} + \ldots = \varphi + b\varphi^2 + \mathcal{O}\left(\varphi^3\right), \tag{3.29}$$

where

$$a = -1, \quad b = \frac{3}{4}. \tag{3.30}$$

A string moving far from the black hole is moving in the perturbed metric

$$g_{\mu\nu} = \eta_{\mu\nu} + \gamma_{\mu\nu}, \quad \gamma_{\mu\nu} = \overset{1}{\gamma}_{\mu\nu} + \overset{2}{\gamma}_{\mu\nu} + \mathcal{O}\left(\varphi^3\right), \tag{3.31}$$

$$\overset{1}{\gamma}_{\mu\nu} = 2\varphi\,\delta_{\mu\nu}, \quad \overset{2}{\gamma}_{\mu\nu} = 2\varphi^2\,\pi_{\mu\nu}, \quad \pi_{\mu\nu} = a\delta^0_\mu\delta^0_\nu + b\delta^i_\mu\delta^j_\nu\delta_{ij}. \tag{3.32}$$

Here $i, j = 1, 2, 3$ and δ_{ij} is the Kronecker δ-symbol.

The perturbation, $\gamma_{\mu\nu}$, of the metric results in the perturbations δX^μ and δh_{AB} of the flat-spacetime string solution (3.22). The equations describing these perturbations can be obtained by perturbing string equations (3.3) and (3.5). For this purpose decompose the perturbation of the string, using the orthogonal tetrad (3.23) and (3.24), as

$$\delta X^\mu = \chi^{(m)} e^\mu_{(m)} = \chi^{(R)} n^\mu_{(R)} + \chi^{(A)} X^\mu_{,A}, \tag{3.33}$$

where the four scalar functions of two variables, $\chi^{(m)}(\tau, \sigma)$, describe the deflection of the string world-sheet from the plane (3.22). The perturbations $\chi^{(0)}$ and $\chi^{(3)}$ describe perturbations along the tangent vectors of the string worldsheet Σ, denote these the longitudinal fields. The perturbations $\chi^{(1)}$ and $\chi^{(2)}$ describe perturbations perpendicular to Σ, denote these the transverse fields. As was done earlier, expand $\chi^{(m)} = \overset{1}{\chi}{}^{(m)} + \overset{2}{\chi}{}^{(m)} + \ldots$ in powers of φ, and also use the expansion of the internal metric h_{AB}

$$h_{AB} = \eta_{AB} + \overset{1}{h}_{AB} + \overset{2}{h}_{AB} + \ldots. \tag{3.34}$$

The first-order corrections will be treated next and applied to the general scattering problem. Second-order corrections will be discussed in section 3.3.3 to obtain the low-velocity behaviour of strings.

[3]The same form (3.27) of the metric is valid for the charged black hole (with charge Q). For the Reissner-Nordstrom metric describing such a black hole, one has $1 - 2\Phi = (1 + \varphi + q\varphi^2)^{-2}(1 - q\varphi^2)^2$, $1 + 2\Psi = (1 + \varphi + q\varphi^2)^2$, $q = 1 - (Q/M)^2$. For this metric, the expansion (3.29) is also valid with $a = \frac{1}{2}(q-3)$, $b = \frac{1}{4}(q+2)$.

3.3.2 First-Order Corrections

This section considers effects that are of the first order in φ only. The first-order effects on the constraint equations are considered first to obtain gauge fixing conditions, followed by first-order effects on the equations of motion, then by solutions using Green's function methods.

Constraint Equations

The induced metric is

$$G_{AB} = \eta_{AB} + \overset{1}{\gamma}_{AB} + 2\overset{1}{\chi}_{(A,B)}\,, \tag{3.35}$$

where

$$\overset{1}{\gamma}_{AB} = \overset{1}{\gamma}_{\mu\nu} X^{\mu}_{,A} X^{\nu}_{,B} = 2\varphi\ \mathrm{diag}(1 + 2\sinh^2\beta, 1)\,. \tag{3.36}$$

The perturbation of the constraint equation (3.5) has the form

$$\overset{1}{\gamma}_{AB} + 2\overset{1}{\chi}_{(A,B)} - \overset{1}{h}_{AB} - Q\eta_{AB} = 0\,, \tag{3.37}$$

where

$$Q := \frac{1}{2}\eta^{CD}\left[\overset{1}{h}_{CD} + \overset{1}{\gamma}_{CD} + 2\overset{1}{\chi}_{(C,D)}\right]. \tag{3.38}$$

One can always choose

$$\overset{1}{h}_{AB} = \overset{1}{h}\,\eta_{AB}\,. \tag{3.39}$$

so that,

$$\overset{1}{\gamma}_{AB} + 2\overset{1}{\chi}_{(A,B)} - \frac{1}{2}\eta_{AB}\eta^{CD}\left[\overset{1}{\gamma}_{CD} + \overset{1}{\chi}_{C,D}\right] = 0\,. \tag{3.40}$$

Using Eqn. (3.36), it follows that

$$\overset{1}{\chi}_{0,\tau} + \overset{1}{\chi}_{1,\sigma} = -2\varphi\cosh^2\beta\,, \quad \overset{1}{\chi}_{0,\sigma} + \overset{1}{\chi}_{1,\tau} = 0\,. \tag{3.41}$$

In what follows these are chosen to be the gauge fixing conditions.

Equations of Motion

The perturbation of the dynamical equation (3.3) is now considered. First, note that Eqn. (3.39) implies that $\sqrt{-h}h^{AB}$ is equal to η^{AB} up to the terms which are quadratic in φ. As a result, the equations of motion (3.9) can be decomposed as

$$\Box\mathcal{X}^{\mu} + h^{AB}\Gamma^{\mu}_{\alpha\beta}X^{\alpha}_{,A}X^{\beta}_{,B} \approx \Box X^{\mu} + e^{\mu}_{(m)}\,\Box\overset{1}{X}{}^{(m)} + \eta^{AB}\,\overset{1}{\Gamma}{}^{\mu}_{\alpha\beta}X^{\alpha}_{,A}X^{\beta}_{,B} = 0 \tag{3.42}$$

from which it follows that the first-order corrections must satisfy

$$\Box\overset{1}{X}_{(m)} + \eta^{AB}\,\overset{1}{\Gamma}_{\mu,\alpha\beta}\,X^{\alpha}_{,A}X^{\beta}_{,B}\,e^{\mu}_{(m)} = 0\,. \tag{3.43}$$

In these equations,

$$\overset{1}{\Gamma}_{\mu,\alpha\beta} = \frac{1}{2}(\overset{1}{\gamma}_{\mu\alpha,\beta} + \overset{1}{\gamma}_{\mu\beta,\alpha} - \overset{1}{\gamma}_{\alpha\beta,\mu}) = \varphi_{,\alpha}\delta_{\mu\beta} + \varphi_{,\beta}\delta_{\mu\alpha} - \varphi_{,\mu}\delta_{\alpha\beta}\,. \tag{3.44}$$

Dynamical equation (3.43) has the form

$$\Box\overset{1}{X}_{(m)} = \overset{1}{f}_{(m)}\,, \tag{3.45}$$

The components $f_{(A)}$ describe longitudinal perturbations of the straight string[4]. The components $f_{(R)}$ describe transverse perturbations of the straight string under the action of the external gravitational force $\overset{1}{f}_{(R)}$. To calculate $\overset{1}{f}_{(R)}$, note that

$$\overset{1}{f}_{(m)} = \overset{1}{K}_{\mu}\,e^{\mu}_{(m)}\,, \tag{3.47}$$

$$\overset{1}{K}_{\mu} = -\eta^{AB}\,\overset{1}{\Gamma}_{\mu,\alpha\beta}\,X^{\alpha}_{,A}X^{\beta}_{,B}$$

$$= \cosh^2\beta\,\overset{1}{\Gamma}_{\mu,00} + 2\sinh\beta\cosh\beta\,\overset{1}{\Gamma}_{\mu,01} + \sinh^2\beta\,\overset{1}{\Gamma}_{\mu,11} - \overset{1}{\Gamma}_{\mu,33}\,. \tag{3.48}$$

Simple calculations give

$$\overset{1}{K}_{\mu} = -2\sinh^2\beta\,\varphi_{,\mu} + 2\sinh\beta\cosh\beta\,\varphi_{,1}\delta^{0}_{\mu} + 2\sinh^2\beta\,\varphi_{,1}\delta^{1}_{\mu} - 2\varphi_{,3}\delta^{3}_{\mu}\,. \tag{3.49}$$

Using these results it is easily shown that

$$\overset{1}{f}_{(0)} = 2\sinh\beta\cosh^2\beta\,\varphi_{,X}\,, \qquad \overset{1}{f}_{(1)} = -2\cosh^2\beta\,\varphi_{,Z}\,, \tag{3.50}$$

$$\overset{1}{f}_{(2)} = 2\sinh^2\beta\cosh\beta\,\varphi_{,X}\,, \qquad \overset{1}{f}_{(3)} = -2\sinh^2\beta\,\varphi_{,Y}\,, \tag{3.51}$$

---

[4]Since longitudinal fields $\overset{1}{X}_{(A)}$ are already fixed by the gauge fixing condition it is necessary to verify that Eqns. (3.43) for $m = A$ are identically satisfied for this choice and do not give additional restrictions. For this purpose, it is noted that

$$\overset{1}{\Gamma}_{\mu,\alpha\beta}\,X^{\alpha}_{,A}X^{\beta}_{,B}X^{\mu}_{,C} = \frac{1}{2}(\overset{1}{\gamma}_{AC,B} + \overset{1}{\gamma}_{BC,A} - \overset{1}{\gamma}_{AB,C})\,. \tag{3.46}$$

By using this relation and Eqn. (3.40) it is easy to verify that Eqns. (3.43) are satisfied identically for $m = A$.

Solutions

Equation (3.45) for string propagation in a weak gravitational field can be easily solved. The retarded Green's function for the 2D $\Box$-operator is [10]

$$G_0\left(\sigma,\tau \mid \sigma',\tau'\right) = \frac{1}{2}\,\Theta(\tau-\tau'-\mid \sigma-\sigma' \mid)\,. \tag{3.52}$$

Using this Green's function a solution of Eqn. (3.45) can be written in the form[5] [41]

$$\chi_{(m)}(\tau,\sigma) = \chi^0_{(m)}(\tau,\sigma) + \chi^+_{(m)}(\tau+\sigma) + \chi^-_{(m)}(\tau-\sigma)\,, \tag{3.53}$$

where

$$\chi^0_{(m)}(\tau,\sigma) = -\int_{\tau_0}^{\tau} d\tau' \int_{-\infty}^{\infty} d\sigma' G_0\left(\sigma,\tau \mid \sigma',\tau'\right) f_{(m)}(\tau',\sigma')$$

$$= -\frac{1}{2}\int_{\tau_0}^{\tau} d\tau' \int_{\sigma-(\tau-\tau')}^{\sigma+\tau-\tau'} d\sigma' f_{(m)}(\tau',\sigma') \tag{3.54}$$

is a solution of inhomogeneous equation and $\chi^{\pm}_{(m)}$ are solutions of homogeneous equation which are fixed by the initial data

$$\chi_{(m)}(\tau_0,\sigma) = \chi^+_{(m)}(\tau_0+\sigma)+\chi^-_{(m)}(\tau_0-\sigma)\,, \quad \dot{\chi}_{(m)}(\tau_0,\sigma) = \dot{\chi}^+_{(m)}(\tau_0+\sigma)+\dot{\chi}^-_{(m)}(\tau_0-\sigma)\,. \tag{3.55}$$

Consider first the perturbation perpendicular to the direction of motion (the Y-direction), which is described by $\chi_{(3)}$. Assume that initially (at the infinite past) $\chi_{(3)} = 0$, that is, the straight string starts its motion ($\tau = 0$) at a very large, negative X_0 with initial conditions,

$$\chi_{(3)}(0,\sigma) = \dot{\chi}_{(3)}(0,\sigma) = 0\,, \tag{3.56}$$

and the solution has the form[6]

$$\chi_{(3)}(\tau,\sigma) = -M\sinh\beta\,\left[H_+(\tau,\sigma) + H_-(\tau,\sigma)\right]\,, \tag{3.57}$$

where

$$\begin{aligned} H_{\pm}(\tau,\sigma) &= \arctan\left[\frac{Y_0^2 + (X_0+\tau\,\sinh\beta)\,(X_0+s_{\pm}\,\sinh\beta)}{Y_0\,\sinh\beta\,R(\tau,\sigma)}\right] \\ &- \arctan\left[\frac{X_0\,(X_0+s_{\pm}\,\sinh\beta)+Y_0^2}{Y_0\,\sinh\beta\sqrt{\rho^2+s_{\pm}^2}}\right]. \end{aligned} \tag{3.58}$$

where the following notation was introduced,

$$R^2(\tau,\sigma) = (X_0+\tau\sinh\beta)^2 + Y_0^2 + \sigma^2\,, \quad \rho^2 = X_0^2+Y_0^2\,, \quad s_{\pm} = \tau\pm\sigma\,. \tag{3.59}$$

[5]Since only first-order corrections to string motion are considered, the superscript 1 in $\overset{1}{\chi}_{(m)}$ and similar quantities is omitted in this section.

[6]The integrals were carried out using Gradshteyn and Ryzhik [32], section 2.25. The solutions were verified using Maple V.

One can also obtain solutions for the other components of $\chi_{(m)}$. Substituting (3.51) and (3.50) into (3.54) and performing the integrations one gets, for the initial conditions $\chi_{(m)}(0,\sigma) = 0$,

$$\begin{aligned}
\chi_{(0)}(\tau,\sigma) &= M\cosh(\beta)\,[\ln(F_+(\tau,\sigma)) + \ln(F_-(\tau,\sigma)) && (3.60)\\
&+ \frac{1}{2}\cosh(\beta)\;[sgn(s_+)\ln(G_+(\tau,\sigma)) + sgn(s_-)\ln(G_-(\tau,\sigma))]] \\
\chi_{(1)}(\tau,\sigma) &= M\cosh(\beta)\;[\ln(F_+(\tau,\sigma)) - \ln(F_-(\tau,\sigma))] && (3.61)\\
\chi_{(2)}(\tau,\sigma) &= -M\sinh(\beta)\,[\ln(F_+(\tau,\sigma)) + \ln(F_-(\tau,\sigma)) && (3.62)\\
&+ \frac{1}{2}\cosh(\beta)\;[sgn(s_+)\ln(G_+(\tau,\sigma)) + sgn(s_-)\ln(G_-(\tau,\sigma))]]
\end{aligned}$$

where

$$F_\pm(\tau,\sigma) = \frac{R\cosh\beta + \tau\cosh^2\beta + X_0\sinh\beta - s_\pm}{\cosh\beta\sqrt{\rho^2 + s_\pm^2} + X_0\sinh\beta - s_\pm} \qquad (3.63)$$

$$G_\pm(\tau,\sigma) = \frac{\sqrt{\rho^2 + s_\pm^2} - |\,s_\pm\,|}{\sqrt{\rho^2 + s_\pm^2} + |\,s_\pm\,|} \qquad (3.64)$$

These results are applied to the study of string scattering in the weak field regime (Chapter 4); they are also used as boundary conditions and initial data for numerical work, as discussed in the next section.

3.3.3 Low-Velocity Limit

As was already mentioned, the components $f_{(R)}$ normal to the string world-sheet are components of the physical force acting on the string. As can be seen from (3.51), the force $f_{(R)}$ acting on the string vanishes in the limit $v \to 0$. This fact has a simple physical explanation. As was shown in Ref. [29], a static string configuration in a static spacetime is a geodesic in a spacetime with the metric $|g_{00}|g_{ij}$, which in this case takes the form

$$dS^2 = |g_{00}|g_{ij}dx^i dx^j = (1-2\Phi)(1+2\Psi)(dX^2 + dY^2 + dZ^2)\,. \qquad (3.65)$$

In the leading order, $\Phi = \Psi = \varphi$, and the string is a straight line, as was first observed by Vilenkin [52]. In other words, in the first-order approximation a force acting on a static string in a static spacetime of a black hole vanishes. For this reason, the leading terms in the expansion of the force are of the second order in φ, and they remain so until $v/c \sim (M/b_{imp})^{1/2}$. In this section the effect of these second order terms on the motion of the string is discussed in the limit of very small velocities.

Substituting Eqn. (3.33) into the dynamical equations (3.3),

$$n^\mu_{(R)}\,\Box\overset{2}{X}{}^{(R)} = \overset{2}{f}{}^{\mu} \equiv A^\mu + B^\mu\,, \qquad (3.66)$$

where the $\Box$-operator is given by (3.46) and,

$$A^\mu = -\eta^{AB} \overset{2}{\Gamma}{}^{\mu}_{\alpha\beta} X^\alpha_{,A} X^\beta_{,B}\,, \quad B^\mu = -\eta^{AB} \overset{1}{\Gamma}{}^{\mu}_{\alpha\beta} (\overset{1}{X}{}^{(m)}_{,B} X^\alpha_{,A} e^\beta_{(m)} + \overset{1}{X}{}^{(m)}_{,A} X^\beta_{,B} e^\alpha_{(m)})\,. \quad (3.67)$$

Note that

$$\overset{2}{\Gamma}{}^{\mu}_{\alpha\beta} = \eta^{\mu\nu} \overset{2}{\Gamma}_{\nu,\alpha\beta} + \overset{1}{\gamma}{}^{\mu\nu} \overset{1}{\Gamma}_{\nu,\alpha\beta} \quad (3.68)$$

where $\overset{1}{\Gamma}_{\nu,\alpha\beta}$ is given by (3.44) and,

$$\begin{aligned} \overset{2}{\Gamma}_{\nu,\alpha\beta} &= \frac{1}{2}\left(\overset{2}{\gamma}_{\nu\alpha,\beta} + \overset{2}{\gamma}_{\nu\beta,\alpha} - \overset{2}{\gamma}_{\alpha\beta,\nu}\right) \quad (3.69)\\ &= 2\varphi\,(\varphi_{,\alpha}\,\pi_{\nu\beta} + \varphi_{,\beta}\,\pi_{\nu\alpha} - \varphi_{,\nu}\,\pi_{\alpha\beta}) \end{aligned}$$

where $\overset{2}{\gamma}_{\mu\nu,\eta} = 2\varphi\,\varphi_{,\eta}\,\pi_{\mu\nu}$.

To simplify matters, consider only the corrections to the motion of the string in Y-direction. It is easy to verify that

$$A^2 = \cosh^2\beta\,\overset{2}{\Gamma}{}^{2}_{00} + \sinh^2\beta\,\overset{2}{\Gamma}{}^{2}_{11} - \overset{2}{\Gamma}{}^{2}_{33} = 2\varphi\varphi_{,2}[2(1+b) - (2+a+b)\cosh^2\beta]\,. \quad (3.70)$$

Calculations also give

$$B^2 = 2\varphi_{,2}\left[(\cosh^2\beta + \sinh^2\beta)\,\overset{1}{X}_{(0),\tau} - \sinh(2\beta)\,\overset{1}{X}_{(2),\tau} + \overset{1}{X}_{(1),\sigma}\right] - 2\varphi_{,3}\,\overset{1}{X}_{(3),\sigma}\,. \quad (3.71)$$

At low velocities ($\beta \to 0$) one has

$$A^2 \sim 2\varphi\varphi_{,2}(b-a)\,, \quad B^2 \sim 2\varphi_{,2}(\overset{1}{X}_{(0),\tau} + \overset{1}{X}_{(1),\sigma}) - 2\varphi_{,3}\,\overset{1}{X}_{(3),\sigma}\,. \quad (3.72)$$

Equation (3.57) shows that $\overset{1}{X}_{(3)}$ vanishes at $\beta \to 0$. Using gauge conditions (3.41), it follows that

$$\overset{2}{f}_{(3)} \sim -2(2+a-b)\varphi\varphi_{,2}\,. \quad (3.73)$$

Using a relation similar to Eqn. (4.1),

$$\overset{2}{X}_{(3)}\,(\tau=\infty) = \frac{2+a-b}{2\sinh\beta}\int_{-\infty}^{\infty} dX \int_{-\infty}^{\infty} dZ\,\frac{\partial\varphi^2}{\partial Y}(X, Y_0, Z)\,. \quad (3.74)$$

Calculating the integral one gets

$$\overset{2}{X}_{(3)}\,(\tau=\infty) = -\frac{\pi M^2(2+a-b)}{Y_0\sinh\beta}\,. \quad (3.75)$$

For the scattering of the string on the Schwarzschild black hole, $a=-1$ and $b=3/4$, so that one has

$$\overset{2}{X}_{(3)}\,(\tau=\infty) = -\frac{\pi(GM)^2}{4c^4 Y_0\sinh\beta}\,. \quad (3.76)$$

These results will be applied to the problem of string capture in Chapter 6.

Using the expressions for the coefficients a and b for the scattering on a Reissner-Nordstrom black hole (see footnote 3) one gets

$$\overset{2}{X}_{(3)}\,(\tau=\infty) = -\frac{\pi((GM)^2 - GQ^2)}{4c^4 Y_0 \sinh\beta}\,. \tag{3.77}$$

These results agree with those of Page [44].

3.4 Ultra-relativistic String Motion in a Weak Gravitational Field

The solutions presented here are, in a sense, a special case of the perturbative solutions documented above. The ultra-relativistic solutions are simpler in form, and a number of properties of ultra-relativistic scattering are derived in a straightforward manner in Chapter 4 using these simpler solutions.

The key observation which leads to a solution of the equations of motion in the ultra-relativistic limit is the following: in the reference frame of the string the black hole moves with $v \approx 1$ and its gravitational field is boosted to the shock wave [33]. As a result, before and after crossing the null surface N representing the black hole, the string obeys the free equations in flat spacetime. All the information concerning the non-linear interaction with the gravitational field of the black hole can be obtained in the form of "jump" conditions on the null surface N. Such solutions were studied earlier (see e.g. Ref. [3]).

To obtain the metric of an ultra-relativistic black hole one starts with the metric (3.27) written in the form

$$ds^2 = (1+2\Psi)ds_0^2 + 2(\Phi+\Psi)dT^2\,, \tag{3.78}$$

where

$$ds_0^2 = -dT^2 + dX^2 + dY^2 + dZ^2\,, \tag{3.79}$$

and make the boost transformation

$$\bar{T} = \gamma(T - vX)\,, \quad \bar{X} = \gamma(X - vT)\,, \quad \bar{Y} = Y\,, \quad \bar{Z} = Z\,. \tag{3.80}$$

Let $X_\pm = \bar{T} \pm \bar{X}$ so that

$$X_+ = \gamma(1-v)\,(T+X)\,, \quad X_- = \gamma(1+v)\,(T-X)\,, \tag{3.81}$$

and, since $\gamma^2 = \left(1-v^2\right)^{-1}$,

$$\begin{aligned} T &= \frac{\gamma}{2}(1+v)\left(X_+ + \left(\frac{1-v}{1+v}\right)X_-\right)\,, \\ X &= \frac{\gamma}{2}(1+v)\left(X_+ - \left(\frac{1-v}{1+v}\right)X_-\right)\,. \end{aligned} \tag{3.82}$$

Using Eqns. (3.82) the metric (3.78) takes the form

$$\begin{aligned} ds^2 &= (1+2\Psi)\left[-dX_-\,dX_+ + dY^2 + dZ^2\right] \\ &+ \frac{\gamma^2}{2}(1+v)^2(\Phi+\Psi)\left(dX_+ + \frac{1-v}{1+v}dX_-\right)^2 . \end{aligned} \tag{3.83}$$

In the lowest order $\Phi = \Psi = \varphi = M/R$, where $R = \sqrt{X^2+Y^2+Z^2}$ can be rewritten using Eqn. (3.82) as

$$R = \gamma\sqrt{\left(\frac{1+v}{2}\right)^2\left(X_+ - \left(\frac{1-v}{1+v}\right)X_+\right)^2 + \frac{1}{\gamma^2}\left(Y^2+Z^2\right)} \tag{3.84}$$

so that

$$\varphi = \frac{\gamma M(1-v^2)}{\left[\left(\frac{1+v}{2}\right)^2\left(X_+ - \left(\frac{1-v}{1+v}\right)X_-\right)^2 + (1-v^2)(Y^2+Z^2)\right]^{1/2}} . \tag{3.85}$$

The metric (3.83) takes the form

$$\begin{aligned} ds^2 &= -dX_-\,dX_+ + dY^2 + dZ^2 \\ &+ 2\varphi\left(dY^2+dZ^2\right) + \gamma^2\varphi\left((1+v)^2\,dX_+^2 + (1-v)^2 dX_-^2\right) \end{aligned} \tag{3.86}$$

In the limit $v \to 1$ and γM fixed one has [3]

$$\lim_{v\to 1}\gamma^2\varphi = \lim_{v\to 1}\frac{\gamma M}{\sqrt{X_+^2 + (1-v^2)\rho^2}} = -\gamma M\delta(X_+)\ln\rho^2 , \tag{3.87}$$

where $\rho^2 = Y^2 + Z^2$. From this it follows that the metric in the Aichelburg-Sexl form [1] is obtained

$$ds^2 = -dX_-\,dX_+ + dY^2 + dZ^2 - 4\gamma M F\delta(X_+)dX_+^2 . \tag{3.88}$$

where $F = \ln\rho^2$. The boosted metric in this form represents a gravitational shockwave. The following components of the Christoffel symbols do not vanish:

$$\begin{aligned} &\Gamma^-_{++} = 4\gamma M\,F\,\delta'(X_+), \quad \Gamma^-_{+Y} = 2\Gamma^Y_{++} = 4\gamma M\,F_{,Y}\,\delta(X_+), \\ &\Gamma^-_{+Z} = 2\Gamma^Z_{++} = 4\gamma M\,F_{,Z}\,\delta(X_+). \end{aligned} \tag{3.89}$$

The in-coming straight string motion (3.22) in this limit takes the form

$$X_+|_{\tau<0} = \tau, \quad X_-|_{\tau<0} = \tau - 2\gamma X_0, \quad Y|_{\tau<0} = Y_0, \quad Z|_{\tau<0} = \sigma . \tag{3.90}$$

First solve the string equation (3.3) in the metric (3.88) for the initial conditions (3.90) using the conformal gauge in which $\sqrt{-h}h^{AB} = \eta^{AB}$, so that $\Box = -\partial_\tau^2 + \partial_\sigma^2$.

The equation for X_+ takes a simple form

$$\Box X_+ = 0\,. \tag{3.91}$$

Hence its solution obeying the proper initial conditions is

$$X_+ = \tau\,. \tag{3.92}$$

The equation for Y is

$$\Box Y = 2\gamma M\, F_{,Y}\, \delta(\tau)\,. \tag{3.93}$$

The solution obeying the initial conditions (3.90) is solved using the Green's Function (3.52) and has the form

$$Y|_{\tau>0} = Y_0 - 2\gamma M \left[\arctan\left(\frac{\tau+\sigma}{Y_0}\right) + \arctan\left(\frac{\tau-\sigma}{Y_0}\right)\right]. \tag{3.94}$$

Similarly, solving equation

$$\Box Z = 2\gamma M\, F_{,Z}\, \delta(\tau) \tag{3.95}$$

for Z with the initial conditions (3.90) one gets

$$Z|_{\tau>0} = \sigma - \gamma M \ln\left[\frac{Y_0^2 + (\tau+\sigma)^2}{Y_0^2 + (\tau-\sigma)^2}\right]. \tag{3.96}$$

And finally, a solution of the equation for X_-

$$\Box X_- = 4\gamma M\, F\, \delta'(\tau) \tag{3.97}$$

is

$$X_-|_{\tau>0} = \tau - 2\gamma\, X_0 - \gamma M \left[\ln\left(Y_0^2 + (\tau+\sigma)^2\right) + \ln\left(Y_0^2 + (\tau-\sigma)^2\right)\right]. \tag{3.98}$$

It is easy to verify that the obtained solutions obey constraint equations (3.5) which for the case under consideration take the form

$$\dot{Y}^2 + Y'^2 + \dot{Z}^2 + Z'^2 = \dot{X}_- + 4\gamma M F \delta(\tau)\,, \tag{3.99}$$

$$\dot{Y}Y' + \dot{Z}Z' = \frac{1}{2}X'_-\,, \tag{3.100}$$

Here a dot and prime denote derivatives with respect to τ and σ.

These results are applied to the study of string scattering in the ultra-relativistic regime, as discussed in Chapter 4.

3.5 String Motion in a Weak Gravitational Field (rotating source)

First-order perturbative solutions in Kerr spacetime can be obtained using the general procedure outlined above to solve the scalar perturbation equations $\chi_{(m)}$. However, the perturbative expansion of the Kerr metric is more involved than that of the Schwarzschild metric. In the latter case, the expansion was done directly in isotropic coordinates and first-order contributions to the metric, $\overset{1}{\gamma}$, and Christoffel symbols, $\overset{1}{\Gamma}$, were easily obtained. Since there is no analogous coordinate system for Kerr black holes, the perturbative expansion must be carried out in two stages, beginning in Boyer-Lindquist coordinates to obtain leading terms, and then converting these terms to Cartesian coordinates.

The Kerr metric in Boyer-Lindquist coordinates, (t, r, θ, ϕ), has the form (see Appendix D),

$$\begin{aligned} ds^2 &= -\left(1 - \frac{2\,M\,r}{\Sigma}\right) dt^2 - \frac{4\,a\,M\,r\sin^2\theta}{\Sigma}\, dt\, d\phi + \frac{\Sigma}{\Delta}\, dr^2 \\ &+ \Sigma\, d\theta^2 + \frac{A\sin^2\theta}{\Sigma}\, d\phi^2 \end{aligned} \tag{3.101}$$

where $a = J/M$ is the specific angular momentum, and

$$\begin{aligned} \Delta &:= r^2 - 2\,M\,r + a^2 \\ \Sigma &:= r^2 + a^2\cos^2\theta \\ A &:= \left(r^2 + a^2\right)^2 - a^2\sin^2\theta\,\Delta\,. \end{aligned} \tag{3.102}$$

The metric components are expanded in powers of r, for r large,

$$\begin{aligned} g_{00} &\approx -1 + \frac{2\,M}{r} + \mathcal{O}(r^{-3})\,, \\ g_{03} &\approx -\frac{4\,a\,M\sin^2\theta}{r} + \mathcal{O}(r^{-3})\,, \\ g_{11} &\approx 1 + \frac{2\,M}{r} + \mathcal{O}(r^{-2})\,, \\ g_{22} &\approx r^2\,, \\ g_{33} &\approx r^2\sin^2\theta\,. \end{aligned}$$

In this expansion, the new contribution due to angular momentum is the $\mathcal{O}(r^{-1})$ term in g_{03}; otherwise, the metric is equivalent to the expansion of the Schwarzschild metric.

Now transform the coordinates to Cartesian using Eqn.(E.2) to obtain the metric

$$\begin{aligned} ds^2 &\approx -\left(1 - \frac{2M}{R}\right) dT^2 + \left(1 + \frac{2M}{R}\right)\left(dX^2 + dY^2 + dZ^2\right) \\ &- \frac{4\,a\,M}{R^3}\left(X\,dY - Y\,dX\right) dT\,, \end{aligned} \tag{3.103}$$

where $R = \sqrt{X^2 + Y^2 + Z^2}$ and the black hole is rotating about the Z axis. This result is in agreement with the general weak-field formula (19.5) in Misner, Thorne and Wheeler [40] for a gravitating source rotating about the Z axis. Further, this result reduces to the weak-field metric for Schwarzschild black holes in the limit where $a \to 0$.

The new contribution to the Christoffel symbols is

$$\overset{1}{\Gamma}{}^{2}_{01} \approx \frac{a\,M}{R^3}, \tag{3.104}$$

with $R^2 = (X_0 + \tau \sinh\beta)^2 + Y_0^2 + \sigma^2$.

The source term $f_{(3)}$ appearing in Eqn. (3.45) receives an extra contribution from angular momentum

$$\overset{1}{f}_{(3)} = -2M \sinh\beta Y_0 \left(\sinh\beta \pm \frac{a\cosh\beta}{Y_0}\right) \frac{1}{R^3}. \tag{3.105}$$

The new solution for $\chi_{(3)}$ with black hole angular momentum is

$$\chi_{(3)} = -M \left(\sinh(\beta) \pm \frac{a\cosh(\beta)}{Y_0}\right) \{H_+(\tau,\sigma) + H_-(\tau,\sigma)\}, \tag{3.106}$$

where $H_\pm$ are given by Eqn. (3.58). The choice of sign for the angular momentum term depends on the choice of initial conditions. As discussed in Chapter 2, the angular momentum of the black hole now introduces an additional dimension to the scattering problem. The terms retrograde and prograde (see Fig. 2.4) were introduced to describe the two possible cases for particle scattering. These terms will be used here also. Here, the convention $X_0 < 0$, $b = Y_0 > 0$, and $\beta > 0$ results in choosing the + sign for the angular momentum term (this can be verified by carefully following signs through the detailed perturbative calculations).

According to this lowest-order calculation, angular momentum simply introduces a small correction to the amplitude of the transverse perturbation $\chi_{(3)}$ that is proportional to a and inversely proportional to impact parameter. It is important to note, however, that the perturbation calculation outlined here has to be approached with caution. The magnitude of the correction is small and may be subject to further corrections from higher-order perturbation terms.

It would seem as if the methods used to study the low-velocity behaviour of strings should extend to Kerr spacetime, with appropriate caution taken in obtaining the higher-order expansions of the metric and the Christoffel symbols. Due to time constraints, these calculations will not be pursued in this document, but will be the subject of a subsequent publication.

3.6 Numerical Schemes

The above perturbative solutions are important for the general formulation of the scattering problem (discussed in the next chapter). If a string enters in the strong field region near

the black hole, the weak-field solutions break down and numerical solutions must be found instead. This section describes the main features of the numerical schemes, the results of which will be discussed in subsequent chapters.

In seeking numerical solutions, a method of truncating the string to a reasonably short segment is required since strings of infinite length cannot be dealt with directly. Such a physical truncation imposes special boundary conditions since it is crucial to reproduce the motion of an infinitely long string. Two such boundary conditions have been developed:

- **Numerical Scheme A:** This method places the truncation points a reasonable distance away from the black hole, subject to the condition that the end points move in a weak gravitational field where a perturbative solution to the equations of motion is applicable and can be imposed as boundary conditions.

- **Numerical Scheme B:** This method places a massive particle at each end of a segment of string and requires that the motion of these particles mimic the motion of the portions of the string lying outside the region of interest. Without the "support" of such massive particles, the segment of string would collapse on itself at the speed of light.

Each method has distinct advantages, and both were used extensively in the course of this study. Since method A is a direct application of the standard equations of motion, it is the better model in that it deals directly with an infinite string. However, from the numerical perspective, method B offers certain advantages that will be discussed in subsequent chapters. Furthermore, provided suitable care is taken to correctly specify the numerical problem, the results from the two models are in complete agreement.

3.6.1 Computational Grid

The numerical solution to the equations of motion begins with the imposition on the internal coordinate space of the string worldsheet of a grid of uniformly spaced points, $(\sigma, \tau) \rightarrow (\sigma_i, \tau_j)$. As shown in Fig. 3.1, this grid consists of a fixed number of points in the spatial (σ) direction, indexed by $i = 1, \ldots, N$, and an unspecified number of points in the temporal (τ) direction, indexed by $j = 0, \ldots, M$, where $j = 0$ represents the initial time step (obtained from initial data) and $j = M$ represents some particular time denoting the end of the evolution. Each set $\{(\sigma_i, \tau_j)\}$ with j fixed represents the string configuration at $\tau = \tau_j$. The spatial interval between grid points, $\Delta\sigma$, is constant. The temporal spacing, $\Delta\tau_j$, is constant across the spatial grid, but may vary from one time step to the next, allowing for an adaptive step size to be used.

The equations of motion describe the spacetime coordinates of the string, $\mathcal{X}^\mu(\sigma, \tau)$. On a discrete grid, denote these coordinates $\mathcal{X}^\mu(\sigma, \tau) \rightarrow \mathcal{X}^\mu(\sigma_i, \tau_j) \equiv (\mathbf{x}^\mu)_{i,j}$. Note that the use of roman indices here is specific to the numerical grid; these should not be confused with spacetime indices. The equations of motion, as shown in Eqns. (3.9) and (3.18), are a system of four coupled non-linear wave equations that specify the time-evolution of the cosmic string, beginning from some initial configuration. How these equations are discretized is outlined here, and discussed in detail in Appendix B.

3.6.2 Discretization

After some trials with more traditional approaches involving substitutions to reduce the equations to a first order system, a method based on Von Neumann's discretization [4] for the linear (scalar) wave equation ($\Box u = 0$) was developed. This approach deals with the wave equation directly as a second-order equation, using standard centered finite differencing for the time and space derivatives. The method deals with the time derivative directly, but uses an average of spatial derivatives at three adjacent time steps, with the third time step being the next increment in the time-evolved solution. Von Neumann's discretization gives rise to an implicit scheme that yields a tridiagonal system where the time-evolved solution is expressed for the entire spatial grid; this system is solved algebraically.

The Von Neumann method has been extended to handle a system of equations, and to handle the non-linear terms shown in Eqns. (3.9) and (3.18). The non-linear terms are expanded to first order in the appropriate grid spacing ($\Delta\tau$ or $\Delta\sigma$), using second-order accurate centered differences for the first derivatives, and treating the Christoffel symbols as known functions of the spacetime coordinates. The non-linear spatial term is averaged in the same manner as the second-order spatial term. The discretized expressions for each term in the equations of motion are combined and manipulated to yield a block-tridiagonal system of linearized equations that is solved iteratively using a Newton-Raphson scheme.

3.6.3 Initial Data and Boundary Conditions

In order to have a well-posed problem, we must specify the shape of the string at some initial time τ_0, along with normal derivatives ($\partial_\tau \mathcal{X}^\mu$) everywhere on the string, including the boundaries, at this initial time. Along with the appropriate boundary conditions, these completely specify the initial/boundary value problem (IBVP). Since the Von Neumann method requires two time steps in order to compute the unknown time step, a completely equivalent way of specifying the IBVP is to use two initial time steps, along with the required boundary conditions.

The design of the numerical solver allows a good deal of flexibility as to the choice of initial-boundary value problem. The two physical boundary conditions discussed above can be implemented using this numerical scheme simply by altering the initialization routine and the conditions imposed on the $i = 1$ and $i = N$ grid locations (i.e. the first and last rows of the block-tridiagonal system).

Numerical Scheme A

In this version, the numerical scheme uses the perturbation solutions of sections 3.3 and 3.5 as initial data, and to prescribe the motion of the end points. Typically, this scheme imposes two conditions to yield usable results:

1. the string must be long enough ($L \sim 200\, r_g$) so that the ends of the truncated string move always in the weak field

2. the string must be started in the weak field, ($r_0 \sim 100\, r_g$) so that the perturbed configuration is a reasonable approximation of the correct string configuration.

Typical runs using this version of the numerical scheme require small grids ($\sim 10^3$ grid points) and short integration times ($\sim 10^2$ to 10^4 time steps). This IBVP is used to probe the low-speed behaviour of strings for both rotating and non-rotating black holes.

Numerical Scheme B

In this version, the numerical scheme uses a finite straight string solution as initial data. It can be shown by direct computation that, in Minkowski spacetime,

$$X^\mu(\tau,\sigma) = \left(\frac{L}{\pi}\cosh(\beta)\,\tau, \frac{L}{\pi}\sinh(\beta)\,\tau + X_0, Y_0, \frac{L}{\pi}\sigma\right) \quad ,\left(-\frac{\pi}{2} \le \sigma \le \frac{\pi}{2}\right), \quad (3.107)$$

is a solution to the equations of motion for a string of length L with massive ends (3.18) that also satisfies the constraints (3.20). The numerical scheme enforces the geodesic boundary conditions (3.19). This scheme must meet two conditions to yield usable results:

1. the string must be very long ($L \sim 2000\, r_g$) to ensure that the motion of the end points is not extensively disturbed by the black hole,

2. the string must be started well away from the black hole ($r_0 \sim 1000\, r_g$) so that the straight string configuration is a reasonable approximation of the correct string configuration.

Typical runs using this version of the numerical scheme require large grids ($\sim 10^4$ grid points) and long integration times ($\sim 10^4$ to 10^5 time steps). This IBVP is used to study the long-term evolution of strings (scattering) and the high-speed capture cross-section. Since the massive particles at the ends of the string act as perfect mirrors, an additional constraint is imposed on string length for long integrations: perturbations propagating along the string at the speed of light cannot be allowed to reach the end points in the course of calculations.

Where the data for these two schemes overlaps, it is possible to validate the numerical results. They were also tested against the perturbation solutions and using other means, as documented in Appendix C.

3.6.4 Role of Constraints

The constraint equations, (3.10) or (3.20), are used as checks on the solutions to the equations of motion. The calculation of the discretized form of these equations (see Appendix B) is carried out periodically during the numerical solution. Statistics are computed for the constraints (average value over the length of the string and standard deviation) at the current time step and reported to an output file. Monitoring that the constraints are consistent with zero to several significant digits is done by inspecting this file. If the constraints are not satisfactorily maintained, that is if the average value grows unacceptably large or undergoes sudden changes, the numerical solution is restarted with new parameters (e.g.

finer grid, finer step size). The specific tolerances for constraint calculations are discussed in subsequent chapters; typically, the constraints were expected to be consistent with zero to four significant figures for numerical scheme A and six significant figures for numerical scheme B. Tighter tolerances can be achieved by increasing the number of grid points (and significantly increasing solution time), but for the purposes of this study, the above values were deemed a reasonable compromise between accuracy and speed.

3.7 Chapter Summary

In this section, the following results were established:

- for a cosmic string moving in a weak gravitational field, perturbative solutions were developed for non-rotating sources;
- a special form of the perturbative solution was obtained in the limit where the string moves at ultra-relativistic velocity;
- the perturbative solution was extended to rotating sources;
- a discretization of the equations of motion, based on a non-linear extension of Von Neumann's discretization of the wave equation was also discussed; this method can be used to numerically evolve cosmic strings using initial-boundary value data derived from both the perturbative solution and the solution for a straight string terminated by infinitely massive particles.

The following chapters discuss how these analytic and numerical solutions were used to study the dynamics of cosmic strings near black holes.

Chapter 4

Gravitational Scattering of Cosmic Strings by a Black Hole

This chapter deals with the gravitational scattering of a straight cosmic string by a black hole. The problem under consideration is that of an initially straight string starting at a large distance from the black hole and approaching with a velocity $v\,(0 < v < c)$ and impact parameter b, as shown in Fig. 1.1. The impact parameter is greater than the critical impact parameter for capture, so the string scatters to infinity. It will be shown that the perturbative solutions can be applied to formulate the scattering problem, and from these solutions a number of scattering parameters can be derived which are useful in discussing the general scattering problem.

A cosmic string is an extended object whose response to a gravitational field is determined by its internal tension. Cosmic strings formed at the GUT-scale are extremely stiff objects, and straight strings have an infinite number of internal degrees of freedom. The scattering of a string is an inelastic process since the string absorbs some energy (i.e. the string's internal energy, connected with the excitations of its degrees of freedom, changes during the interaction). Naively, one can expect that only a close encounter with a black hole's extreme gravitational field can excite string modes to any great extent. The fact that such internal modes can be excited leads to many dynamical consequences that will be discussed in this and subsequent chapters.

This chapter is divided into five sections. The first three sections discuss the scattering of straight cosmic strings by Schwarzschild black holes, which has proven to be far more interesting than initially anticipated. Scattering is discussed in the weak-field, strong-field, and ultra-relativistic regimes, comparing analytic and numerical results in each case. The fourth section compares the results of string scattering to that for a dust (tensionless) string in order to gain insight on the role of the internal tension. The fifth section shows how black hole angular momentum affects scattering.

4.1 Weak-field String Scattering by a Non-rotating Black Hole

A simple picture of scattering in the weak field arises when one considers the perturbation solutions of Section 3.3. In order to set the context, consider the asymptotic solution, at $\tau \to \infty$, of the $\chi_{(3)}$ perturbation (3.53), assuming that $\chi_{(3)} = 0$ at $\tau \to -\infty$,

$$\chi_{(3)}(\tau = \infty) = \lim_{\tau \to \infty} \chi_{(3)}(\tau, \sigma) = -\frac{1}{2} \int_{-\infty}^{\infty} d\tau' \int_{-\infty}^{\infty} d\sigma' \, f_{(3)}(\tau', \sigma') \,. \tag{4.1}$$

Substituting expression (3.51) for $f_{(3)}$ and making a change of variables of integration from (τ, σ) to (X, Z) (using Eqn. (3.22)) the integral takes the form

$$\chi_{(3)}(\tau = \infty) = -\sinh\beta \int_{-\infty}^{\infty} dX \int_{-\infty}^{\infty} dZ \, \frac{\partial \varphi}{\partial Y}(X, Y_0, Z) \,. \tag{4.2}$$

This integral represents the flux of the Newton gravitational field through the plane $Y = Y_0$ and is equal to $2\pi M$ (that is a half of the total flux $4\pi M$). Using this simple observation, it follows that, as a result of scattering, the string as the whole is displaced downward in the Y-direction by a constant value

$$\chi_{(3)}(\tau = \infty) = -2\pi M \sinh\beta \,. \tag{4.3}$$

At late but finite time only part of the string is displaced. The full perturbative solutions help shed light on the process.

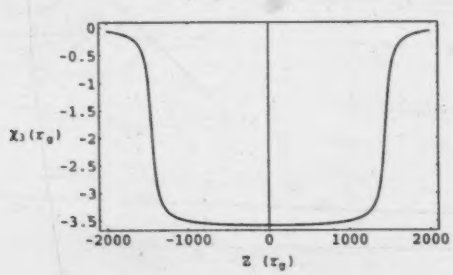

Figure 4.1: $\chi_{(3)}$ perturbation.

The perturbation solutions are illustrated by Figs. 4.1–4.3, where the solutions are applied to the case of a straight string with initial velocity $v = \tanh\beta = 0.76c$ and impact parameter $b = Y_0 = 40\, r_g$ (for $-2000\, r_g < \sigma < 2000\, r_g$)[1]. These figures show each perturbation at late proper time, when the string is well past the black hole. The $\chi_{(3)} \equiv \delta Y$ perturbation (Fig. 4.1) describes the deformation of the string normal to the background world-sheet; the two kink-like pulses propagating away from the $Z = 0$ plane at the speed of

[1]For non-rotating black holes, distances are measured in units of the gravitational radius, $r_g = 2M$.

light are clearly visible, and their amplitude is considerably larger that any of the other perturbations. These pulses carry energy away to infinity and, in the process, shift the string's late-time position roughly $3.5\,r_g$ below the original position. The $\chi_{(1)} \equiv \delta Z$ perturbation (Fig. 4.2) represents lateral displacements of points on the string towards the $Z = 0$ plane; the amplitude of these displacements is small at low velocities, but becomes significant in the limit of ultra-relativistic velocity and shallow impact parameter, where lateral displacements of the string are involved in transient loop formation. The $\chi_{(0)}$ and $\chi_{(2)}$ perturbations (Fig. 4.3) also show two pulses propagating outward, but these are exceedingly small, and are of secondary interest in the scattering problem.

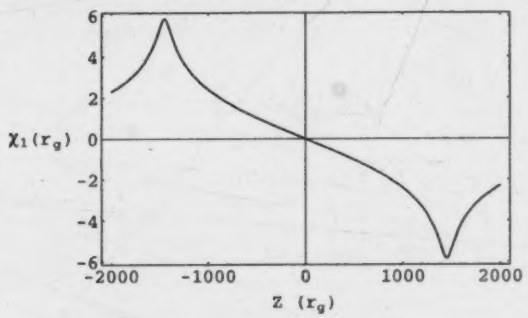

Figure 4.2: $\chi_{(1)}$ perturbation.

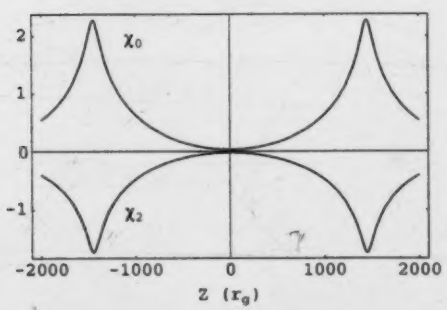

Figure 4.3: $\chi_{(0)}$ and $\chi_{(2)}$ perturbations.

The perturbation solutions can be used to reconstruct the full world-sheet of the string in Cartesian coordinates, using

$$\mathcal{X}^\mu(\tau,\sigma) = X^\mu(\tau,\sigma) + \chi^{(m)}(\tau,\sigma)e^\mu_{(m)}\,, \tag{4.4}$$

where the tetrad components are given in Eqns. (3.23) and (3.24). Such a reconstruction is shown in Fig. 4.4, where a sequence of string configurations separated by constant intervals of proper time in two separate views. The view on the left looks down on the XZ plane

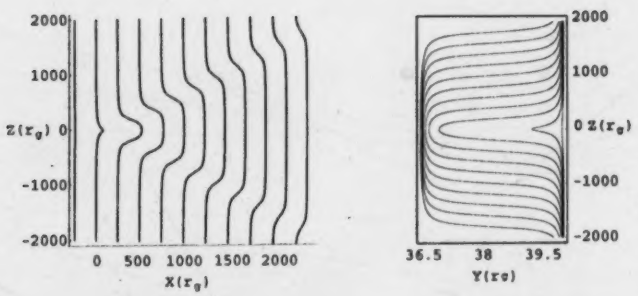

Figure 4.4: Reconstruction of perturbed string (Cartesian coordinates).

and shows the outward propagation of the two pulses (the black hole lies at the origin). Note that the view is a 3D projection; the kinks appear to extend in the X-direction, but they actually lie completely in the Y-direction (the effect is an artifact of the viewpoint chosen for this view). The view on the right looks toward the origin along the direction of motion, and shows the growth of the perturbations along the Y axis. Comparing Figs. 4.1 through 4.3, it is easily seen that the shape of the perturbed world-sheet is almost completely determined by the $\chi_{(3)}$ (or δY) perturbation. The contribution from the other perturbations is undetectable on the scale used in Fig. 4.4.

The scattering of the string can be used to generate a schematic representation of string worldsheet, as shown in Fig. 4.5. This figure is a quite general representation of the scattering problem and will be useful in describing the general (late-time) features of string scattering in all regimes. The straight string starts its motion in the plane $Y = Y_0$; denote this the *in-plane*. This plane represents the motion of the free string in flat spacetime. At late times, the scattered string approaches another plane, offset from the in-plane by A_∞; denote this the *out-plane*. As the energy acquired by the string is propagated to infinity through the two kinks, more and more of the string falls to the out-string plane. The asymptotic deflection, A_∞, is determined by the properties of the encounter.

4.1.1 Late-time Properties

In terms of the background solution (3.22), the string reaches periastron when $\tau \sinh\beta = -X_0$. In order to study the late time behaviour of the string it is advantageous to rewrite the perturbation solution in a more symmetric form by making the substitutions $X_0 = -L$ and $\tau \sinh\beta = 2L$, and considering the limit $L \to \infty$. In this limit, the expression for $H_\pm$ (Eqn. (3.58)) simplifies to

$$\begin{aligned} H_\pm &\approx \arctan\left[\frac{L \pm \sigma \sinh\beta}{Y_0 \sinh\beta\sqrt{1+(\sigma/L)^2}}\right] \\ &+ \arctan\left[\frac{L \pm \sigma \sinh\beta}{Y_0 \sinh\beta\sqrt{1+((2/\sinh\beta) \pm \sigma/L)^2}}\right], \end{aligned} \tag{4.5}$$

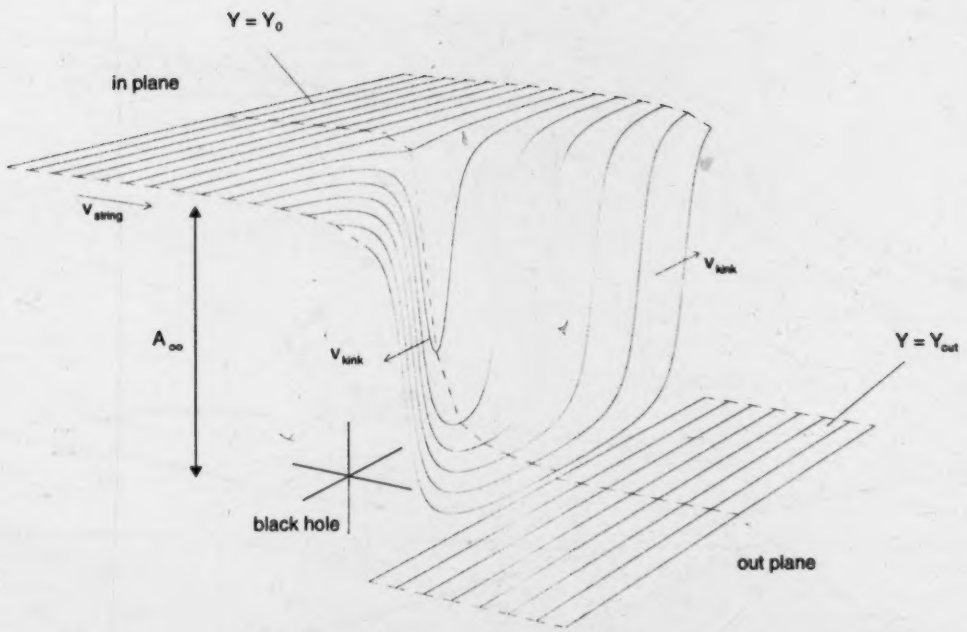

Figure 4.5: A straight cosmic string scattered by a Schwarzschild black hole. Weak-field case.

and the kink is located near $\sigma = \mp L/\sinh\beta$. Using this fact the asymptotic expression for $H_\pm$ further simplifies to

$$H_\pm \approx 2\arctan\left[\frac{L \pm \sigma\sinh\beta}{Y_0\cosh\beta}\right] \to \pi\,. \tag{4.6}$$

From this result, the shift in position of the string is given by

$$A_\infty := Y_{out} - Y_0 = \lim_{L\to\infty} M\,\sinh\beta\,(H_+ + H_-) = -2\pi\,\gamma\,M\,v, \tag{4.7}$$

where $\sinh\beta = \gamma\,v$, $\gamma = \cosh\beta = (1-v^2)^{-1/2}$. Furthermore, each kink has a characteristic width in the external spacetime. This width is computed using $\partial_\sigma\,\chi_{(3)}$ at the center of the kink and using a linear fit to the kink profile. The width of the kink is the distance between the points where this straight line intersect the lines Y_0 and $Y_0 + A_\infty$. It is easy to show that the width of the kinks is given by

$$w = \pi\,Y_0\,\coth\beta = \pi\,\frac{Y_0}{v}. \tag{4.8}$$

Steep pulses occur for small impact parameters ($b = Y_0$) and/or large velocities ($v \to 1$).

As was done for $\chi_{(3)}$, expressions (3.60) - (3.63) for the other components $\chi_{(m)}$ can be rewritten in terms of the parameter L (with $L \gg Y_0$). The functions (3.63) that appear in these expressions take the form

$$F_\pm = \frac{\cosh\beta\sqrt{1+(\sigma/L)^2} + \left(\cosh^2\beta + 1\right)/\sinh\beta - (2/\sinh\beta \pm \sigma/L)}{\cosh\beta\,\sqrt{1+(2/\sinh\beta \pm \sigma/L)^2} - \sinh\beta - (2/\sinh\beta \pm \sigma/L)}, \tag{4.9}$$

$$G_\pm = \frac{\sqrt{1+(2/\sinh\beta \pm \sigma/L)^2} - |\,2/\sinh\beta \pm \sigma/L\,|}{\sqrt{1+(2/\sinh\beta \pm \sigma/L)^2} + |\,2/\sinh\beta \pm \sigma/L\,|}. \tag{4.10}$$

In rewriting the expressions in terms of the location of the kink, $\sigma = \mp L/\sinh\beta$, one sees that, $F_\pm \to \infty$ and $G_\pm \to (\cosh\beta - 1)/(\cosh\beta + 1)$ for $L \to \infty$. Whereas the contributions $\ln G_\pm$ are well behaved, those from $\ln F_\pm$ generate a logarithmic divergence in $\chi_{(0)}$ and $\chi_{(2)}$. This divergence is the result of the long-range nature of gravitational forces and is similar to the logarithmic divergence of the phase for the Coulomb scattering in quantum mechanics. It vanishes for potentials vanishing rapidly enough at infinity.

4.1.2 Energy of Kinks

At late time in the asymptotic region where $g_{\mu\nu} \approx \eta_{\mu\nu}$ the action (3.1) can be written as the sum of the action for the straight string and a term which is quadratic in perturbations. This term is of the form (for details see Ref. [26])

$$S_2 = -\frac{\mu}{2}\int d\tau d\sigma\sqrt{-h}h^{AB}\chi^{(R)}_{,A}\chi^{(R)}_{,B}\,. \tag{4.11}$$

Hence the contributions of $\chi_{(3)}$ to the energy is

$$E = \frac{\mu}{2}\int_{-\infty}^{\infty} d\sigma\,\left\{\left(\frac{\partial\chi_{(3)}}{\partial\tau}\right)^2 + \left(\frac{\partial\chi_{(3)}}{\partial\sigma}\right)^2\right\}. \tag{4.12}$$

Using solution (4.6) and

$$\frac{\partial \chi_{(3)}}{\partial \tau} = \frac{\partial \chi_{(3)}}{\partial L}\frac{\partial L}{\partial \tau} = \frac{\sinh\beta}{2}\frac{\partial \chi_{(3)}}{\partial L}, \tag{4.13}$$

the integrals can be evaluated in a straightforward manner. In the limit $L \rightarrow \infty$, the energy carried away by each of the kinks has a very simple form

$$E = \frac{5\mu}{32}\frac{A_\infty^2}{w}. \tag{4.14}$$

Large, steep pulses created at small impact parameters and ultra-relativistic velocities carry away the most energy.

4.1.3 Comparison to Numerical Results

The perturbative solution to the equations of motion of an infinitely long cosmic string is most conveniently carried out in isotropic coordinates, (T, X, Y, Z). Numerically, however, the scattering problem is best studied in Eddington-Finkelstein In-going coordinates since the Christoffel symbols in this coordinate system are simple, few in number, and regular everywhere, and allow following the scattered string very close to the event horizon. The Christoffel symbols associated with this coordinate system, along with their derivatives with respect to the spacetime coordinates (see Appendix D), were derived and inserted as analytic expressions in the portions of the code dealing with the initialization of the tridiagonal matrices. For similar reasons, the scattering of a cosmic string by a rotating black hole is best carried out in Kerr coordinates. In order to compare analytic and numerical results, Cartesian sections of the worldsheet such as those shown above will be used; the coordinate transformations given in Appendix E are used to generate these views from the numerical data.

Both numerical schemes were used for this study. For string scattering where the late-time behaviour of the string is of interest, numerical scheme B is perfectly suitable since a long string is required. Numerical scheme A is useful for obtaining high-resolution views of string scattering in the vicinity of the event horizon.

The solvers are used to generate numerical worldsheets. As the numerical simulation evolves, the solution to the equations of motion is output to a file (the frequency of output, number of grid points, etc. are set by run-time parameters, as discussed in Appendix C). The results of the constraint calculations are also output periodically and are used to validate the numerical solution (numerical constraint calculations are described in Appendix B). If the constraints are not maintained to suitable numerical thresholds, the run is repeated with finer step sizes and/or finer spatial grids, as the situation dictates. For scheme B, the grid-averaged constraint can be expected to be maintained at zero to seven significant digits. For scheme A, dealing with first-order perturbative boundary conditions, the grid-averaged constraint holds to three (perhaps four) significant digits over the duration of the run. In both cases, these zero results should hold at all times; any great departure (whether sudden or over the length of the run) is deemed to invalidate the run.

Figure 4.6 shows sections of the numerical worldsheet of a string under the same conditions as those of Fig. 4.4. As shown in Table 4.1, the maximum amplitude and width of the pulses is in good agreement with the weak-field results obtained from Eqns. (4.7) and (4.8).

Table 4.1: Scattering Parameters - Schwarzschild Weak-field.

	numerical	perturbation
A_∞	$3.4\,r_g$	$3.6\,r_g$
w	$140 r_g$	$165 r_g$
$(v = 0.76\,c,$	$b = 40\,r_g)$	

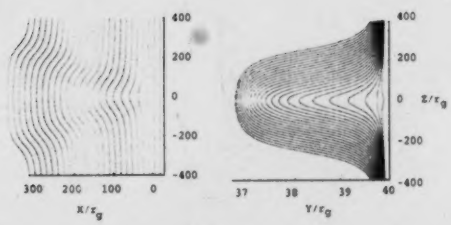

Figure 4.6: Time sequence of string scattering in weak-field regime (numerical results). Black hole lies at origin of coordinate system. Initial velocity, 0.76c, impact parameter 40 r_g.

It will be shown in the following sections that the scattering model just described provides a useful context in which to discuss more general results, even though the weak field approximation breaks down when the impact parameter becomes comparable to the critical impact parameter for capture. The breakdown of the weak field approximation manifests itself as the failure of the analytical expressions to correctly reproduce transient shapes, which develop when the string reaches periastron. However, the late time features of the string, counter-propagating kinks and asymptotic deflection, explained by the weak-field approximation remain qualitatively the same.

4.2 Strong-field Scattering by a Non-rotating Black Hole

When the impact parameter approaches the critical value for capture, the string is in a regime where only numerical solutions are available. This section discusses scattering in this strong-field region, and the numerical solutions are compared to those of the weak-field approximation at intermediate velocities ($0.1c < v < c$) for a range of impact parameters.

The basis for comparison will be the amplitude of the deflection, A_∞, and the characteristic width of each pulse, w_{pulse}, as defined in the previous section.

Figure 4.7 shows sections of the worldsheet of a slow string ($v = 0.2c$) with near-critical impact parameter ($b = 2.5\ r_g$ compared to $b_{\text{capture}} = 2.1\ r_g$). As shown in Table 4.2, the maximum amplitude of the pulses is considerably greater than predicted by weak-field Eqn. (4.7), while there is good agreement in terms of the measured width of the kink and Eqn. (4.8).

Table 4.2: Scattering Parameters - Schwarzschild Strong-field.

	numerical	perturbation
A_∞	$1.8\,r_g$	$0.95\,r_g$
w	$28\,r_g$	$27\,r_g$
$(v = 0.29\,c, \quad b = 2.5\,r_g)$		

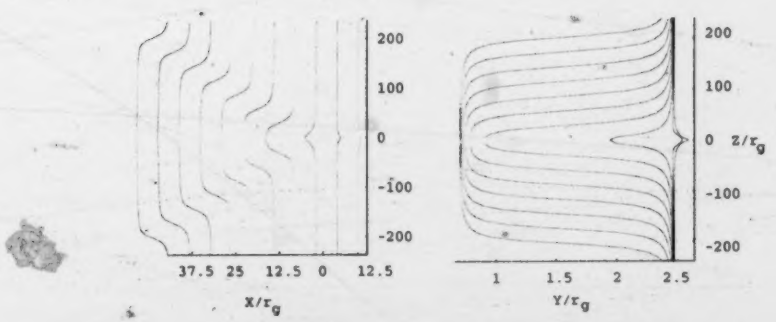

Figure 4.7: Time sequence of string scattering in strong-field regime (numerical results). Black hole lies at origin of coordinate system. Initial velocity, 0.29c, impact parameter 2.5 r_g.

It is important to note that, although the behaviour of the string is qualitatively consistent with the weak-field solutions, the total deflection of the string is greater than predicted by Eqn. (4.7). The discrepancy is made clear by plotting the total deflection of the string obtained from the numerical solver and comparing it to the prediction of Eqn. (4.7). This is done in Fig. 4.8, where the ratio $A_{numerical}/A_{weak}$ is plotted for four velocities. It can be seen that numerical and perturbative results converge for large impact parameters, and that the transition from weak-field to strong-field occurs for impact parameters on the order of $10\,r_g$. Conversely, the curves make it clear that the weak-field solutions are quite acceptable down to very small impact parameters. The curve which suffers a downturn is the lower velocity one, meaning that Eqn. (4.7) predicts a greater shift than the numerical data. The velocity of the string in this case is at the upper threshold where second-order corrections to

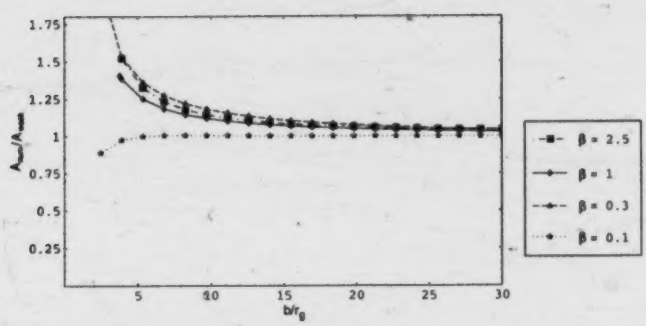

Figure 4.8: Breakdown of weak-field approximation.

the perturbative expansion become important. Recall that the expression (4.7) was derived using results from first-order perturbative calculations.

4.3 Ultra-relativistic Scattering and Loop Formation

Numerical studies of the evolution of stochastic networks of cosmic strings from initial formation to the matter era ([52],[51]) suggest that astrophysical cosmic strings are expected to move with an average velocity $v \approx 0.7c$. For this reason, the results discussed in this section concerning motion at the ultra-relativistic limit are mainly of theoretical interest. Nevertheless, they provide a number of analytic expressions against which to validate numerical solutions in this regime.

Figure 4.9 shows sections of the numerical worldsheet of a string propagating with an initial velocity of $0.995\,c$ ($\gamma = 10$) and impact parameter of $4\,r_g$. The projections onto the XZ plane show a complicated early phase associated with the evolution of short-lived loops and, at late times, two kink-like pulses propagating outward. The speed of the pulses is again that of light. The projections onto the YZ plane show more clearly the early evolution of the loops, which indicate that the points on the string near the $Z = 0$ plane undergo a short-lived deflection across the $Z = 0$ plane. The formation of loops suggests that the behaviour of the string at periastron is particle-like in that there is insufficient time for tension to play a role. However, once clear of the black hole, the tension can again assert itself and solitonic pulses with an S-shaped profile propagate outward. This will be discussed at greater length in the next section. Figure 4.9 also shows that the string self-intersects in the $Z = 0$ plane. As the loop grows, the intersection point moves gradually downward in the Y-direction. Once the loop has reached its maximum size, the S-shaped kinks have formed and begin to propagate outward, away from the $Z = 0$ plane. The intersection point disappears when the kinks have completely separated.

The amplitude of the kinks and the maximum size of the loops can be computed from the ultra-relativistic solutions (3.94) and (3.96). The maximum amplitude comes from the

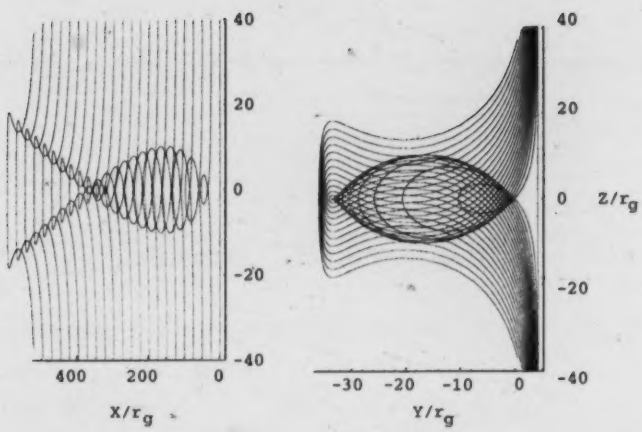

Figure 4.9: Time sequence of string scattering in ultra-relativistic regime (numerical results). Black hole lies at origin of coordinate system. Initial velocity, 0.995c, impact parameter 4.0 r_g.

asymptotic value of $Y|_{\tilde{\tau}>0}$,

$$A_\infty := \lim_{\tau\to\infty} Y|_{\tilde{\tau}>0} - Y_0 = -2\pi\gamma M\,. \tag{4.15}$$

The maximum width of the loops, w_{loop}, occurs when the solution for $Z|_{\tilde{\tau}>0}$ reaches an extremum in both τ and σ. It is straightforward to compute the derivatives from Eqn. (3.96) and show that

$$w_{loop} = 2\gamma\left\{\eta - \frac{1}{2}\ln\left[\frac{1+\eta}{1-\eta}\right]\right\}(r_g) \quad ; \quad \eta = \sqrt{1-\left(\frac{Y_0}{2M\gamma}\right)^2}\,. \tag{4.16}$$

Figure 4.10 shows YZ sections generated from the analytic weak-field and ultra-relativistic solutions for the same physical parameters and intervals of proper time as in Fig. 4.9. It is easy to see that the two analytic solutions are virtually indistinguishable, the only difference being in the first slice, taken at the time where the string reaches periastron. The ultra-relativistic solution shows a completely straight string, as expected, since the black hole does not begin to distort the string until it has passed over it. The weak-field solution shows a slightly bent string, indicating that even at 0.995c, the influence of the black hole is felt before closest approach. For later times, the two solutions are indistinguishable.

As shown in Table 4.3, the maximum amplitude of the deflection and the size of the loops in the numerical data is slightly larger than predicted by Eqns. (4.15) and (4.16). It is important to note that $\gamma = 10$ for these figures, which is low for the ultra-relativistic approximation, but represents a practical upper bound for numerical computations[2]. Furthermore, the impact parameter is very small, and, as shown in the previous section, the approximate solutions are no longer completely accurate under these circumstances.

[2]This is due to numerical anomalies that develop when larger γ-factors are considered. These numerical

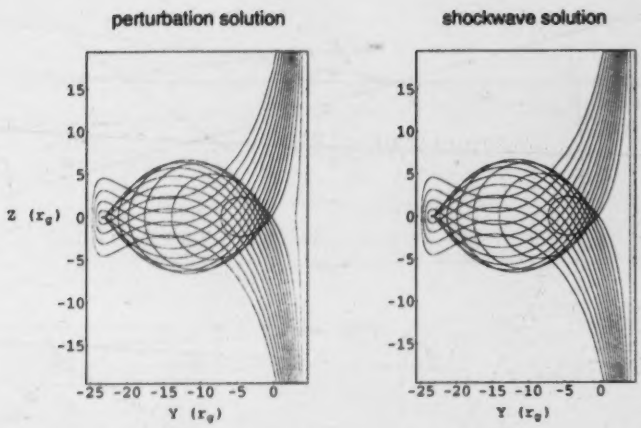

Figure 4.10: Time sequence of string scattering in ultra-relativistic regime (analytic). Black hole lies at origin of coordinate system. Initial velocity, 0.995c, impact parameter 4.0 r_g.

Table 4.3: Scattering Parameters - Schwarzschild Ultra-relativistic.

	numerical	perturbation
A_∞	$40\,r_g$	$31.6\,r_g$
w_{loop}	$20\,r_g$	$13.2\,r_g$
$(v = 0.995\,c,$	$b = 4.0\,r_g)$	

4.3.1 Condition for Loop Formation

The above results show that there is a qualitative difference in string profiles at different velocities. Low velocity scattering sees the evolution of two kinks in the string, but no transient loops, whereas ultra-relativistic scattering shows both kinks and loops.

A loop-like configuration appears when $Z(\tau,\sigma)$ is no longer a monotonic function of σ for a fixed value of τ. This occurs when $Z_{,\sigma} < 0$. From Eqn. (3.96), one gets

$$Z_{,\sigma} = 1 - 2\gamma M\left[\frac{\zeta_+}{Y_0^2+\zeta_+^2} + \frac{\zeta_-}{Y_0^2+\zeta_-^2}\right], \tag{4.17}$$

where $\zeta_\pm = \tau \pm \sigma$. The function $Z_{,\sigma}$ has extrema at $|\zeta_\pm| = |Y_0|$. The minimum of $Z_{,\sigma}$ occurs

anomalies manifest themselves as a rigid deflection of the entire string as it crosses the $X = 0$ plane. The cause of these anomalies was traced to a loss of resolution in the first-order angular derivatives $\partial_\sigma X^\mu$ at large γ-factors. The problem is suppressed by increasing the number of grid points; the large grid sizes required result in a numerically intensive solver.

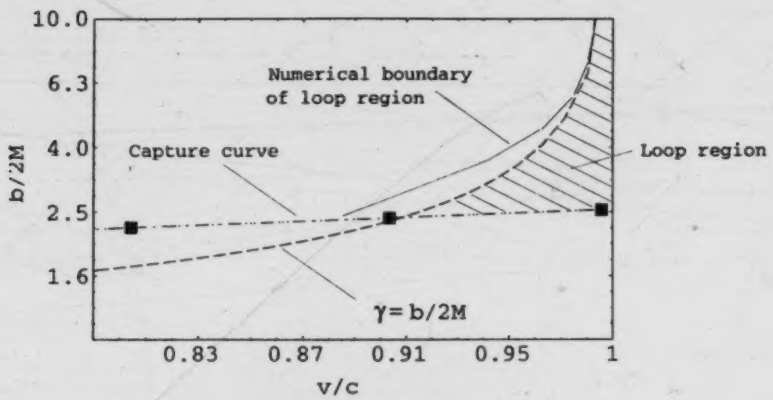

Figure 4.11: Loop formation region.

at $\zeta_+ = \zeta_- = Y_0$, that is at $\tau = Y_0$ and $\sigma = 0$. This minimal value $Z_{,\sigma} = 1 - 2\gamma M/Y_0$ becomes negative when

$$2\gamma M > Y_0 . \tag{4.18}$$

This is the condition for loop formation. This condition can be overlaid on the capture curve (the plot of critical impact parameter for capture introduced in Chapter 2 and discussed in greater detail in Chapter 6), as shown in Fig. 4.11. The loop formation region lies above the capture curve and to the right of the curve $\gamma = Y_0/r_g$; it can be seen that loop formation is a relativistic phenomenon, and the ultra-relativistic solution predicts that this effect cuts off for velocities below $v \sim 0.9c$.

Since the weak-field and ultra-relativistic approximations are accurate only for impact parameters greater than $\sim 10r_g$, the boundary of the loop formation is expected to shift due to strong field effects. The solid line, based on numerical tests to detect loop formation, indicates that the boundary is shifted towards lower velocities; the strong field near the black hole tends to enhance loop formation.

4.3.2 String Self-intersection

Figures 4.6 and 4.9 suggest that the formation of loops is accompanied by string self-intersection. Self-intersection occurs if there exists a pair of points on the string world-sheet, (τ_1, σ_1) and (τ_2, σ_2), such that

$$\mathcal{X}^\mu(\tau_1, \sigma_1) = \mathcal{X}^\mu(\tau_2, \sigma_2) . \tag{4.19}$$

Since this condition forms a system of 4 equations for 4 variables, in the general case the self-intersection points are isolated. For the highly symmetric initial-value problem used here, a point of self-intersection is located at $Z = 0$. Let

$$F(\zeta) = \zeta - 2\gamma M \ln(Y_0^2 + \zeta^2) , \tag{4.20}$$

then $Z = 0$ when $F(\zeta_+) = F(\zeta_-)$. This condition is satisfied for two different points $(\zeta_{+,1}, \zeta_{-,1})$ and $(\zeta_{+,2}, \zeta_{-,2})$ if and only if there exist two different values of c (say, c_1 and $c_2 > c_1$) such that $F(c_1) = F(c_2)$. It happens when the function F is non-monotonic, and the equation

$$F'(\zeta) = 1 - 2\gamma M\zeta/(Y_0^2 + \zeta^2) = 0 \tag{4.21}$$

has a solution. The latter condition implies $2\gamma M \geq Y_0$. This is exactly the same condition of loop formation which was obtained earlier, Eqn. (4.18). The equation $F(c_1) = F(c_2)$ has solutions for

$$c_1 \in (2\gamma M - \sqrt{4(\gamma M)^2 - Y_0^2}, 2\gamma M + \sqrt{4(\gamma M)^2 - Y_0^2}). \tag{4.22}$$

It is easy to verify that for such c_1 all the conditions of self-intersection are met if $\zeta_{-,1} = c_1$, $\zeta_{+,1} = c_2$, $\zeta_{-,2} = c_2$, and $\zeta_{+,2} = c_1$. Simple analysis shows that the self-intersection is stable with respect to small perturbations of the initial state of the string before its scattering by the black hole.

The key point is that, although a high degree of symmetry is imposed on the scattering problem by the initial data, the resulting self-intersection point seems to be a characteristic feature of string scattering at relativistic velocities. The black hole drives the self-intersection process as its gravitational influence draws points on either side of the string towards the $Z = 0$ plane. The string model used here does not allow for the string to break at the self-intersection point (such a model would require higher-order terms in the effective action than the "tree-level" contribution from the Nambu-Goto action). Where such models have been discussed [52] and [2], it is thought that a loop formed through self-intersection would likely break off and the remaining segments of string would reconnect. The size of such loops is thought to be small. If this is indeed the case, then the black hole driven self-intersection could leave a line of small loops in the wake of the string, yielding a physical picture far different from the one shown here. How each of these loops would then interact with the black hole would also prove an interesting problem.

4.4 Role of Tension - Dust String Model

Since a cosmic string is an extended object under tension, motion of a string near a black hole represents the resultant of the competing influences of tension and gravity. In order to shed light on the role of tension in the dynamics of the string, string motion is compared to the motion of an array of test particles initially configured with the same position and initial velocity as the cosmic string.

To study the role of tension for $v < c$, consider a family of N test particles arrayed on a line with initial position $\mathcal{X}^\mu{}_i(\tau_0)$ and initial velocity $\partial_\tau \mathcal{X}^\mu{}_i(\tau_0)$, where i is a position index (an integer between 1 and N) that describes the initial location of the test particle on the line. These particles each satisfy the geodesic equation and constraint,

$$\frac{d^2\mathcal{X}^\nu{}_i}{d\tau^2} + \Gamma^\nu_{\rho\sigma}\frac{d\mathcal{X}^\rho{}_i}{d\tau}\frac{d\mathcal{X}^\sigma{}_i}{d\tau} = 0, \tag{4.23}$$

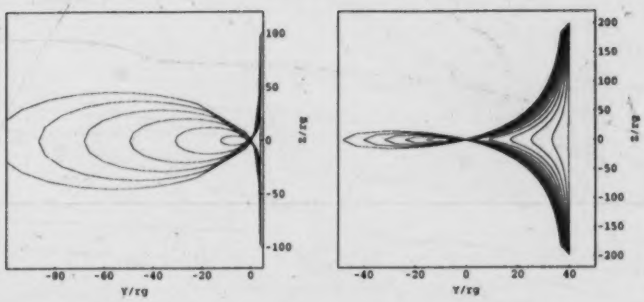

Figure 4.12: Time sequence of dust string scattering in ultra-relativistic regime. Black hole lies at origin of coordinate system. Left: Initial velocity, 0.995c, impact parameter 4.0 r_g. Right: Initial velocity, 0.76c, impact parameter 40 r_g.

$$\frac{d}{d\tau}\left[g_{\mu\nu}\frac{d\mathcal{X}^{\mu}{}_{i}}{d\tau}\frac{d\mathcal{X}^{\nu}{}_{i}}{d\tau}\right] = 0.$$

It is easy to show that

$$X^{\mu}_{i}(\tau) = (\cosh(\beta)\,\tau, \sinh(\beta)\,\tau + X_0, Y_0, \sigma_i)\ , \tag{4.24}$$

satisfies these equations and represents a straight dust string moving with velocity $v = \tanh\beta$ where the discrete σ_i mimic the σ coordinate of the cosmic string[3].

In the weak-field and ultra-relativistic cases, the role of tension in the string is made apparent by comparing the YZ projections of Figs. 4.6 and 4.9 against those of the dust string in Fig. 4.12. The dust solutions show that a loop always evolves in the dust string worldsheet. This loop is due to the Keplerian nature of the trajectories of each particle on the dust string. Particles lying on one side of the $Z = 0$ plane are deflected across this plane since their motion is constrained to an orbital plane passing through the black hole. Unlike the cosmic string, the Y-axis deflection of the dust string is unbounded (this is not to say that the deflection does not reach an asymptotic angular value). Furthermore, at the early stages the size of the loops in the dust and cosmic strings are virtually identical, reinforcing the idea that tension takes some time to assert itself. Loop formation is a generic feature of the dust string; this is not the case for the cosmic string, where loop formation is subject to the low-velocity cut-off effect discussed above.

In the strong-field regime (with $v < c$), a comparison to the dust solution is uninformative since the impact parameter is well below the critical value for particles and the portion of the dust string near the equatorial plane is captured by the black hole. However, it does reinforce the idea that internal tension plays an important role in the dynamics of the string, helping the string avoid capture for impact parameters well below that of the dust string.

[3]Although solutions to the equation of motions of test particles in the Schwarzschild geometry as used here have been given previously, e.g. [16] and [17], it is easier to integrate the dust solutions numerically and graph the results using Mathematica.

4.5 Scattering by a Rotating Black Hole

Having discussed the scattering of strings in Schwarzschild spacetime at length, the effect of black hole rotation can now be considered. As discussed in Chapter 2, the angular momentum of the black hole now introduces an additional dimension to the scattering problem. Here, the study of scattering is restricted to strings oriented along the Z-axis, that is parallel to the axis of rotation of the black hole. The terms retrograde and prograde (see Fig. 2.4) were introduced to describe the two possible cases for particle scattering. These terms will be used here also. The perturbative calculations of Chapter 3 adopted the convention $X_0 < 0$, $b = Y_0 > 0$, and $\beta > 0$ for a string oriented parallel to the Z-axis, which is also the axis of rotation of the black hole. According to Fig. 2.4, for this choice of initial conditions, prograde scattering occurs for $a < 0$; retrograde for $a > 0$.

4.5.1 Weak-field Scattering

As shown in Chapter 3, the perturbative calculations can be extended to the case of a rotating source. In this limit, perturbative solutions were tentatively derived that extended the analytic expressions to Kerr black holes, while noting that the results of this higher-order expansion could be affected by contributions from other terms in the perturbative expansion that were not accounted for in the calculations. With this cautionary note, a comparison will be made of perturbative and numerical results.

Accepting the tentative nature of perturbation solution $\chi_{(3)}$ (3.106), consider its application to the case of a straight string with initial velocity $v = \tanh\beta = 0.76c$ and impact parameter $b = Y_0 = 80M$ (see Fig. 4.13)[4], and angular momenta of $a = 0, \pm M/2$. This figure shows, like Fig. 4.1, the perturbation at late proper time, when the string is well past the black hole.

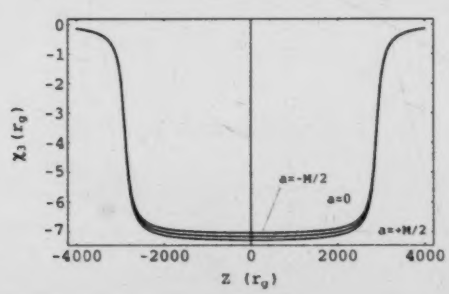

Figure 4.13: $\chi_{(3)}$ perturbation.

Figure 4.13 suggests that angular momentum affects the asymptotic deflection of the

[4]For rotating black holes, distances are measured in units of the black hole mass, M.

string, which can be estimated from perturbation solution $\chi_{(3)}$ (3.106) to be

$$A_\infty \approx -2\pi M \left(\sinh\beta + \frac{a \cosh\beta}{Y_0} \right), \tag{4.25}$$

indicating that weak-field scattering from a black hole with $a < 0$ leads to a smaller deflection than the non-rotating (Schwarzschild) case whereas $a > 0$ leads to a larger deflection.

The numerical results generated for the same initial conditions, $v = \tanh\beta = 0.76c$ and $b = Y_0 = 80M$, are shown in Fig. 4.14. The predictions derived from tentative perturbative results are compared to numerical results in Table 4.4. The numerical results show a smaller shift in amplitude as a function of black hole angular momentum, and it is clear that the perturbative results overestimate the effect. However, the perturbative results give a qualitative account of the effect of the angular momentum in that the direction of the shift due to angular momentum agrees with the numerical results. This comparison reinforces the earlier observation that a more complete perturbative calculation is required (this matter will be pursued in a subsequent publication).

Table 4.4: Scattering Parameters - Kerr Weak-field.

	a :	$+M/2$	0	$-M/2$
perturbation:	A_∞	$6.86M$	$6.81M$	$6.75M$
numerical:	A_∞	$6.858M$	$6.856M$	$6.854M$

$(v = 0.76\,c, \quad b = 40\,r_g)$

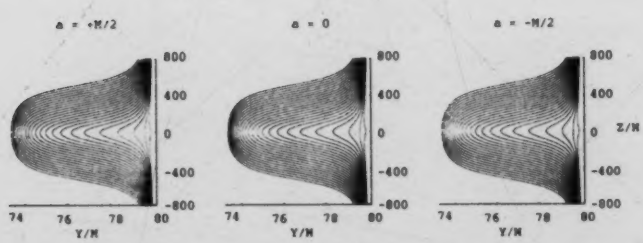

Figure 4.14: Time sequence of string scattering in weak-field regime (numerical results). Kerr black hole lies at origin of coordinate system. Initial velocity, 0.76c, impact parameter $80M$.

4.5.2 Ultra-relativistic Scattering

Noticeable differences in the shape of scattered strings due to black hole angular momentum only manifest themselves at higher velocities and shallow impact parameters. Figure 4.15 shows sections of the numerical worldsheet of an ultra-relativistic string ($v = 0.995c$) with shallow impact parameter ($b = 8.0M$) generated from the perturbative solutions.

The predictions derived from the analytic expression for deflection are compared to numerical results in Table 4.5. As already discussed, the relatively shallow impact parameter of this data set is known to be below the threshold where the perturbative solutions become inaccurate. Again, the perturbative results overestimate the effect of angular momentum. The width of the loops is not affected by angular momentum in the perturbative calculations. To the extent this could be measured from the numerical output, the numerical results also show no change in loop size.

Table 4.5: Scattering Parameters - Kerr Ultra-relativistic.

	a:	$+M/2$	0	$-M/2$
perturbation:	A_∞	67 M	60 M	53 M
numerical:	A_∞	80.8 M	79.4 M	78.2 M

($v = 0.995\,c$, $b = 4.0\,r_g$)

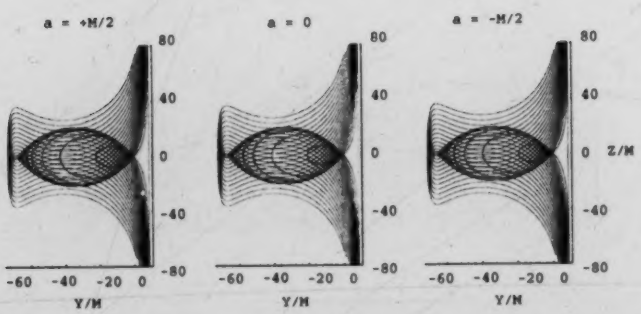

Figure 4.15: Time sequence of string scattering in ultra-relativistic regime (numerical results). Black hole lies at origin of coordinate system. Initial velocity, 0.995c, impact parameter $8.0M$.

4.5.3 Strong-field Scattering

Effects due to angular momentum are also noticeable at non-relativistic velocities and shallow impact parameters. Figure 4.16 shows sections of the numerical worldsheet of

a slow string ($v = 0.29c$) with near-critical impact parameter ($b = 5.0M$ compared to $b_{\text{capture}} = 4.2M$).

The predictions derived from the analytic expressions are compared to numerical results in Table 4.6. It can be seen that the numerical results present a much smaller range of deflections than predicted by the analytic expression (4.25). Evidently, the dynamics of strings in strong-field scattering are quite different than is suggested by the perturbative results. This is reinforced by the presence of bends in the numerical worldsheets of Fig. 4.16 that are not accounted for by the analytic results. The worldsheet of the string appears bowed towards the $Z = 0$ plane for $a = -M/2$, and away from it for $a = +M/2$. These features seem persistent in that a warp seems to remain in the shape of the string at late times. However, very long runs generated in other cases suggest that such features, though they may persist for long periods, eventually are smoothed out by tension. Long runs on this data set have not been attempted at this time.

Table 4.6: Scattering Parameters - Kerr Strong-field.

	$a:$	$+M/2$	0	$-M/2$
Perturbation:	A_∞	$5.0M$	$3.8M$	$2.4M$
Numerical:	A_∞	$3.9M$	$3.6M$	$3.3M$
$(v = 0.29\,c,$	$b = 2.5\,r_g)$			

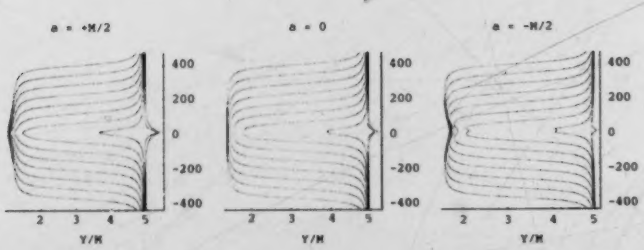

Figure 4.16: Time sequence of string scattering in strong-field regime (numerical results). Black hole lies at origin of coordinate system. Initial velocity, 0.29c, impact parameter $5.0M$.

4.6 Chapter Summary

This chapter discussed the scattering of a cosmic string by non-rotating and rotating black holes. The analysis of the weak-field approximation developed in Chapter 3 helped clarify the process of scattering. Perhaps one of the more important results to emerge from this

chapter is that numerical, weak-field analytic, and ultra-relativistic analytic results are consistent with one another in the regions of overlap.

The scattering of a string was represented at early and late times by straight string in- and out-states. The shifting of the string from one state to the other is done by kinks that propagate along the string at the speed of light. In weak-field scattering, analytic and numerical results agreed well in terms of the properties of the kinks (amplitude and width). In strong-field scattering, analytic results agreed qualitatively with numerical results. Numerical tests have shown that the weak-field approximation breaks down for $Y_0 < 10r_g$, meaning that the strong-field scattering regime occupies a much smaller region of parameter space than originally thought.

In ultra-relativistic scattering, numerical and analytic methods have shown that strings form transient loops under certain conditions, provided that the conditions $Y_0 \leq \gamma r_g$ and $Y_0 > b_{capture}$ are satisfied; this phenomenon cuts off for velocities below $\sim 0.9c$. The formation of these loops indicates that tension in the string plays a decreased role in the early stages of scattering, allowing portions of the string to exhibit dust-like behaviour.

The role of black hole angular momentum was also considered. Again, the general picture of straight-string in- and out-states was found to apply at late times. Numerical results show that black hole angular momentum altered the late-time deflection of the string but, in ultra-relativistic scattering, left the maximum width of the loops unchanged. Perturbative results were qualitatively consistent with numerical results in the relative shift in amplitude due to angular momentum (greater or smaller than the $a = 0$ case), but overestimated the magnitude of the shift. As mentioned in Chapter 3, it is quite likely that other contributions from higher-order perturbative terms also contribute to complicate the effects of black hole angular momentum.

The discussion in the next chapter turns to the special case of scattering where the impact parameter is extremely close to the critical impact parameter for capture, and further effects are observed.

Chapter 5

Cosmic String Scattering at Near-Critical Impact Parameters

The study of geodesics of particles in black hole spacetimes shows that, for impact parameters near the critical value, particles can execute multiple orbits around the black hole before escaping. This chapter discusses string scattering where the impact parameter is extremely close to the critical impact parameter for capture. In this limit, the portion of the string near the $Z = 0$ plane can dwell in the strong-field region for an extended period, leading to interesting dynamical consequences. Some similarities with particle scattering are observed, but there are also important differences that shed light on the process of string capture.

5.1 Near-critical Scattering by a Non-rotating Black Hole

Figure 5.1 compares a slice of the string worldsheet through the $Z = 0$ plane to the motion of a test particle. A comparison is made of a series of string and particle trajectories with identical velocities ($v = 0.987c$) and nearly identical impact parameters. For the particle trajectories, these range from $b = 2.60\,r_g$ through $b = 2.65\,r_g$. For the string, the impact parameters are slightly smaller, ranging from $b = 2.55\,r_g$ through $b = 2.56\,r_g$. The impact parameters at the lower end of each range result in capture, whereas those at the upper end result in scattering. It is easy to see that, even at ultra-relativistic velocities, tension influences string motion. Although the critical impact parameter for the string is very close to that for a particle, suggesting that tension plays a limited role, the dynamics of the string are, nevertheless, still governed by tension. This is made especially clear by the folded appearance of the escaping string trajectories. The escaping trajectories of the test particle are far less complicated.

There are two possible outcomes to near-critical string scattering: either the string crosses the event horizon or it scatters to infinity. However, the detailed motion of the string is highly sensitive to the initial impact parameter. Figure 5.1 shows that there are two types of capture trajectories, trajectories such as curve 1, where the string crosses the horizon directly, and curve 2, where the string folds back on itself before crossing the

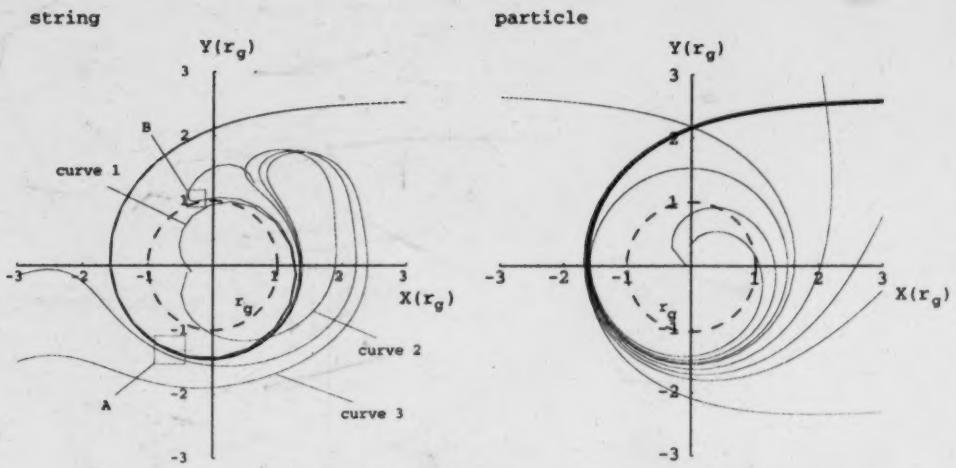

Figure 5.1: Near-critical scattering for string and test particle. $v = 0.987c$ and $r_g = 1$.

horizon. Curve 2 exhibits a loop-like feature, but does not represent a self-intersection since the intersecting points have distinct proper times. Escaping trajectories, such as curve 3, have a folded structure. There are two critical cases that mark the transition between each of these three generic curves. The transition between curves of type 1 and type 2 is marked by a structure that develops an increasingly cusp-like shape (point B in Fig. 5.1) as the impact parameter approaches the critical value that marks the boundary between type 1 and 2 curves. In practical terms, this impact parameter is difficult to obtain since it requires a large number of significant digits (curve 1 and the curve with point B have impact parameters that differ by one part in 10^5). The transition between type 2 and type 3 curves is marked by a tangent point, where the string trajectory passes twice through the same point (point A) at different times (again, no self-intersection).

The string worldsheet for these critical curves contains many twists where the string passes nearest the black hole. Figure 5.2 shows small subsets of the worldsheet for curve 3. Three views are shown, an overall view from a point of view looking up towards the black hole from a viewpoint located in the $-Y$ direction. This view shows that complicated folds that are generated as points on the string cross and recross while executing the partial orbit of the black hole. The view on the left lies in the forward direction and looks back towards the black hole. This view shows the forward self-intersection point as portions of the string cross the $Z = 0$ plane prior to beginning their partial orbit. This view also shows that these points converge again on the far side of the black hole. The third view, from the rear direction looking forward towards the black hole, shows how the string reaches a turn-around point and forms a folded structure. This fold is accompanied by a series of recrossings of various points on the string. There is no clearly defined self-intersection point, and the worldsheet evolves highly complicated folds as the points on the string retrace their

steps and scatter to infinity.

At late times, the folded features have dissipated from the worldsheet and all that remains are kinks; details of the dissipation of loops and emergence of the kinks are shown in Fig. 5.3. This Figure reinforces the observation made in Chapter 4 that the description of scattering at late times is completely understood in terms of the perturbative solutions. However, it may take a significant amount of time for the simple kink/anti-kink picture to emerge. In the case studied here, the distortions due to the close encounter persist until the string is about $1000\, r_g$ past the black hole. Whether simple analytic models can be applied the transient phenomena discussed here is an open question; perhaps a second-order perturbative expansion will yield manageable expressions from which some properties of these phenomena could be understood.

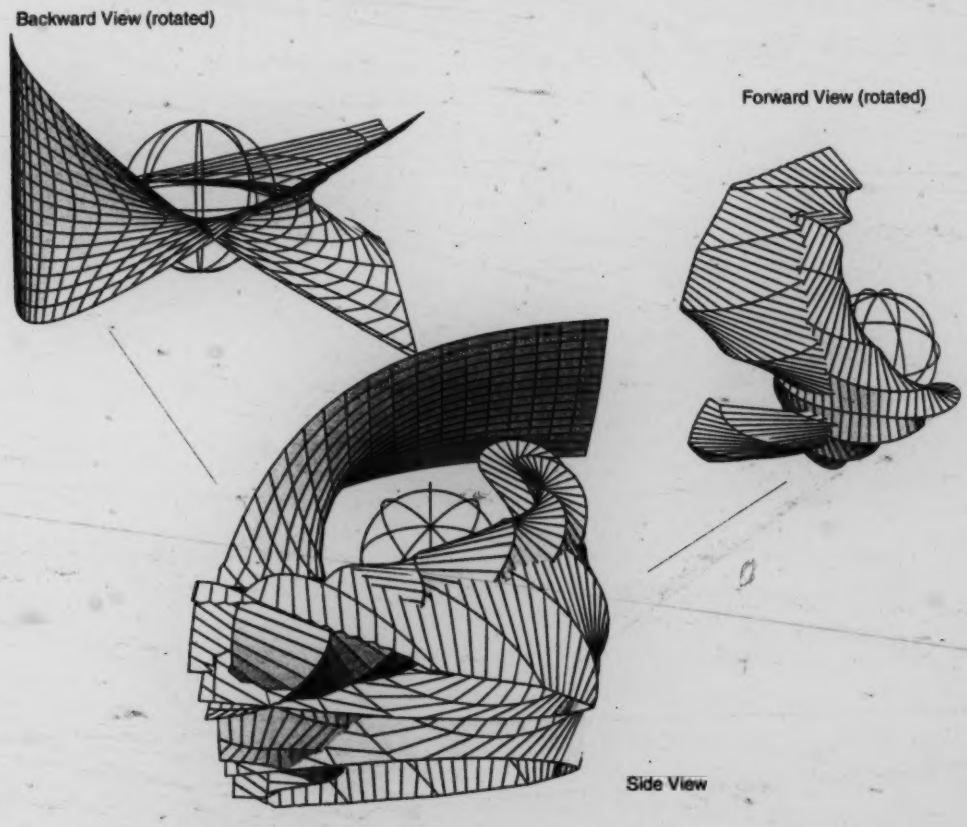

Figure 5.2: String worldsheet near $Z = 0$ plane, $v = 0.987c$.

The numerical study documented here for $\gamma = 6$ was repeated for $\gamma = 10$; a few trajectories are shown in Fig. 5.4 ($\gamma = 10$ is the largest practical value for the numerical solver).

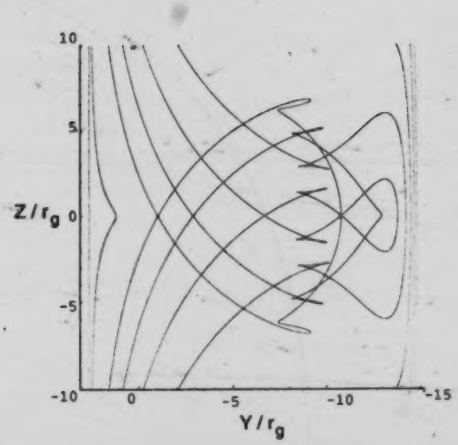

Figure 5.3: String worldsheet at late proper time, $v = 0.987c$. Loops dissipate and kinks emerge.

All observations made for the critical trajectories at lower γ apply in this case as well. The only obvious difference is that the amplitude of the folds has increased noticeably, leading to another instance of apparent intersections (again, there is no physical intersection because proper times at the intersection points are distinct). The critical impact parameter for capture lies between $b = 2.580$ and $b = 2.582$. In this narrow range of impact parameters, there is a range of "loop and capture" trajectories, such as those observed in the $\gamma = 6$ case.

5.1.1 String Capture

The trajectories shown in Fig 5.1 reveal that the critical impact parameter for capture is the value associated with a trajectory that is at the transition point between type 2 and type 3 curves. There was a conjecture made by Page [44] that the curve of critical impact parameter would have some structure due to the string reaching a stationary point under some circumstances. Figure 5.1 suggests that the capture process is quite complicated, involving a transition between a "loop and enter" trajectory and a "loop and escape" trajectory that is dynamically intricate. This looping feature is highly dependent on velocity; nevertheless, it seems that the capture curve has some structure since the transition point between the two types of trajectories is highly sensitive to initial data (more will be said about this in Chapter 6).

5.1.2 String Winding Effect

The string does not complete more than one turn about the black hole for any of the numerical runs attempted. In fact, it seems as if the transition to a "direct capture" trajectory (like curve 1 in Fig. 5.1) always occurs before a full turn is achieved. The numerical results for moderate γ-factors show that the string worldsheet folds back on itself, with no evidence of multiple windings or glory scattering. The fact that these features are

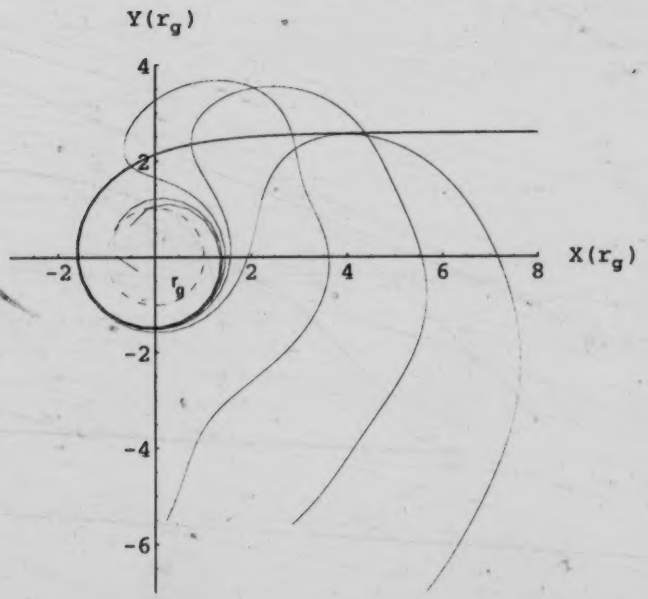

Figure 5.4: Near-critical scattering for string at $\gamma = 10$, $v = 0.995c$. Impact parameters are $b = 2.579$, 2.580, 2.582, and 2.585, and $r_g = 1$.

absent is a clear indication that the tension in remote parts of the string eventually asserts itself in all cases accessible to the numerical solver.

The fold in the worldsheet evolves after the $Z = 0$ portion of the string has almost completed a full orbit of the black hole. The question as to whether the string can complete more than one full turn and "wrap" the black hole is an open one, although numerical results suggest it is unlikely. There are three possible approaches to address this problem:

- revisit the numerical problem with a solver that can handle large γ-factors (this is done with very large grids and small step sizes),
- revisit the perturbative treatment of ultra-relativistic string motion,
- work with the null-string approximation.

The ultra-relativistic solutions given in Chapter 3 worked with the Aichelburg-Sexl form of the shock wave metric. In this approximation, the weak-field condition is still in force. Since the winding, or wrapping effect that is under study here is a strong-field one, the ultra-relativistic approach is unsuitable. In the same way that the ultra-relativistic loop formation condition was shown to be related to non-monotonicity in the Z-perturbation, the wrapping effect should manifest itself in some form of non-monotonicity in the X-perturbation. This feature is absent from the ultra-relativistic solutions of Chapter 3. In

order to study wrapping, it would be necessary to go beyond the Aichelburg-Sexl result. Such a "strong-field" shock wave expansion has already been attempted by Hayashi and Samura [33], but even their strong-field result does not exhibit the required feature. Early calculations in this form of the metric showed that the maximum turn in the string world-sheet is $\pi/2$. In a sense, the wrapping feature seems incompatible with the ultra-relativistic perturbative approach.

The other possibility is to use null strings. In the limit where a string travels at the speed of light, the tension in the string vanishes completely and the equations of motion used up to now do not apply; instead the equations for a null string should be used [18]. The equations of motion of a null string are virtually identical with those of a "dust" string of photons, with the addition of a second constraint that the tangent vectors on the null string worldsheet must remain orthogonal. It is possible to carry over knowledge of the geodesics of photons to the discussion of null strings, leading to the tentative conclusion that null strings should indeed wrap around the black hole under the right circumstances. As was discussed in [15], however, there is some question as to the physical meaning of null strings. Since the equations of motion for null strings are not directly derivable from the Nambu-Goto action, it is fair to ask whether the behaviour of the null string is an accurate representation of the ultra-relativistic limit of a cosmic string. If the null-string picture is indeed correct, then near-critical impact parameters could yield multiple windings or even glory scattering of the portion of the string near the $Z = 0$ plane, and cause extreme stretching, and perhaps breaking, since the remainder of the string would continue in the original direction of motion. Whether this is plausible remains an open question.

5.2 Near-critical Scattering by a Rotating Black Hole

As discussed in Chapter 2, the angular momentum of the black hole now introduces an additional dimension to the scattering problem. The terms retrograde and prograde (see Fig. 2.4) were introduced to describe the two possible cases for particle scattering. These terms will be used here also. Here (for historical reasons) numerical calculations adopted the convention $X_0 > 0$, $b = Y_0 > 0$, and $\beta < 0$. According to Fig. 2.4, for this choice of initial conditions, prograde scattering occurs for $a > 0$; retrograde for $a < 0$, opposite what was the case in the previous chapter.

Figure 5.5 compares a slice of the string worldsheet through the equatorial plane to the motion of a test particle for a Kerr black hole with angular momentum $a = +M/2$. For such a black hole, the horizon is located at $r_+ = 1.86M$, and is indicated in the figures by the dashed circle. A comparison is made of a series of string and particle trajectories with identical velocities ($v = 0.987c$) and nearly identical impact parameters. For the particle trajectories, these range from $b = 4.08\,M$ through $b = 4.20\,M$. For the string, the impact parameters are slightly smaller, ranging from $b = 4.00\,M$ through $b = 4.15\,M$.

It is clear from the figure that motion near a Kerr black hole differs from that of a Schwarzschild black hole. The particle and string trajectories that enter the horizon exhibit a short-lived co-rotation phase as they cross the ergosphere. Once in the interior, both

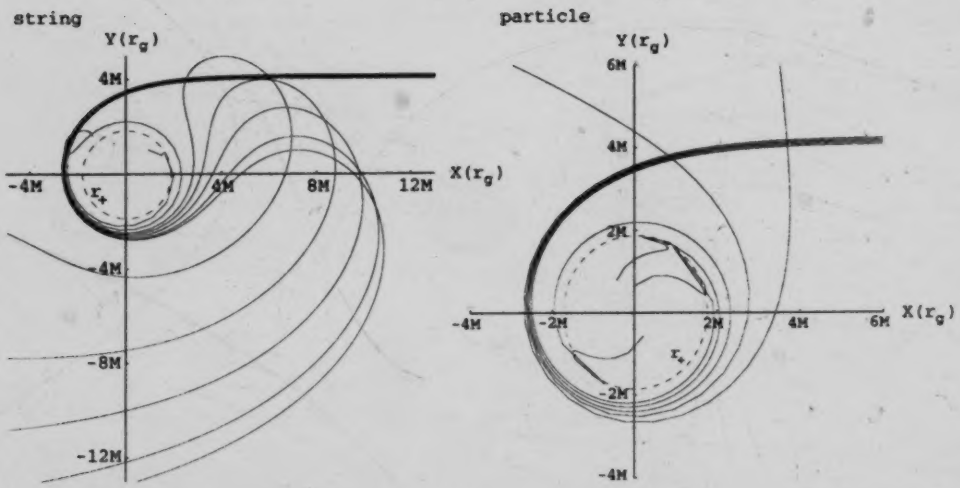

Figure 5.5: Near-critical scattering for string and test particle. $v = 0.987c$, $r_g = 1$, and $a = +M/2$. Black hole rotation is counter-clockwise.

particle and string spiral towards $r = 0$. The resolution of the geodesics in the ergosphere and interior is quite coarse since motion evolves very rapidly in terms of the proper time, and leads to visualization artifacts (i.e. the apparent formation of loops that cross and recross the horizon). Detailed views of motion of particles and strings in the ergosphere and interior of the black hole will be taken up in the next chapter.

The string trajectories exhibit many features already described in the previous section. Some string trajectories have the "loop and capture" feature already discussed; such a feature is absent from the particle trajectories. Escaping trajectories show the familiar fold, but the folds are considerably larger, since the angular momentum of the string is reinforced by the angular momentum of the black hole.

Figure 5.6 presents data for the retrograde case, $a = -M/2$. A comparison is made of a series of string and particle trajectories with identical velocities ($v = 0.987c$) and nearly identical impact parameters. For the particle trajectories, these range from $b = 6.160\,M$ through $b = 6.176\,M$. For the string, the impact parameters are slightly smaller, ranging from $b = 6.00\,M$ through $b = 6.04\,M$.

The particle trajectories that enter the horizon exhibit a short-lived reversal in direction as the particles approach and cross the ergosphere, again due to co-rotation of the string and particle with the rotation of the black hole.

The string trajectories again exhibit many features already described in the previous section. Escaping trajectories show the familiar fold, but the folds are considerably smaller. Since the string is approaching the black hole in a retrograde sense, the angular momentum of the black hole acts against the angular momentum of the string, hence reducing the magnitude of the folds. The trajectories that enter the black hole are similar to those

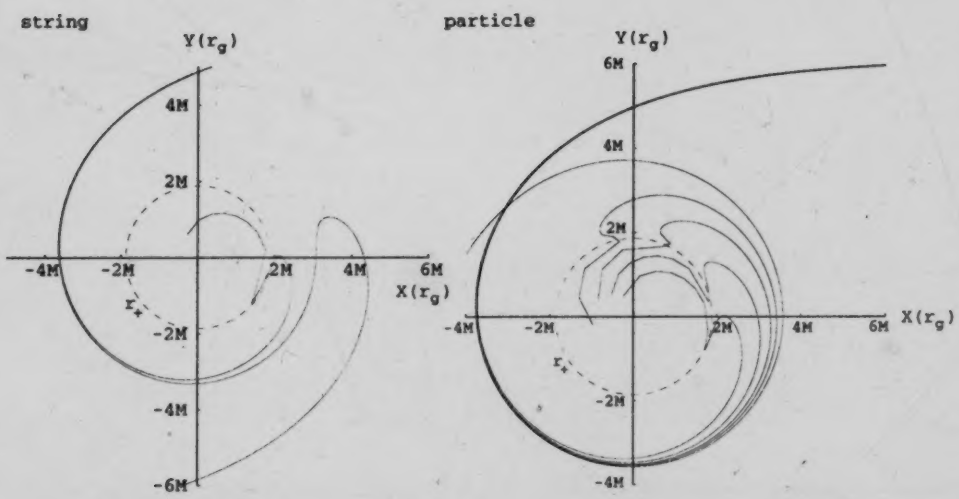

Figure 5.6: Near-critical scattering for string and test particle. $v = 0.987c$, and $a = -M/2$. Black hole rotation is clockwise.

of the particle. No "loop and capture" trajectories were observed. It is possible that they lie between the impact parameters of the last trapped trajectory and the first escaping trajectory, but this appears unlikely, and this feature may be subject to cut-off as a function of angular momentum.

5.3 Chapter Summary

The behaviour of strings with near-critical impact parameters is quite rich. Short-lived loops and folds develop in the worldsheet while the string dwells in the strong-field region of the black hole. These features dissipate over time as the string scatters, and the characteristic kink/anti-kink pattern is recovered when the string has moved well away from the black hole, as is expected from the study of motion in the weak-field region.

The near-critical scattering of relativistic strings has revealed how intricate the process of capture is. Strings can enter the black hole directly, or they may begin an escape only to be subsequently captured, the so-called "loop and capture" curves. Escaping trajectories exhibit a folded structure that progressively lessens as the impact parameter increases away from the critical value. For sufficiently large impact parameters, the more benign scattering trajectories described by the perturbative solutions are recovered.

The role of black hole angular momentum has also shed some light on the origin of the folds in the escaping trajectories: in addition to tension, string angular momentum seems to play a role in the development of those folds, and these can be amplified by the coupling of the black hole's angular momentum.

Although the numerical study of critical scattering is fascinating, it is also extremely intensive. Fine grids and small step sizes are required to obtain adequate views. Further, the extreme sensitivity to initial conditions makes the choice of impact parameters subject to costly guess-work (the Kerr solver takes roughly one day for each critical orbit). For this reason, only near-relativistic strings were considered (since the numerical solutions evolve rapidly), and a small number of values of angular momenta. Since the complexity of the trajectories seems to be a function of the amount of time spent in the strong field region, slower strings might exhibit other interesting features. However, this study would perhaps best be undertaken with more efficient numerical solvers.

For the present, it is more important to look in greater detail at the fate of trapped strings. This is the subject of the following two chapters.

Chapter 6

Capture of Cosmic Strings by a Black Hole

The capture of a cosmic string occurs when the string passes sufficiently close to the gravitational radius. After capture, the string remains attached to the black hole. If it is possible to assign a characteristic length L to the string, then its total mass is $M_{string} = \mu L$. For $\mu L \ll M$ the total mass of the string is much smaller than the mass of the black hole, and the attached string will move around the black hole while the black hole remains practically at rest. In the opposite case, $\mu L \gg M$ the black hole will be accelerated by the string. The characteristic time of this process is $T \sim vM/(\mu c^2)$. For a solar-mass black hole (10^{30} kg) and an ultra-relativistic GUT-scale string ($v \sim c$), the acceleration phase is remarkably brief: $T \sim 10s$.

The objective of the study discussed in this chapter[1] was to map the location of the capture curve both for Schwarzschild and Kerr black holes using the numerical solver[2]. The results for critical impact parameter will be compared to those for test particles. Because the string has tension, it is reasonable to expect that it would be more difficult to capture the string than a test particle moving with the same velocity and impact parameter. In other words, the capture impact parameter for a string approaching a black hole should be less than the capture impact parameter for a test particle.

This chapter is divided into three sections: the first section describes how the numerical solver was adapted to the study of string capture; the second describes string capture for Schwarzschild black holes; the third deals with non-extreme Kerr black holes.

[1]The contents of this chapter dealing with Schwarzschild black holes have been previously published in Ref. [21] and [22], and submitted for publication Ref. [23].

[2]The results cover a range of angular momenta, but the extreme Kerr spacetime, where $a = M$, has not been studied since the numerical IBVP's developed for the present study do not allow this extreme value of angular momentum. To handle extreme Kerr spacetime would require developing another version of the solver (IBVP, metric, Christoffel symbols, and derivatives of Christoffel symbols), which could not be done because of time constraints.

6.1 Description of the Numerical Method

Both numerical schemes were used for this study. Since the geodesic boundary conditions of numerical scheme B were the first to be developed, the results cited in [21] used this version of the numerical solver exclusively. Later, with the availability of the perturbative solutions, a more efficient solver for numerical scheme A was developed, and a revised capture curve was given in [23]. Results from both solvers are reported here since each helps corroborate the other in the regions where results overlap.

Prior to carrying out the study of critical impact parameter, a choice had to be made as to the coordinate system. In order to study the capture problem for Schwarzschild black holes, Eddington-Finkelstein In-going (EFI) coordinates, $(\tilde{V}, r, \theta, \phi)$, are a natural choice since they do away with the Schwarzschild coordinate singularity at the event horizon. The Christoffel symbols associated with this coordinate system, along with their derivatives with respect to the spacetime coordinates (see Appendix D), were derived and inserted as analytic expressions in the portions of the solver dealing with the initialization of the tridiagonal matrices. For similar reasons, Kerr In-going coordinates are the natural choice for studying string capture by Kerr black holes and another version of the solver was prepared using the appropriate Christoffel symbols and their derivatives (as can be seen by glancing at the lengthy expressions in Appendix D, this solver is vastly more complex and numerically intensive than its EFI counterpart). When each solver is in operation, the behaviour of the radial coordinate is monitored. When the capture condition $r(\tau, 0) < r_{\text{horizon}}$ is met, the solution is halted and the capture of the string is reported.

The procedure for scanning the parameter space to locate the critical impact parameter for capture ($b_{capture}$) is straightforward:

- Choose an initial velocity;
- For this velocity, calculate the critical impact parameter for a *particle* (see formulas in Chapter 2);
- Take the initial impact parameter for the string as

$$b_{\text{string}} := \frac{1}{2}\left(b_{\text{particle}} + r_{\text{horizon}}\right) \tag{6.1}$$

  (i.e. halfway between horizon and critical value for particle);
- Run the solver and check the outcome;
- If the string escaped (i.e. $r(\tau_{\text{final}}, 0) > r(\tau_{\text{initial}}, 0)$), repeat the run with

$$b_{\text{new}} := \frac{1}{2}\left(b_{\text{old}} + r_{\text{horizon}}\right); \tag{6.2}$$

- If the string was captured, repeat the run with

$$b_{\text{new}} := \frac{1}{2}\left(b_{\text{particle}} + b_{\text{old}}\right); \tag{6.3}$$

- Repeat this process with

$$b_{\text{new}} := \frac{1}{2}\left(b_{\text{old esc}} + b_{\text{old trap}}\right); \tag{6.4}$$

until a sufficiently precise determination of b_{capture} has been made.

The solvers (EFI and Kerr) developed for numerical scheme B relied on "manual" intervention to carry out this procedure, whereas the solvers developed later for numerical scheme A automated this procedure. For the Kerr versions, a choice is also made of angular momentum and a separate capture curve generated for each such choice.

The critical impact parameter is reported with "error bars". The lower bound indicates largest impact parameter resulting in capture, while the upper bound indicates the smallest impact parameter for which the string escaped. The value of the critical impact parameter is taken as the average of these two numbers.

6.2 Cosmic String Capture by a Non-rotating Black Hole

The capture curve for Schwarzschild black holes was obtained from three different studies. The first used the B solver to map the curve of critical impact parameter for velocities $v > 0.1c$ and different string lengths. The second used the A solver to map the curve for velocities $v > 0.03c$, overlapping the data set for the other solver. The third used the second-order perturbative expansion of Chapter 3 to obtain an analytic expression for the critical impact parameter for very low velocities. These results are assembled here to present a complete picture of string capture over the full range of velocities.

6.2.1 Results from Numerical Scheme B

The results of the numerical calculations are presented in Fig. 6.1. It shows log–log graphs of the capture impact parameter as a function of initial velocity. Dashed, dotted, and dashed-dotted lines represent capture impact parameters for strings of lengths $L = 100r_g$, $1000r_g$, and $2000r_g$, respectively.

The graph shows that for a string of finite size the capture impact parameter depends on both the length and velocity of the string, $b(v, L)$. The capture curve for the $L = 2000\,r_g$ string is definitive for velocities $v \geq 0.2c$, meaning that the capture curves for longer strings are indistinguishable in this velocity range.

The solid line represents the capture impact parameter for a test particle. As discussed in Chapter 2, the gravitational capture of test particles is well understood: a particle moving at non-relativistic velocities has a capture impact parameter $b(v)/r_g = 2/v$, while in the ultra-relativistic regime ($v \to c$), the capture impact parameter is $b(v)/r_g = 3\sqrt{3}/2$. The capture impact parameter for the ultra-relativistic particle is also the smallest capture impact parameter.

The capture curve of a cosmic string is different in many ways from that of a test particle:

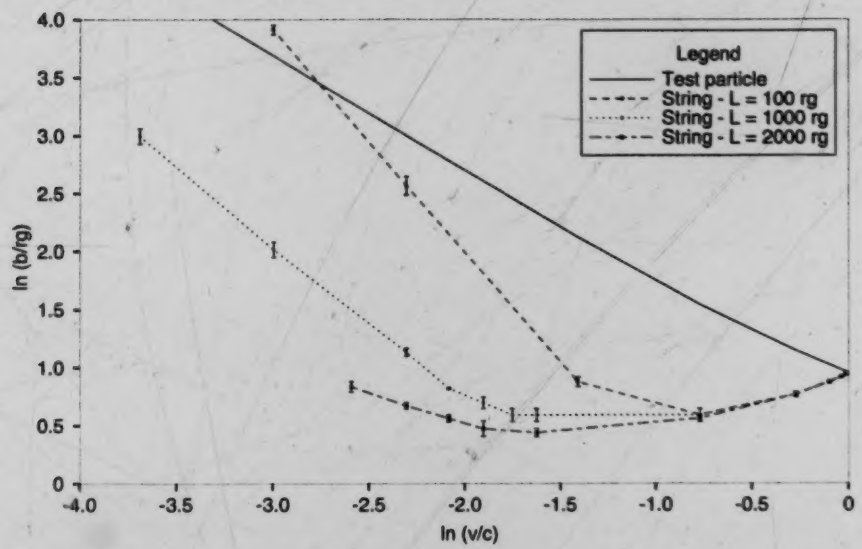

Figure 6.1: Cosmic string capture curve for Schwarzschild black hole - data from numerical scheme B.

- Unlike a test particle, the smallest capture impact parameter for a string occurs at some intermediate velocity (e.g $v \approx 0.2c$ for the $L = 2000\, r_g$ string);
- The capture impact parameter increases as $v \to c$ and $v \to 0$;
- The smallest capture impact parameter decreases with increasing string length.
- At a sufficiently low velocity, the capture curve of a (finite) string intersects the curve for the test particle;
- The capture impact parameter for strings is independent of string length for velocities approaching c, even for very short strings.

The increase in the capture impact parameter for velocities approaching the speed of light can be understood in terms of the propagation time of influences along the string. As $v \to c$, the interaction time where the string experiences the gravitational pull of the black hole becomes progressively shorter, and the influence of the black hole is felt by a shorter and shorter segment of string. For this reason, the string presents an increasingly particle-like appearance to the black hole, and the trapping behaviour of the string is determined by the portion of the string lying nearest to the $Z = 0$ plane. As $v \to c$, the capture impact parameter increases and converges on the value of the capture impact parameter for

a particle. It is reasonable to expect that in the ultimate limit, the string will behave like a particle and hence have the same capture impact parameter.

This result illustrates how the internal tension in the string helps determine its response to the gravitational field of the black hole. In the extreme relativistic limit, tension plays virtually no role since signals cannot propagate sufficiently far down the string to help influence the capture process. At lower velocities, tension plays an increasingly dominant role and helps the string avoid capture. The smallest capture impact parameter for the string is far less than that for a test particle, and occurs away from the ultra-relativistic limit.

If the string is not long enough its end points may influence the string's motion. For example, the capture curve for $L = 100 r_g$ intersects the capture curve for the test particle. This reflects the fact that for small velocities the finiteness of the string plays an important role. The trajectories of the infinitely heavy particles terminating the strings are focused by the black hole. When the strings are sufficiently long, the effect of focusing on capture is negligible. However, the boundary conditions used in the numerical work force these infinitely heavy particles to move on geodesics, so they are subject to the same capture characteristics as free test particles. This means that the end particles will be trapped by the black hole when the initial velocity becomes sufficiently small, no matter how far they are initially from the black hole. Since there is a string connecting the two particles, its behaviour will be greatly influenced by a strong focusing of the end points, and hence easily captured. For this reason, the intersection of particle and string curves is to be expected for any finite length of string. However, the initial velocity for which intersection occurs decreases with increasing string length.

6.2.2 Results from Numerical Scheme A and Perturbative Calculations

The results obtained from the A solver produce the capture curve shown in Fig. 6.2; the capture curve for $v > 0.2c$ is identical to that of the $L = 2000\, r_g$ string discussed above.

The A solver, because of its increased efficiency, was able to probe lower velocities than were possible with the B solver. These results validate two claims made in the previous section: first, that the capture curve for long strings is indeed definitive (provided focusing of end points is negligible), and is reproduced by the perturbative results; and, second, that there is indeed a minimum impact parameter at intermediate velocities, which occurs in the range of $v \approx 0.2c$ and has a value of $1.6\, r_g$. The A solver is also velocity-limited in that, at sufficiently low velocities, second-order perturbative effects become important and invalidate the first-order solutions used to set the boundary conditions. However, analytic results are available for this velocity range, and the numerical results join smoothly with the analytical result for the critical impact parameter for very low velocities, which can be derived from (3.76), taking $Y_0 \equiv b$ and noting that, for capture, $\overset{2}{X}_{(3)}\ (\tau = \infty) = b/2$, so that

$$b_{capture} \sim \frac{1}{2}\sqrt{\frac{\pi}{2v}}\,(r_g), \tag{6.5}$$

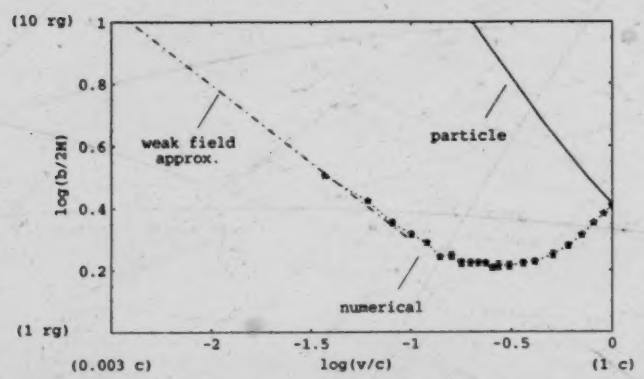

Figure 6.2: Cosmic string capture curve for Schwarzschild black hole - data from numerical scheme A and perturbative results.

and is shown as a dashed line in Fig. 6.2[3].

Further, the error bars (as defined above), are quite small for the model A solver. With such tight values for critical impact parameter, it is quite apparent that the capture curve is not a smooth line, but has some fine structure to it. This has to do with the complicated nature of the trajectory of the string for near-critical impact parameters, as mentioned in Chapter 5.

6.3 Cosmic string Capture by a Rotating Black Hole

As discussed in Chapter 2, the angular momentum of the black hole now introduces an additional dimension to the scattering problem. Here numerical calculations adopted the convention $X_0 > 0$, $b = Y_0 > 0$, and $\beta < 0$, and, as usual, the string is oriented parallel to the Z-axis, which is also the axis of rotation of the black hole. According to Fig. 2.4, for this choice of initial conditions, prograde scattering occurs for $a > 0$; retrograde for $a < 0$.

The capture curves for $a = 0, \pm M/2, \pm M/5, \pm 3\,M/4$ are shown in Fig. 6.3 for ultra-relativistic velocities (using data from the B solver).

It is clear from the curves that angular momentum shifts the capture curve up ($a < 0$; retrograde) or down ($a > 0$; prograde) relative to the Schwarzschild case. Naively, this can be understood in terms of the coupling of black hole angular momentum to the string. In the case where the string is approaching such that it co-rotates with the black hole ($a > 0$,

[3]In addition, the capture curve agrees with a recent result by Page [44] for the critical impact parameter,

$$b_{capture} \sim \frac{1}{2}\left[\sqrt{\frac{\pi}{2v}} - \left(\sqrt{\frac{\pi}{2}} + \frac{64}{15} - \sqrt{27}\right) + \frac{64}{15}v\right] (r_g). \tag{6.6}$$

This formula reproduces the general shape of the curve shown in Figure 6.2, without the fine structure that is revealed by the numerical approach.

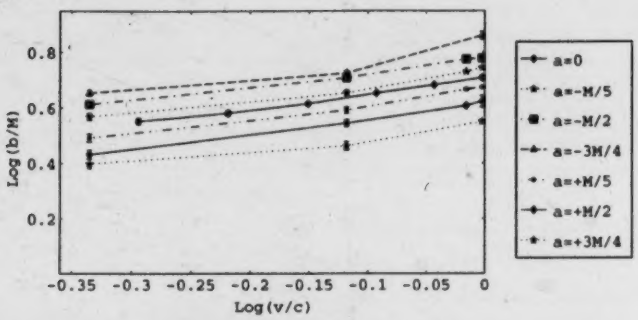

Figure 6.3: Cosmic string capture curve for Kerr black hole - Ultra-relativistic data.

$b > 0$), the string has an increased tendency to "bounce off" the black hole, and hence is more difficult to capture. The net result is that the critical impact parameter shifts *downward*; the string can come closer without trapping than it can in the Schwarzschild case. In the retrograde case, where the string is approaching a counter-rotating black hole ($a < 0$, $b > 0$), the string has an increased tendency to be dragged by the black hole in the direction opposite its original motion, and hence is more easily captured. The net result is that the critical impact parameter shifts *upward*.

The perturbative results for Kerr black holes outlined in Chapter 3 corroborate this view. Although the perturbative results are known to break down near the horizon, tests have shown that they provide a qualitative picture of string dynamics even very close to the horizon. As was discussed in Chapter 4, the magnitude of the deflection of the string towards the black hole is greater for the retrograde case than it is for $a = 0$ (Schwarzschild); a greater deflection implies an increased likelihood of capture, hence an *upward* shift of the critical impact parameter. Conversely, for the prograde, the magnitude of the deflection is less than it is for $a = 0$; a smaller deflection implies a decreased likelihood of capture, hence a *downward* shift of the critical impact parameter.

A preliminary verification that this shift of the capture curve holds for intermediate velocities is given in Fig. 6.4, where partial results of the A solver are given for a smaller set of angular momentum values. The error bars are somewhat broad, but the shift effect is nevertheless distinguishable. It appears as if the velocity at which the minimum capture impact parameter occurs ($v \approx 0.2c$) is not altered by black hole angular momentum. In light of the observations made in the preceding chapters, it is possible that the capture curves for Kerr black holes will exhibit more structure that in the Schwarzschild case when the error bars are tightened, but this remains to be determined.

A comparison to the capture of particles is also useful, using the formulas for capture impact parameter for particles (2.20), (2.22), and (2.23). Table 6.1 compares the critical impact parameters for string and particle at $v = 0.995c$. As in the Schwarzschild case, the critical impact parameters for particle and string converge, indicating that tension plays a decreased role in helping the string avoid capture. However, it is important to note that

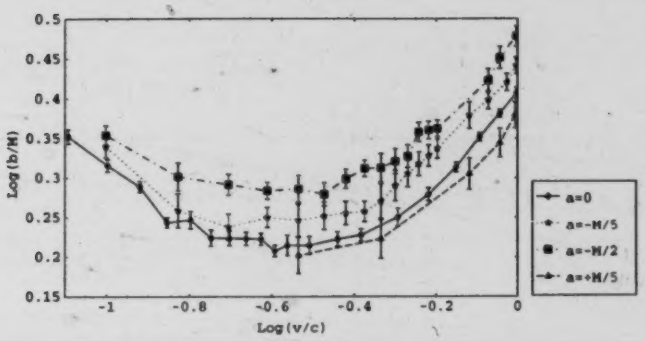

Figure 6.4: Cosmic string capture curve for Kerr black hole - non-relativistic data (preliminary).

results for string capture for $|a| = 3M/4$ do not agree with particle results, that is, the string appears to be slightly easier to capture than the particle at the ultra-relativistic limit. These results do not make sense and show that the numerical IBVP, which is known to break down completely in the limit where $a = M$, actually shows symptoms of this breakdown for smaller values of a. For this reason, the solver was restricted to the range $-M/2 \leq a \leq +M/2$ in other work.

Table 6.1: Comparison of Critical Impact Parameters - $v = 0.995c$ (Kerr).

a:	$-3M/4$	$-M/2$	$-M/5$	0	$+M/5$	$+M/2$	$+3M/4$
b_{string}:	7.24 M	6.00 M	5.55 M	5.12 M	4.72 M	4.08 M	3.55 M
b_{particle}:	6.58 M	6.14 M	5.59 M	5.20 M	5.08 M	4.10 M	3.40 M

6.4 Chapter Summary

Capture by Schwarzschild black holes was studied over the entire velocity range using numerical and analytic methods. The capture curve for strings is different than that for particles in that the capture impact parameter increases both as $v \to 0$ and $v \to c$. At the low-velocity limit, the impact parameter for the string is shown by second-order perturbation calculations to be $b \sim v^{-1/2}$ (for a particle, $b \sim v^{-1}$). At the ultra-relativistic limit, $b \to 3\sqrt{3}M$, the same result as for particles. This is due to the decreased role played by tension in determining the fate of the string at this extreme. A minimum impact parameter occurs at intermediate velocities.

The effect of black hole angular momentum was also studied numerically. In the prograde

case, the capture curve shifts downward. In the retrograde case, the capture curve shifts upward. This effect was shown to be consistent with analytic results from perturbative calculations, and it is conjectured that this shifting effect is consistent across the full velocity range.

The gravitational capture of strings by Schwarzschild black holes was discussed some time ago by Moss and Lonsdale [39]. The results shown here do not agree with these earlier results. The capture curve presented in Figure 6.2 does not resemble that of Moss and Lonsdale, neither do the details of string configurations which were discussed in previous chapters resemble the sample string configuration given by these authors. This early paper does not contain sufficient information to understand the discrepancy; since the results presented here are corroborated using several different lines of reasoning, the only conclusion that can be drawn is that this earlier paper is incorrect.

Chapter 7

Motion of a Trapped String in the Black Hole Interior

This chapter discusses preliminary results on the fate of trapped cosmic strings. Since the gravitational field inside the black hole is extremely strong, only numerical solutions are available. In principle, an expansion of the metric for small r is possible; such an expansion was attempted in the hopes that it would yield simplified equations of motion. Some simplifications are indeed possible, but they apparently do not lead to analytic solutions. This issue will be revisited at a later date; for the time being, only numerical solutions were obtained for ultra-relativistic cosmic strings and dust strings.

7.1 Description of the Numerical Method

The only significant modification to the basic EFI and Kerr solvers described in Chapter 4 is the use of a smaller step size ($\Delta\tau = \Delta\sigma/20$). Since the string evolves very quickly (in terms of string proper time τ) near to and inside the event horizon, a small step size is needed in order to adequately resolve the physical effects of string capture. In fact, without small step sizes, the tridiagonal solvers failed to converge once a substantial portion of the string had crossed the event horizon.

As usual, the constraint equations are a critical part of the validation of numerical results. All results presented herein followed the same guidelines regarding the constraint checks as discussed in Chapter 4.

7.2 Case of Non-rotating Black Hole

Figure 7.1 shows a sequence of 3D string profiles, for a cosmic string and a dust string, inside a Schwarzschild black hole (note that the scaling of the axes distorts the shape of the string). The string velocity is $v = 0.987c$ and the impact parameter of $b = 2M$ is well below the critical value for capture, $b_{\text{capture}} \approx 3\sqrt{3}M$ for the cosmic string and the dust string. These views are generated in display (i.e. Cartesian) coordinates by transforming

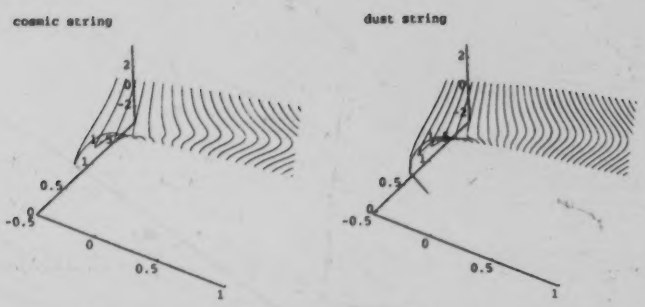

Figure 7.1: Motion in interior of Schwarzschild Black Hole. $v = 0.987c$ and $b = 2M$. Axes are in dimensionless units X^i/M.

from the EFI coordinates of the solver using the formulas given in Appendix E. It is clear from the picture that the fate of the cosmic string is not different from that of a particle (or dust string) in this respect: once trapped by a black hole, the string is drawn towards the central singularity on a very short time scale. The solver was unable to track the solution when the string reached a radial distance of $\sim 0.1\, r_g$ and reached an automatic stop when the tridiagonal solver failed to converge on a solution. Constraints were fairly well maintained during the latter stages. It is also clear from the picture that the motion of the cosmic string and the dust string are very similar, suggesting that, once inside the black hole, string tension plays a very minor role. This is not entirely surprising considering that gravity is dominant in black hole interiors.

7.3 Case of Rotating Black Hole

A three-dimensional view of string motion in the interior of a Kerr black hole can also be generated, but the resulting display is almost meaningless in display coordinates[1]. This is because of the complicated dynamics that arise when portions of the string cross the ergosphere on their way to the horizon. The first portion of the string to enter the ergosphere is that which lies in the equatorial plane of the black hole (the $Z = 0$ plane in display coordinates). This portion is dragged by the black hole and co-rotates until it crosses the event horizon. As the portions of the string lying off the equatorial plane enter the ergosphere, they also co-rotate before crossing the horizon. In terms of string proper time, the process is very rapid. Nevertheless the string worldsheet develops a highly tangled appearance that is very difficult to visualize. The clearest representation is that which is restricted to the portion of the string lying in the equatorial plane.

Figure 7.2 compares the motion of the cosmic string and the dust string for $a = -M/2,\, 0,\, +M/2$. It can be seen that the fate of the dust and cosmic strings is virtually

[1]The string worldsheet is very smooth in the original Kerr coordinates, but these are not intuitive coordinates for the visualizations presented here.

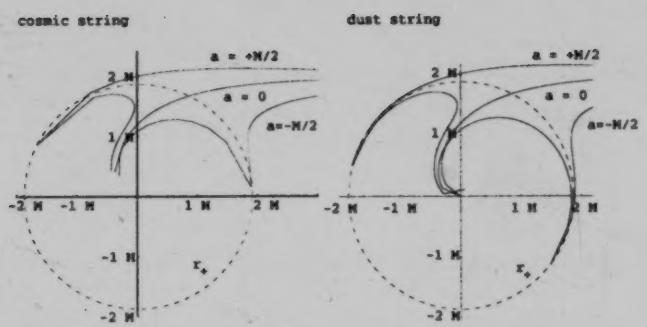

Figure 7.2: Motion in interior of Kerr and Schwarzschild Black Holes (equatorial plane). $v = 0.987c$ and $b = 2M$.

indistinguishable. This observation also holds for the portions of the string lying off the equatorial plane, where both the cosmic and dust strings display the same tangled structure as they approach and cross the event horizon. Once inside the black hole, string motion is less agitated and, as in the Schwarzschild case, the string evolves very rapidly (a matter of a few time steps) towards the center. Constraint calculations show that the solution is no longer reliable in the very late stages, and the solution displays large oscillations that are numerical (and not physical) in origin. These last time steps were removed from the graph[2].

Because of the nature of the numerical solvers, it is not possible to study the behaviour of the parts of the string that remain outside the black hole for very long (i.e. until the interior portions force the solver to shut down). In order to obtain an adequate late-time view of disturbances propagating along the string, a method would have to be found of removing the portions of the string that lie inside the black hole from the numerical evolution. This is an open issue.

[2]In principle, the numerical solutions can track the motion closer to $r = 0$ given a finer numerical grid and smaller step size, but these solutions are far too numerically intensive to pursue at this stage.

Chapter 8

Discussion

The preceding chapters discussed the dynamics of cosmic strings in different regions of the (b, v) parameter space (shown in Fig. 1.2). Perturbative solutions were derived to describe the motion of strings in weak gravitational fields; numerical schemes were developed to study motion in weak and strong gravitational fields, including the interior of black holes. In all cases where there was overlap, numerical and perturbative results were consistent. The method that underlies all numerical work is based on a novel non-linear extension of the Von Neumann discretization of the wave equation; this numerical method has proven to be robust and reliable, and has allowed investigations to be pursued where analytical methods are not applicable. Furthermore, this numerical method should be applicable to other system of non-linear wave equations, and it should also be possible to extend the numerical method to handle more spatial dimensions.

8.1 Summary of Findings

The scattering of cosmic strings in the weak-field, ultra-relativistic, and strong-field regimes revealed many aspects of string dynamics that were unanticipated when this study was first undertaken. With the two-pronged approach of numerical simulations and analytical calculations, the solution of the equations of motion of the cosmic string yielded many interesting results:

Weak-field Scattering - After passing the black hole, the string is displaced in the direction perpendicular to its velocity vector and towards the black hole. This shift was explained in terms of the flux of the Newtonian gravitational field through the string world-sheet, and is accomplished by two kinks that propagate along the string at the speed of light. Besides providing a quantitative understanding of the scattering and capture of cosmic strings by black holes at large impact parameters, the weak-field approximation provided the conceptual framework for describing scattering in the strong field since the early and late phases of strong-field scattering are well described by the in- and out-states derived from the analysis of weak-field scattering. Black hole angular momentum was shown to have long-lived effects that alter the value of the asymptotic deflection of the string; angular

momentum enters the deflection formula as a correction to the (first-order) Schwarzschild expressions. The effect of angular momentum was found (numerically) to be small; perturbative calculations tended to overestimate its effect, suggesting that the calculations for angular momentum were subject to higher-order corrections that were not factored in.

Ultra-relativistic Regime - Scattering in the limit where the string velocity approaches the speed of light, yet has a sufficiently large impact parameter, can be treated using the weak-field solutions. However, more manageable solutions were obtained by transforming the Schwarzschild metric to that of a shock wave spacetime. Scattering in the ultra-relativistic regime exhibited a new feature: the formation of transient loops in the string shortly after periastron, provided that the conditions $b \leq \gamma r_g$ and $b > b_{capture}$ are satisfied. These loops arise because gravity dominates string tension in the early stages of scattering; when the string emerges once again in the weak-field region, tension reasserts itself and the loops are unwound into outward-moving kinks. The numerical solver established that the loop-formation phenomenon cuts off for velocities below $\sim 0.9c$. Black hole angular momentum, as in the non-relativistic case, altered the amplitude of the string deformations but left the amplitude of the loops unchanged. Again, the effect was very small and perturbative results tended to overestimate the effect.

Strong Field Regime - Scattering in the strong-field regime bears a general resemblance to weak-field scattering in that kinks are formed (without loops for $v < 0.9c$) and propagate outward after the string reaches periastron. At relativistic velocities, transient loops are also seen to form (for $v > 0.9c$). However, the amplitude of the kinks and the maximum width of the loops are larger than predicted by the perturbative formulas. Black hole angular momentum again altered the amplitude of the string deformations. The effect of angular momentum was more pronounced here, suggesting that only near-critical encounters are significantly affected by black hole rotation.

Breakdown of Weak-field Approximation - Numerical studies showed that the weak-field approximation breaks down for $b < 20\,M$; this is a surprisingly small value, and suggests that the analytic expressions are a good approximation of string dynamics even for strings with relatively small impact parameters.

Near-critical Impact Parameters - When the cosmic string approaches the black hole with an impact parameter that is very close to the critical value for capture, the behaviour of the string is extremely sensitive to initial conditions. It was shown that there are two characteristic trajectories for capture, the first where the string enters directly after partially wrapping itself around the black hole, the second where the string evolves a small loop before crossing the horizon. The trajectory of a cosmic string that avoids capture is significantly different from that of a dust string. Instead of winding a number of times around the black hole, as is the case for the dust string, the cosmic string evolves a folded structure after partially wrapping itself. This fold appears to be persistent up to moderate γ-factors (in fact, up to the practical limit of the numerical solvers), revealing that tension is not entirely absent from the strong-field dynamics of ultra-relativistic strings.

Capture - The location of the capture curve in parameter space was mapped using the numerical solvers, and supplemented with a perturbative analysis for very low velocities. Together, these results yielded a composite picture of the string capture curve over the entire

velocity range. The capture impact parameter grows for both small and large values of v/c, and hence there exists a velocity v for which the capture impact parameter has minimum value. This minimum occurred for $v \approx 0.2c$ for rotating and non-rotating black holes. The numerical results also demonstrated that for ultra-relativistic velocities the critical impact parameter $b_{capture}$ reaches the same value as the capture parameter for the ultra-relativistic particles. This result supports the earlier observation that tension becomes less effective at helping a string avoid capture when $v \to c$. The angular momentum of the black hole shifted the capture curve up or down in parameter space. This effect was understood in terms of the effect of angular momentum in the weak-field regime, extrapolated to the strong-field case where capture occurs.

Interior Preliminary work on the motion of strings in the interior of a black hole (subsequent to capture) indicates that, as expected, gravity dominates the dynamics of the string. Little difference is observed between cosmic string and dust strings, and strings are inexorably drawn inward. As in the case of particle motion, string motion in the interior occurs very rapidly in terms of proper time. Numerical solutions had to be carefully controlled because of this.

8.2 Future Research

The numerical solver and the perturbative methods developed in the course of this study have allowed many aspects of the interaction of cosmic strings and black holes to be investigated, at least at a preliminary level. These techniques should now be applied to more elaborate studies.

As mentioned in preceding chapters, a number of areas remain to be investigated:

- Resolving the wrapping "problem" (Schwarzschild case) using either an improved numerical method or shock wave expansion; results from this study should help settle how a string behaves at the ultra-relativistic limit.
- High-resolution capture curve for Schwarzschild and Kerr black holes; this study will provide a better understanding of string capture and should suggest further investigations of string dynamics for near-critical impact parameters (chaotic behaviour in such cases is anticipated).
- Scattering and capture for extreme Kerr spacetime, in order to extend the description of string dynamics to all possible values of black hole angular momentum.
- High-resolution views of trapped strings, and the late-time behaviour of the exterior parts of the string.

These will be the subject of subsequent papers. In addition, it appears as if an investigation of gravitational radiation from string scattering might be fruitful, and may offer an opportunity for experimental detection of cosmic strings by space-based gravitational wave observatories.

There has been a good deal of work done on the radiation produced by encounters between test particles and black holes and, more recently, by extended bodies (including black hole/black hole coalescence). The following facts can be extracted from the literature (see, e.g. [5] and [6]):

- Black holes radiate in quasi-normal modes, which are strongly damped oscillations of the event horizon;
- Quasi-normal modes are excited by ultra-relativistic particles and extended objects;
- Black holes are largely insensitive to scattered particles, and only near misses excite the quasi-normal modes;
- Quasi-normal modes are characteristic of the black hole.

Cosmic strings, being extended objects, should excite the quasi-normal modes of a black hole in the process of scattering (or trapping), and will also radiate themselves as the kinks that characterise scattering form and propagate outward, especially in a near-critical encounter where the string dwells in the strong-field region and becomes highly distorted. It would seem as if string/black hole encounters could be interesting sources of bi-modal radiation, with a high-frequency component due to ringing of the black hole, and a low-frequency component associated with large-scale deformations of the string.

As was shown earlier, a cosmic string can pass very close to a black hole without being captured. The deformation of the string has a characteristic length scale of the order of the black hole diameter ($L \sim 2\,r_g$) and takes place on a time scale that is of the order of $t \sim \frac{2r_g}{v}$, the time taken to cross the diameter of the black hole.

Using the expression for power radiated by a quadrupole source (see, e.g., Vilenkin [52]),

$$\dot{E} = \frac{G}{c^5} M^2 L^4 \omega^6 , \tag{8.1}$$

where M and L are the mass and length of the string along with the relation for the amplitude of the radiation signal at an Earth-based detector (see Thorne [48]),

$$h \approx 4 \left(\frac{G}{c^4}\right) \left(\frac{\ddot{Q}}{r_E}\right) , \tag{8.2}$$

where r_E is the distance from the Earth to the source and Q the quadrupole moment, and introducing the characteristic length and time scales for an encounter between GUT-scale cosmic string and a black hole yields

$$h \approx \frac{10^{-3}}{r_E} \left(\frac{v}{c}\right)^5 \left(\frac{M_{BH}}{M_{sol}}\right) . \tag{8.3}$$

where M_{BH} is the mass of the black hole and M_{sol} is the mass of the sun.

A large galactic core black hole ($\sim 10^9$ solar masses) should generate a signal in the 10^{-4} Hz frequency range with an amplitude that could lie above the noise threshold of

proposed space-based detectors (the frequency is far below the lowest frequencies accessible to Earth-based detectors).

Although a full numerical investigation of string capture and the gravitational radiation emitted by the string/black hole system appears to be beyond the capabilities of present computers, it is possible to obtain preliminary results on the radiation from the string only, using the weak-field approximation discussed in Chapter 3. For an extended, weak source such as this, a method described by Weinberg [54] allows direct calculation of a radiation solution.

From the findings discussed in this document, it appears as if the dynamical interaction of a cosmic string with a black hole is a source of rich, and perhaps even surprising, behaviours. It is hoped that the results discussed here have helped clarify some aspects the interaction of two of the more exotic types of objects in our universe.

Bibliography

[1] Aichelburg, P.C., and Sexl, R.U. *On the gravitational field of a massless particle.* Gen. Rel. Grav. **2**, 303-312 (1971).

[2] Albrecht, A. and York, T. *Topological picture of cosmic string self-intersection.* Phys. Rev. **D38**, 2958-2962 (1988).

[3] Amati,D., and Klimcik, C. *Strings in a shock wave background and generation of curved geometry from flat-space string theory.* Phys. Lett. **B210** 92-96 (1988).

[4] Ames, W.F. *Non-linear Partial Differential Equations in Engineering.* Academic Press (1965).

[5] Anninos, P., Hobill, D., Seidel, E., Smarr, L., and Suen, W.-M. *Collision of two black holes.* Phys. Rev. Lett. **71**, 2851-2854 (1993).

[6] Anninos, P., Hobill, D., Seidel, E., Smarr, L., and Suen, W.-M. *Head-on collision of two equal-mass black holes.* Phys. Rev. **D52**, 2044-2059 (1995).

[7] Barbashov, B.M. *Some solutions of the equations of motion of a relativistic string with massive ends.* Nucl. Phys., **B129**, 175-188 (1977).

[8] Barbashov, B.M. and Chervyakov, A.M. *New formulation of the classical dynamics of the relativistic string with massive ends.* J. Phys., **A24**, 2443-2460 (1991).

[9] Barbashov, B.M. and Chervyakov, A.M. *Action-at-a-distance and equations of motion of a system of two massive points connected by a relativistic string.* Theor. Math. Phys., **89**, 1087-1098 (1991).

[10] Barton, G. *Elements of Green's functions and propagation: potentials, diffusion, and waves.* Oxford University Press (1989).

[11] Bondelli, S. *Divide and conquer: a parallel algorithm for the solution pf a tridiagonal linear system of equations.* Parallel Computing, **17**, 419-434 (1991).

[12] Boyer, R.H., and Lindquist, R.W. *Maximal analytic extension of the Kerr metric.* J. Math. Phys. **8**, 265-281 (1967).

[13] Carter, B., and Frolov, V.P. *Separability of string equilibrium equations in generalized Kerr-de Sitter background.* Class. Quant. Grav. **6** 569-580 (1989).

[14] Castellvi, P., Jaen, X., and Llanta, E. *TTC: Symbolic tensor and exterior calculus.* Computers in Physics **8**, 360-367 (1994).

[15] Dabrowski, M.P., and Larsen, A.L. *Null strings in Schwarzschild spacetime.* Phys. Rev. **D55**, 6409-6414 (1997). Preprint, **hep-th/9610243.**

[16] Darwin, Sir C. *The gravity field of a particle.* Proc. Roy. Soc. London **A249** , 180-194 (1959).

[17] Darwin, Sir C. *The gravity field of a particle II.* Proc. Roy. Soc. London **A263** , 39-50 (1961).

[18] De Vega,H.J., and Nicolaidis, A. *Strings in strong gravitational fields.* Phys. Lett. **B 295** 214-218 (1992).

[19] De Villiers, J.P. *Divide and conquer block-tridiagonal solvers.* Canadian Network for Space Research Report 94-07.

[20] De Villiers, J.P. *Dynamics of Cosmic Strings in Schwarzschild Spacetime.* Proceedings of Seventh Canadian Conference on General Relativity and Relativistic Astrophysics (Fall 1997). **gr-qc9706040.**

[21] De Villiers, J.P., and Frolov, V.P. *Gravitational Capture of Cosmic Strings by a Black Hole.* To appear in Int. J. Mod. Phys. **D7** No. 6 (December 1998).

[22] De Villiers, J.P., and Frolov, V.P. *Scattering of Straight Cosmic Strings by Black Holes: Weak Field Approximation.* To appear in Phys. Rev. **D58** No. 6 (October 1998).

[23] De Villiers, J.P., and Frolov, V.P. *Gravitational Scattering of Cosmic Strings by Non-Rotating Black Holes.* (paper under preparation).

[24] Frolov, V.P., Hendy, S., and De Villiers, J.P. *Rigidly rotating strings in stationary axisymmetric spacetimes.* Class. Quant. Grav. **14**, 1099-1114 (1997).

[25] Frolov, V.P., Hendy, S., and Larsen, A.L. *How to create a two-dimensional black hole.* Phys. Rev. **D54**, 5093-5102 (1996).

[26] Frolov, V.P., and Larsen, A.L. *Propagation of perturbations along strings.* Nucl. Phys. **B414**, 129-146 (1988).

[27] Frolov, V.P., and Novikov, I.D. *Physics of Black Holes.* Kluwer Academic Press (1989).

[28] Frolov, V.P., and Sanchez, N. *Instability of accelerated strings and the problem of limiting acceleration.* Nucl. Phys. **B349** 815-838 (1991).

[29] Frolov, V.P., Skarzhinsky, V.D., Zelnikov, A.I., and Heinrich, O. *Equilibrium configurations of a cosmic string near a rotating black hole.* Phys. Lett. **B224**, 255 (1989).

[30] Gibbons, G.W. and Perry, M.J. *Quantizing gravitational instantons.* Nucl. Phys. **B146**, 90-108 (1978).

[31] Goldstein, H.H. *Classical mechanics.* 2^{nd} *ed.* Addison-Wesley (1980).

[32] Gradshteyn, I.S., and Ryzhik, I.M. *Table of Integrals, Series, and Products.* 5^{th} *ed.* Academic Press (1994).

[33] Hayashi,K., and Samura, T. *Gravitational shock waves for Schwarzschild and Kerr black holes.* Phys. Rev. **D50** 3666-3673 (1994).

[34] Hindmarsh, M.B., and Kibble, T.W.B. *Cosmic strings.* Preprint hep-ph/9411342.

[35] Hirsch, C. *Numerical Computation of Internal and External Flows - Volume 1, Fundamentals of Numerical Discretization.* Wiley (1988).

[36] Kerr, R. P. *Gravitational field of a spinning mass as an example of algebraically special metrics.* Phys. Rev. Lett. **11**, 237-238 (1963).

[37] Kibble, T.W.B. *Topology of cosmic domains and strings.* J. Phys. **A**, 1387 (1976).

[38] Kibble, T.W.B. *Some implications of cosmological phase transitions.* Phys. Rep. **67** (1980) 183.

[39] Lonsdale, S. and Moss, I. *The motion of cosmic strings under gravity.* Nucl. Phys. **B298**, 693-700 (1988).

[40] Misner,C.W., Thorne, K.S., and Wheeler, J.A. *Gravitation.* W.H. Freeman, San Francisco (1973).

[41] Morse, P.M., and Feshbach, H. *Methods of Theoretical Physics.* McGraw-Hill (1953).

[42] Nakahara, M. *Geometry, Topology, and Physics.* IOP Publishing (1990).

[43] Nielsen, H.B., Olesen, P. *Vortex-line models for dual strings.* Nucl. Phys. **B61**, 4496 (1973)

[44] Page, D.N. *Gravitational Capture and Scattering of Straight Test Strings with Large Impact Parameters.* Preprint, **Alberta Thy 05-98; gr-qc/9804088.**

[45] Polyakov, A.M. *Quantum geometry of bosonic strings.* Phys. Lett. **B103**, 207-210 (1981).

[46] Ramond, P. *Quantum Field Theory: a modern primer.* Benjamin-Cummings (1981).

[47] Stark, P.A. *Introduction to Numerical Methods.* Macmillan, 1970.

[48] Thorne, K.S. *Gravitational Waves.* gr-qc/9506086

[49] Vilenkin, A. *Cosmological density fluctuations produced by vacuum strings.* Phys. Rev. Lett. **46**, 1169-1172 (1981).

[50] Vilenkin, A. *Cosmic Strings and Domain Walls.* Phys. Rep. **121**, 263-315 (1985).

[51] Vilenkin, A. *Correspondence.* (1998).

[52] Vilenkin, A., and Shellard, E. P. S. *Cosmic Strings and Other Topological Defects.* (Cambridge Univ. Press, Cambridge) (1994).

[53] Weinstock, R. *Calculus of variations with applications to physics and engineering.* Dover (1974).

[54] Weinberg, S. *Gravitation and Cosmology: Principles and Applications of the General Theory of Relativity.* Wiley (1972).

[55] Zeldovich, Ya. B. *Cosmological fluctuations produced near a singularity.* Mon. Not. R. astr. Soc. **192**, 663-667 (1980).

Appendix A

Variational Calculations

This appendix supplements the derivation of the equations of motion for a cosmic string terminated by massive particles discussed in Chapter 3. Many authors have carried out similar derivations for strings with massive end particles (see, e.g., [7], [8], and [9]) using the Nambu-Goto action. The derivations shown here for the Polyakov form of the Nambu-Goto action are new.

In Chapter 3 the Polyakov action was extended to include massive end points,

$$\begin{aligned} S[X^\mu, h_{AB}, \sigma_i] &= -\mu \int_{\tau_1}^{\tau_2} d\tau \int_{\sigma_1(\tau)}^{\sigma_2(\tau)} d\sigma \sqrt{-h}\, h^{AB} G_{AB} \\ &\quad - \sum_{i=1}^{2} \frac{m_i}{2} \int_{\lambda_1}^{\lambda_2} d\lambda\, g_{\mu\nu} \frac{dX_i^\mu}{d\lambda} \frac{dX_i^\nu}{d\lambda}, \end{aligned} \tag{A.1}$$

where the string tension μ has been explicitly shown, and $\lambda = \lambda(\tau)$ is the most general parametrization for the boundaries X_i^μ, from which,

$$\frac{dX_i^\mu}{d\lambda} = \left(\frac{\partial X_i^\mu}{\partial \tau} + \frac{\partial X_i^\mu}{\partial \sigma} \dot{\sigma}_i(\tau) \right) \dot{\lambda}^{-1}. \tag{A.2}$$

Using Eqn. (A.2), it is possible to rewrite Eqn. (A.1) as

$$\begin{aligned} S[X^\mu, h_{AB}, \sigma_i] &= -\mu \int_{\tau_1}^{\tau_2} d\tau \int_{\sigma_1(\tau)}^{\sigma_2(\tau)} d\sigma \sqrt{-h}\, h^{AB} G_{AB} \\ &\quad - \sum_{i=1}^{2} \frac{m_i}{2} \int_{\tau_1}^{\tau_2} d\tau\, g_{\mu\nu} \left(\frac{\partial X_i^\mu}{\partial \tau} + \frac{\partial X_i^\mu}{\partial \sigma} \dot{\sigma}_i \right) \left(\frac{\partial X_i^\nu}{\partial \tau} + \frac{\partial X_i^\nu}{\partial \sigma} \dot{\sigma}_i \right) \dot{\lambda}^{-1}. \end{aligned} \tag{A.3}$$

The equations of motion are obtained by taking the h_{AB}, x^μ, and σ_i variations of the action. Since the bounds of integration are finite, the variations must take into account contributions from the interior of the (τ, σ) plane, denoted D in Fig. 3.1, and bounded by $\tau_0 < \tau < \tau_1$ and $\sigma_1(\tau) < \sigma < \sigma_2(\tau)$, as well as the boundary of D. In order to obtain the most general equations possible, it will be assumed that the extremizing functions for

the free string action are not prescribed on the σ boundaries (however, the extremizing functions are assumed to vanish on the τ boundaries). The above action functional consists of three distinct "pieces", a functional for the string interior (the free string action) and functionals for each massive end point,

$$S[\mathcal{X}^\mu, h_{AB}, \sigma_i] \equiv S_{string}[\mathcal{X}^\mu, h_{AB}] + \sum_{i=1}^{2} S_i[\mathcal{X}^\mu, \sigma_i]. \tag{A.4}$$

A.1 Variations on Interior Region

The free-string action S_{string} is a functional of both string position, $\mathcal{X}^\mu$, and the internal metric, h_{AB}, so variations with respect to each of these quantities must be computed[1].

First, the variation with respect to $\mathcal{X}^\mu$

$$\left.\frac{\delta S_{string}}{\delta \mathcal{X}^\mu}\right|_D \tag{A.5}$$

is computed using[2]

$$\frac{\partial f}{\partial \mathcal{X}^\mu} - \frac{\partial}{\partial \tau}\left(\frac{\partial f}{\partial \mathcal{X}^\mu_{,\tau}}\right) - \frac{\partial}{\partial \sigma}\left(\frac{\partial f}{\partial \mathcal{X}^\mu_{,\sigma}}\right) = 0 \tag{A.9}$$

where $f = \sqrt{-h}\, h^{AB}\, g_{\rho\eta}(\mathcal{X}^\lambda)\mathcal{X}^\rho_{,A}\, \mathcal{X}^\eta_{,B}$. The contributions to the variations are

$$\begin{aligned} \frac{\partial f}{\partial \mathcal{X}^\mu} &= \frac{\partial}{\partial \mathcal{X}^\mu}\left\{\sqrt{-h}\, h^{AB}\, g_{\rho\eta}(\mathcal{X}^\lambda)\, \mathcal{X}^\rho_{,A}\, \mathcal{X}^\eta_{,B}\right\} \\ &= \sqrt{-h}\, h^{AB}\, g_{\rho\eta,\lambda}(\mathcal{X}^\lambda)\, \mathcal{X}^\rho_{,A}\, \mathcal{X}^\eta_{,B}\, \delta^\lambda_\mu \end{aligned} \tag{A.10}$$

$$\frac{\partial f}{\partial \mathcal{X}^\mu_{,C}} = \sqrt{-h}\, h^{AB}\, g_{\rho\eta}(\mathcal{X}^\lambda)\left(\mathcal{X}^\rho_{,A}\, \delta_{BC}\, \delta^{\eta\mu} + \mathcal{X}^\eta_{,B}\, \delta_{AC}\, \delta^{\rho\mu}\right) \tag{A.11}$$

and

---

[1] These calculations also apply to the conventional case where the domain D is unbounded.

[2] For a general integral defined on a 2-dimensional space, (see, for instance, Weinstock [53]),

$$I_2 = \int\int_D dx\, dy\, f(x, y, w, w_x, w_y), \tag{A.6}$$

the function w that extremizes the integral is determined by the following PDEs:

$$\frac{\partial f}{\partial w} - \frac{\partial}{\partial x}\left(\frac{\partial f}{\partial w_x}\right) - \frac{\partial}{\partial y}\left(\frac{\partial f}{\partial w_y}\right) = 0 \tag{A.7}$$

on the interior of region D, and by

$$\frac{\partial f}{\partial w_x}\frac{dy}{ds} - \frac{\partial f}{\partial w_y}\frac{dx}{ds} = 0 \tag{A.8}$$

on the boundary of region D.

$$\frac{\partial}{\partial \zeta^D}\left(\frac{\partial f}{\partial \mathcal{X}^\mu_{,C}}\right) = \left(\sqrt{-h}\,h^{AB}\right)_{,D} g_{\rho\eta}(\mathcal{X}^\lambda)\left(\mathcal{X}^\rho_{,A}\,\delta_{BC}\,\delta^{\eta\mu} + \mathcal{X}^\eta_{,B}\,\delta_{AC}\,\delta^{\rho\mu}\right) \tag{A.12}$$
$$+ \sqrt{-h}\,h^{AB}\,g_{\rho\eta,\lambda}(\mathcal{X}^\lambda)\left(\mathcal{X}^\rho_{,A}\,\delta_{BC}\,\delta^{\eta\mu} + \mathcal{X}^\eta_{,B}\,\delta_{AC}\,\delta^{\rho\mu}\right)\mathcal{X}^\lambda_{,D}$$
$$+ \sqrt{-h}\,h^{AB}\,g_{\rho\eta}(\mathcal{X}^\lambda)\left(\mathcal{X}^\rho_{,AD}\,\delta_{BC}\,\delta^{\eta\mu} + \mathcal{X}^\eta_{,BD}\,\delta_{AC}\,\delta^{\rho\mu}\right)$$

where indices $C, D = 0, 1$.

Combining, factoring, and relabelling indices, Eqn. (A.9) becomes

$$0 = \sqrt{-h}\,h^{AB}\left(g_{\rho\eta,\mu} - g_{\mu\eta,\rho} - g_{\rho\mu,\eta}\right)\mathcal{X}^\rho_{,A}\,\mathcal{X}^\eta_{,B} \tag{A.13}$$
$$- 2\left(\sqrt{-h}\,h^{AB}\,g_{\mu\nu}\,\mathcal{X}^\nu_{,AB} + \left(\sqrt{-h}\,h^{AB}\right)_{,A} g_{\mu\nu}\,\mathcal{X}^\nu_{,B}\right)$$

With

$$\Box := \frac{1}{\sqrt{-h}}\,\partial_A\left(\sqrt{-h}\,h^{AB}\,\partial_B\right) \tag{A.14}$$

and

$$\Gamma_{\nu\rho\eta} := \frac{1}{2}\left(g_{\nu\eta,\rho} + g_{\rho\nu,\eta} - g_{\rho\eta,\nu}\right) \tag{A.15}$$

then, Eqn. (A.9) becomes

$$0 = -2\sqrt{-h}\left(g_{\mu\nu}\,\Box\mathcal{X}^\nu + \Gamma_{\nu\rho\eta}\,h^{AB}\,\mathcal{X}^\rho_{,A}\,\mathcal{X}^\eta_{,B}\right) \tag{A.16}$$
$$= -2\sqrt{-h}\,g_{\mu\nu}\left(\Box\mathcal{X}^\nu + \Gamma^\nu_{\rho\eta}\,h^{AB}\,\mathcal{X}^\rho_{,A}\,\mathcal{X}^\eta_{,B}\right)$$

and it follows that the equations of motion are,

$$\Box\mathcal{X}^\mu + \Gamma^\mu_{\rho\eta}\,h^{AB}\,\mathcal{X}^\rho_{,A}\,\mathcal{X}^\eta_{,B} = 0 \tag{A.17}$$

Second, the variation with respect to h_{AB}

$$\left.\frac{\delta S_{string}}{\delta h_{AB}}\right|_D \tag{A.18}$$

is computed using

$$\frac{\partial f}{\partial h_{AB}} - \frac{\partial}{\partial \tau}\left(\frac{\partial f}{\partial h_{AB,\tau}}\right) - \frac{\partial}{\partial \sigma}\left(\frac{\partial f}{\partial h_{AB,\sigma}}\right) = 0 \tag{A.19}$$

where $f = \sqrt{-h}\,h^{AB}\,G_{AB}$. Care must be taken in handling the covariant and contravariant indices of metric h, but the calculations are straightforward since there are no metric derivatives $h_{AB,C}$ in the action. It is straightforward to show that Eqn. (A.19) becomes

$$0 = \frac{\partial f}{\partial h_{AB}} = \sqrt{-h}\left(G^{AB} - \frac{h^{AB}}{2}\,G^C{}_C\right) \tag{A.20}$$

where $G^C{}_C = h^{BC} G_{BC}$. It follows that the equations of constraint are,

$$G^{AB} - \frac{h^{AB}}{2} G^C{}_C = 0 \tag{A.21}$$

The choice on the internal metric $h_{AB} = e^{2\gamma(\tau,\sigma)}\eta_{AB} \equiv \eta_{AB}$ is justified in Chapter 3 and leads to equations of motion (3.18).

A.2 Variations on Boundary

On the boundary of region D, there are contributions from both free-string action S_{string} and the action of the massive particles S_i, which is a functional of both particle position, X_i^μ and the parameter σ_i, so variations with respect to each of these quantities must be computed. Since there are no contributions on the τ boundaries, τ_0 and τ_1, only the boundaries $\sigma_i(\tau)$ are of concern.

First, the variation with respect to $\mathcal{X}^\mu$ of the free string action

$$\left.\frac{\delta S_{string}}{\delta \mathcal{X}^\mu}\right|_{\partial D} \tag{A.22}$$

is computed using

$$\frac{\partial f}{\partial \mathcal{X}^\mu_{,\tau}}\frac{d\sigma_i}{d\tau} - \frac{\partial f}{\partial \mathcal{X}^\mu_{,\sigma}}\frac{d\tau}{d\tau} = \frac{\partial f}{\partial \mathcal{X}^\mu_{,\tau}}\dot{\sigma}_i - \frac{\partial f}{\partial \mathcal{X}^\mu_{,\sigma}} \tag{A.23}$$

where $f = \sqrt{-h}\, h^{AB}\, g_{\rho\eta}\, \mathcal{X}^\rho_{,A}\, \mathcal{X}^\eta_{,B}$. The contributions to the variations are as given in (A.11) and it follows that Eqn. (A.23) becomes

$$\sqrt{-h}\, h^{AB}\, g_{\rho\eta} \left\{ \left(\mathcal{X}^\rho_{,A}\, \delta_{B0}\, \delta^{\eta\mu} + \mathcal{X}^\eta_{,B}\, \delta_{A0}\, \delta^{\rho\mu} \right) \dot{\sigma}_i - \left(\mathcal{X}^\rho_{,A}\, \delta_{B1}\, \delta^{\eta\mu} + \mathcal{X}^\eta_{,B}\, \delta_{A1}\, \delta^{\rho\mu} \right) \right\} \tag{A.24}$$

Second, the variation with respect to h_{AB} of the free string action

$$\left.\frac{\delta S_{string}}{\delta h_{AB}}\right|_{\partial D} \tag{A.25}$$

is automatically zero since there are no terms $h_{AB,C}$ in the action.

Third, the variation with respect to X_i^μ of the end point action

$$\left.\frac{\delta S_i}{\delta X_i^\mu}\right|_{\partial D} \tag{A.26}$$

is computed using[3]

$$\frac{\partial f}{\partial X_i^\mu} - \frac{d}{d\tau}\left(\frac{\partial f}{\partial X_{i,\tau}^\mu}\right) \tag{A.29}$$

where $f = m_i\, g_{\rho\eta}\, X_{i,\tau}^\rho\, X_{i,\tau}^\eta$.

The calculations are similar to those already shown in the previous section and lead to

$$m_i\, g_{\mu\nu}\left(\frac{d^2 X_i^\nu}{d\lambda^2} + \Gamma_{\rho\eta}^\nu \frac{d X_i^\rho}{d\lambda}\frac{d X_i^\eta}{d\lambda}\right), \tag{A.30}$$

Since the combined variations must vanish, that is Eqns. (A.23) and (A.29) add to 0, it follows that the equations of motion are,

$$\begin{aligned}\sqrt{-h}\, h^{AB}\, g_{\mu\nu}\left\{\left(\mathcal{X}_{,A}^\nu\, \delta_{B0} + \mathcal{X}_{,B}^\nu\, \delta_{A0}\right)\dot{\sigma}_i - \left(\mathcal{X}_{,A}^\nu\, \delta_{B1} + \mathcal{X}_{,B}^\nu\, \delta_{A1}\right)\right\} \; + \\ m_i\, g_{\mu\nu}\left(\frac{d^2 X_i^\nu}{d\lambda^2} + \Gamma_{\rho\eta}^\nu \frac{d X_i^\rho}{d\lambda}\frac{d X_i^\eta}{d\lambda}\right) \;=\; 0\,, i = 1,2\,.\end{aligned} \tag{A.31}$$

which can be expanded to

$$\begin{aligned}2\sqrt{-h}\, g_{\mu\nu}\left(h^{00}\, \mathcal{X}_{,\tau}^\nu\, \dot{\sigma}_i - h^{11}\, \mathcal{X}_{,\sigma}^\nu + \frac{h^{01}+h^{10}}{2}\left(\mathcal{X}_{,\sigma}^\nu\, \dot{\sigma}_i - \mathcal{X}_{,\tau}^\nu\right)\right) \; + \\ m_i\, g_{\mu\nu}\left(\frac{d^2 X_i^\nu}{d\lambda^2} + \Gamma_{\rho\eta}^\nu \frac{d X_i^\rho}{d\lambda}\frac{d X_i^\eta}{d\lambda}\right) \;=\; 0\,, i = 1,2\,.\end{aligned} \tag{A.32}$$

Finally, there are also "equations of motion" for the boundary points arising from the σ_i variation of the end point action. To do this variation, use the second expression for the action, (A.3), for which the Euler-Lagrange equation reads, for each end point,

$$\begin{aligned}0 \;=\; & \frac{m_i}{\dot{\lambda}}\left\{g_{\mu\nu}\left(\frac{\partial^2 X_i^\mu}{\partial\tau^2} + \Gamma_{\rho\eta}^\mu \frac{\partial X_i^\rho}{\partial\tau}\frac{\partial X_i^\eta}{\partial\tau}\right)\frac{\partial X_i^\nu}{\partial\sigma}\right. \\ & + \; 2\dot{\sigma}_i\left[g_{\mu\nu}\frac{\partial^2 X_i^\mu}{\partial\tau\,\partial\sigma}\frac{\partial X_i^\nu}{\partial\sigma} + \frac{1}{2}\frac{\partial g_{\mu\nu}}{\partial X_i^\rho}\frac{\partial X_i^\rho}{\partial\tau}\frac{\partial X_i^\mu}{\partial\sigma}\frac{\partial X_i^\nu}{\partial\sigma}\right] \\ & + \; \dot{\sigma}_i^2\left[g_{\mu\nu}\frac{\partial^2 X_i^\mu}{\partial\sigma^2}\frac{\partial X_i^\nu}{\partial\sigma} + \frac{1}{2}\frac{\partial g_{\mu\nu}}{\partial X_i^\rho}\frac{\partial X_i^\rho}{\partial\sigma}\frac{\partial X_i^\mu}{\partial\sigma}\frac{\partial X_i^\nu}{\partial\sigma}\right] \\ & + \left.\ddot{\sigma}_i\, g_{\mu\nu}\left(\frac{\partial X_i^\mu}{\partial\sigma}\frac{\partial X_i^\nu}{\partial\sigma}\right) - \frac{\ddot{\lambda}}{\dot{\lambda}}\, g_{\mu\nu}\left(\frac{\partial X_i^\mu}{\partial\tau} + \frac{\partial X_i^\mu}{\partial\sigma}\dot{\sigma}_i\right)\frac{\partial X_i^\nu}{\partial\sigma}\right\}.\end{aligned} \tag{A.33}$$

[3]For a general action functional defined on a 1-dimensional space,

$$I_1 = \int dx\, f\,(x, y, y') \tag{A.27}$$

the function y that extremizes the integral is determined by the Euler-Lagrange equation,

$$\frac{\partial f}{\partial y} - \frac{d}{dx}\left(\frac{\partial f}{\partial y'}\right) = 0 \tag{A.28}$$

For the boundaries, it is necessary to unravel Eqns. (A.32) and (A.33). To do this, two physical conditions are imposed on the system. First, assume the end points to be very massive, and hence consider the limiting case where m_i tend to infinity. Second, assume that the initial string time τ_1 and parameter $\lambda(\tau_1)$ agree at the boundaries. Along with these conditions, a conformal reparametrization of the internal metric leaves the freedom to specify the boundary functions; this fact is used to apply the condition that σ_i are constant functions, namely, $\sigma_i = \pm\frac{\pi}{2}$. This simplifies the equations of motion of the boundary points and yields information on the parametrization $\lambda(\tau)$. (Note: With this choice, the σ parameter is bounded in the conventional fashion, $-\frac{\pi}{2} \leq \sigma \leq \frac{\pi}{2}$.)

This choice of boundary function reduces Eqn. (A.32) to

$$m_i \left(\frac{d^2 X_i^\nu}{d\lambda^2} + \Gamma^\nu_{\rho\eta} \frac{dX_i^\rho}{d\lambda} \frac{dX_i^\eta}{d\lambda} \right) - 2\mu\sqrt{-h} \left(h^{11} \frac{\partial \mathcal{X}^\nu}{\partial \sigma} + \frac{h^{01}+h^{10}}{2} \frac{\partial \mathcal{X}^\nu}{\partial \tau} \right) = 0 \,, \quad \text{(A.34)}$$

or,

$$\frac{d^2 X_i^\nu}{d\lambda^2} + \Gamma^\nu_{\rho\eta} \frac{dX_i^\rho}{d\lambda} \frac{dX_i^\eta}{d\lambda} = \frac{2\mu\sqrt{-h}}{m_i} \left(h^{11} \frac{\partial \mathcal{X}^\nu}{\partial \sigma} + \frac{h^{01}+h^{10}}{2} \frac{\partial \mathcal{X}^\nu}{\partial \tau} \right) . \quad \text{(A.35)}$$

Taking the limit of infinite mass, the geodesic equation is obtained,

$$\frac{d^2 X_i^\nu}{d\lambda^2} + \Gamma^\nu_{\rho\eta} \frac{dX_i^\rho}{d\lambda} \frac{dX_i^\eta}{d\lambda} = 0 \,. \quad \text{(A.36)}$$

The choice of boundary function reduces Eqn. (A.33) to

$$2\dot{\lambda}^{-1} g_{\mu\nu} \left[\left(\frac{\partial^2 X_i^\mu}{\partial \tau^2} + \Gamma^\mu_{\rho\eta} \frac{\partial X_i^\rho}{\partial \tau} \frac{\partial X_i^\eta}{\partial \tau} \right) \frac{\partial X_i^\nu}{\partial \sigma} - \dot{\lambda}^{-1} \ddot{\lambda} \frac{\partial X_i^\mu}{\partial \tau} \frac{\partial X_i^\nu}{\partial \sigma} \right] = 0 \,. \quad \text{(A.37)}$$

This result imposes conditions on the parametrization $\lambda(\tau)$. The first term in parentheses is interesting; the equations of motion for the boundary points are "recovered", parametrized this time by τ. Further, it is clear that $\dot{\lambda}(\tau) = 0$ is not allowed. In order for the above expression to hold, it is necessary to satisfy $\partial_\tau^2 \lambda = 0$ subject to the initial condition that the string and end point times be "synchronized",

$$\lambda(\tau_1) = \tau_1 \,. \quad \text{(A.38)}$$

The required parametrization is, therefore,

$$\lambda(\tau) = \tau \,. \quad \text{(A.39)}$$

For this parametrization, the equations of motion for the end points become

$$\frac{d^2 X_i^\mu(\tau,\sigma_i)}{d\tau^2} + \Gamma^\mu_{\rho\eta} \frac{dX_i^\rho(\tau,\sigma_i)}{d\tau} \frac{dX_i^\eta(\tau,\sigma_i)}{d\tau} = 0 \quad ; \quad \sigma_i = \pm\frac{\pi}{2} \,. \quad \text{(A.40)}$$

To summarize, the equations of motion consist of two pieces, the equations for the string proper, and boundary conditions that describe the physics at the edges of the computational domain:

$$\frac{\partial^2 \mathcal{X}^\mu}{\partial \tau^2} + \Gamma^\mu_{\rho\eta} \frac{\partial \mathcal{X}^\rho}{\partial \tau} \frac{\partial \mathcal{X}^\eta}{\partial \tau} = \frac{\partial^2 \mathcal{X}^\mu}{\partial \sigma^2} + \Gamma^\mu_{\rho\eta} \frac{\partial \mathcal{X}^\rho}{\partial \sigma} \frac{\partial \mathcal{X}^\eta}{\partial \sigma} \,; \left(-\frac{\pi}{2} < \sigma < \frac{\pi}{2}\right) \quad \text{(A.41)}$$

$$\frac{d^2 X_i^\mu}{d\tau^2} + \Gamma^\mu_{\rho\eta} \frac{dX_i^\rho}{d\tau} \frac{dX_i^\eta}{d\tau} = 0 \,; \sigma_i = \pm\frac{\pi}{2} \,. \quad \text{(A.42)}$$

Appendix B

Discretization of the Equations of Motion and Constraints

This appendix[1] discusses the discretization of the equations of motion and constraints of the cosmic string and the implementation of the boundary conditions for both models (perturbative and geodesic boundary points).

The motion of a cosmic string in an external spacetime is described by the equation for the string proper

$$\frac{\partial^2 \mathcal{X}^\mu}{\partial \tau^2} + \Gamma^\mu_{\rho\eta} \frac{\partial \mathcal{X}^\rho}{\partial \tau} \frac{\partial \mathcal{X}^\eta}{\partial \tau} - \frac{\partial^2 \mathcal{X}^\mu}{\partial \sigma^2} - \Gamma^\mu_{\rho\eta} \frac{\partial \mathcal{X}^\rho}{\partial \sigma} \frac{\partial \mathcal{X}^\eta}{\partial \sigma} = 0\,, \tag{B.1}$$

along with boundary conditions that depend on the numerical model.

For numerical scheme A, where the ends of the string move in a weak gravitational field, the ends of the string must satisfy initial data

$$\mathcal{X}^\mu(\tau_0, \sigma) = X^\mu(\tau_0, \sigma) + \delta X^\mu(\tau_0, \sigma)\,, \tag{B.2}$$

and the boundary conditions

$$X^\mu_i = X^\mu(\tau, \sigma_i) + \delta X^\mu(\tau, \sigma_i)\,, \tag{B.3}$$

where δX^μ are the perturbations documented in Chapter 3.

For numerical scheme B, a string terminated by massive particles, the string must satisfy initial data

$$\mathcal{X}^\mu(\tau_0, \sigma) = X^\mu(\tau_0, \sigma)\,, \tag{B.4}$$

where X^μ is the Minkowski analytic solution documented in Chapter 3, along with the boundary conditions

$$\frac{d^2 X^\mu_i}{d\tau^2} + \Gamma^\mu_{\rho\eta} \frac{dX^\rho_i}{d\tau} \frac{dX^\eta_i}{d\tau} = 0\,. \tag{B.5}$$

[1] A less detailed version of this appendix has been previously published in Ref. [21].

The equations of motion and their boundary conditions must be discretized. The task appears quite complicated due to the presence of the Christoffel symbols, $\Gamma^{\mu}_{\rho\eta}$, which are derivatives of the spacetime metric. However, these are known analytic functions of the spacetime coordinates and, since the spacetime is taken to be non-dynamical, the Christoffel symbols enter the equations of motion as pre-defined, albeit somewhat complicated, functions of the string position. The role of the Christoffel symbols is to couple the equations of motion; in addition, they are also non-linear functions of the spacetime coordinates, and can give the equations of motion a very complicated structure. However, the only portions of Eqns. (B.1) and (B.5) that require discretization are the first- and second- order derivatives.

The non-linear terms in Eqn. (B.1) are potentially troublesome. For instance, one of the Christoffel symbols for the radial coordinate for a Schwarzschild black hole of mass M is given by

$$\Gamma^{1}_{11} \equiv \Gamma^{r}_{rr} = -\frac{M}{r\,(r-2M)}\,, \tag{B.6}$$

and grows without bound as the radial coordinate approaches the event horizon $r_g = 2M$. A discretization based on this particular type of black hole and coordinate system must therefore be used only for cosmic strings moving at a reasonable distance away from the event horizon; other coordinate systems (e.g. Eddington-Finkelstein) are available to follow the motion of the string near to and across the event horizon.

In devising a numerical method to solve the equations of motion (B.1), a number of points were considered:

- the cosmic string is a large, extended object; only a small portion of the string is likely to probe the highly non-linear region of spacetime near a black hole,
- the degree of coupling between the equations can vary considerably during the evolution of the solution,
- the cosmic string can travel at any speed, up to ultra-relativistic velocities (arbitrarily close to the speed of light).

For these reasons, a robust, implicit finite difference solver was sought.

B.1 Von Neumann's Method - Linear Case

Ames [4] describes a discretization due to Von Neumann for the linear wave equation,

$$\frac{\partial^2 u}{\partial \tau^2} = \frac{\partial^2 u}{\partial \sigma^2}\,, \tag{B.7}$$

which uses a standard second-order finite difference formula for evaluating the time derivative at the discrete grid point (i, j),

$$\left(\frac{\partial^2 u}{\partial \tau^2}\right)_{i,j} \approx \frac{u_{i,j+1} - 2\,u_{i,j} + u_{i,j-1}}{(\Delta\tau)^2}\,. \tag{B.8}$$

This formula is second order accurate in the temporal grid spacing ($\Delta\tau$). A similar expression holds for the spatial derivative, but here the actual finite difference expression is created from an average

$$\begin{aligned}\left(\frac{\partial^2 u}{\partial \sigma^2}\right)_{i,j} &\approx \frac{\lambda}{(\Delta\sigma)^2}\left(u_{i+1,j+1} - 2\,u_{i,j+1} + u_{i-1,j+1}\right) \\ &+ \frac{(1-2\lambda)}{(\Delta\sigma)^2}\left(u_{i+1,j} - 2\,u_{i,j} + u_{i-1,j}\right) \\ &+ \frac{\lambda}{(\Delta\sigma)^2}\left(u_{i+1,j-1} - 2\,u_{i,j-1} + u_{i-1,j-1}\right) \qquad \text{(B.9)}\end{aligned}$$

that is second order accurate in the spatial grid spacing ($\Delta\sigma$). Here, the spatial derivative at the current grid point is the weighted average (weighted by the factor λ) of the spatial derivatives at the current, previous, and next time steps. This averaging gives rise to a 9-point implicit scheme; the scheme is referred to a 9-point since there are three grid points required at each of three time levels, and implicit since the spatial derivative involves the unknown "j+1" time step whose solution is sought in order to advance the solution forward in time. Ames shows that this scheme is unconditionally stable for $\frac{1}{4} \leq \lambda \leq \frac{1}{2}$.

In order to generalize Von Neumann's discretization to the non-linear wave equation of interest here, a number of extensions must be made to the basic scheme:

1. Generalize the discretization to handle 4-vectors
2. Linearize the terms containing Christoffel symbols
3. Modify the temporal discretization to allow an adaptive step size

The third consideration is important for two reasons: first, the motion of the cosmic string will take place in a background where the non-linear terms contribute either very little (well away from the event horizon, for instance) or a great deal, so that the option must exist to stride over large time increments in uninteresting areas; second, the linearization scheme (an iterative method is used) may require smaller time steps when the contribution of non-linear terms becomes significant and convergence of the solution is difficult to obtain. These considerations require that an adaptive time step size be available.

B.2 Vector-Matrix Notation for Equations of Motion

In order to simplify the formulation of the complete finite-difference expression which is to be coded in FORTRAN, a vector and matrix representation of the equations of motion will be adopted. Denote the 4-vector describing the position of the string as $\left(x^0, x^1, x^2, x^3\right) = \mathbf{x}$. The Christoffel symbols that are part of the non-linear terms can be represented as 4-vectors

of 4x4 matrices,

$$\Gamma^{\nu}_{\rho\sigma}\,\frac{\partial x^{\rho}}{\partial \zeta^{A}}\,\frac{\partial x^{\sigma}}{\partial \zeta^{A}} = \begin{bmatrix} \left(\frac{\partial \mathbf{x}}{\partial \zeta^{A}}\right)^{T} \Gamma^{0} \left(\frac{\partial \mathbf{x}}{\partial \zeta^{A}}\right) \\ \left(\frac{\partial \mathbf{x}}{\partial \zeta^{A}}\right)^{T} \Gamma^{1} \left(\frac{\partial \mathbf{x}}{\partial \zeta^{A}}\right) \\ \left(\frac{\partial \mathbf{x}}{\partial \zeta^{A}}\right)^{T} \Gamma^{2} \left(\frac{\partial \mathbf{x}}{\partial \zeta^{A}}\right) \\ \left(\frac{\partial \mathbf{x}}{\partial \zeta^{A}}\right)^{T} \Gamma^{3} \left(\frac{\partial \mathbf{x}}{\partial \zeta^{A}}\right) \end{bmatrix} \equiv \left(\frac{\partial \mathbf{x}}{\partial \zeta^{A}}\right)^{T} \bar{\Gamma} \left(\frac{\partial \mathbf{x}}{\partial \zeta^{A}}\right) ; \bar{\Gamma} = \begin{bmatrix} \Gamma^{0} \\ \Gamma^{1} \\ \Gamma^{2} \\ \Gamma^{3} \end{bmatrix} , \quad \text{(B.10)}$$

where $\zeta^{A} = \tau$ or σ, $\left(\frac{\partial \mathbf{x}}{\partial \zeta^{A}}\right)^{T}$ is the transpose of the 4-vector form of the derivative, and Γ^{μ} denotes the 4×4 matrix of Christoffel symbols for the given upper index μ.

With this notation, the equations of motion (B.1) can now be written in vector-matrix form,

$$\frac{\partial^{2} \mathbf{x}}{\partial \tau^{2}} + \left(\frac{\partial \mathbf{x}}{\partial \tau}\right)^{T} \bar{\Gamma} \left(\frac{\partial \mathbf{x}}{\partial \tau}\right) = \frac{\partial^{2} \mathbf{x}}{\partial \sigma^{2}} + \left(\frac{\partial \mathbf{x}}{\partial \sigma}\right)^{T} \bar{\Gamma} \left(\frac{\partial \mathbf{x}}{\partial \sigma}\right) . \quad \text{(B.11)}$$

B.3 Discretization of the Derivatives

As a first step in developing discretized expressions for Eqn. (B.11), express the 4-vector in a manner compatible with a numerical grid

$$\mathbf{x} \rightarrow \mathbf{x}_{i,j} , \quad \text{(B.12)}$$

where i is a spatial index associated with discrete values of the σ coordinate, and j is a temporal index associated with discrete values of the τ coordinate. The following standard finite difference expressions for the first and second order derivatives of the position 4-vector $\mathbf{x}$ (see, for instance, Hirsch [35]) will be referenced throughout this Appendix.

The first-order spatial derivative is handled using a standard centered difference,

$$\left(\frac{\partial \mathbf{x}}{\partial \sigma}\right)_{i,j} \approx \frac{\mathbf{x}_{i+1,j} - \mathbf{x}_{i-1,j}}{2\,\Delta\sigma} \equiv D_{\sigma}\mathbf{x}_{i,j} . \quad \text{(B.13)}$$

The second-order spatial derivative is also discretized using a standard centered difference, denoted $D^{2}_{\sigma}\mathbf{x}_{i,j}$, but in keeping with Von Neumann's method, is expressed as an average at three adjacent time levels,

$$\left(\frac{\partial^{2} \mathbf{x}}{\partial \sigma^{2}}\right)_{i,j} \approx \lambda\, D^{2}_{\sigma}\mathbf{x}_{i,j+1} + (1 - 2\,\lambda)\; D^{2}_{\sigma}\mathbf{x}_{i,j} + \lambda\, D^{2}_{\sigma}\mathbf{x}_{i,j-1} , \quad \text{(B.14)}$$

where,

$$D^{2}_{\sigma}\mathbf{x}_{i,j} \equiv \frac{(\mathbf{x}_{i+1,j} - 2\,\mathbf{x}_{i,j} + \mathbf{x}_{i-1,j})}{(\Delta\sigma)^{2}} . \quad \text{(B.15)}$$

The discretized time (τ) derivatives need to be modified to handle a non-uniform mesh. The formulation of such expressions is based on forward and backward differences,

$$\left(\frac{\partial \mathbf{x}}{\partial \tau}\right)_{i,j} \approx \frac{\mathbf{x}_{i,j+1} - \mathbf{x}_{i,j}}{\Delta \tau_j} \, (forward), \tag{B.16}$$

and,

$$\left(\frac{\partial \mathbf{x}}{\partial \tau}\right)_{i,j} \approx \frac{\mathbf{x}_{i,j} - \mathbf{x}_{i,j-1}}{\Delta \tau_{j+1}} \, (backward), \tag{B.17}$$

where $\Delta \tau_j$ represents the time increment between levels j-1 and j, and $\Delta \tau_{j+1}$ represents the time increment between levels j and j+1. Similar expressions hold for second-order derivatives.

These forward and backward differences are combined to yield

$$\begin{aligned} \left(\frac{\partial \mathbf{x}}{\partial \tau}\right)_{i,j} &\approx \frac{1}{\Delta \tau_j + \Delta \tau_{j+1}} \left\{ \frac{\Delta \tau_j}{\Delta \tau_{j+1}} \left(\mathbf{x}_{i,j+1} - \mathbf{x}_{i,j}\right) + \frac{\Delta \tau_{j+1}}{\Delta \tau_j} \left(\mathbf{x}_{i,j} - \mathbf{x}_{i,j-1}\right) \right\} \\ &\equiv D_\tau(\mathbf{x}_{i,j}) \, , \end{aligned} \tag{B.18}$$

and,

$$\begin{aligned} \left(\frac{\partial^2 \mathbf{x}}{\partial \tau^2}\right)_{i,j} &\approx \frac{2}{\Delta \tau_j + \Delta \tau_{j+1}} \left\{ \frac{1}{\Delta \tau_{j+1}} \left(\mathbf{x}_{i,j+1} - \mathbf{x}_{i,j}\right) - \frac{1}{\Delta \tau_j} \left(\mathbf{x}_{i,j} - \mathbf{x}_{i,j-1}\right) \right\} \\ &\equiv D_\tau^2(\mathbf{x}_{i,j}) \, . \end{aligned} \tag{B.19}$$

It can be readily shown that these expressions reduce to the usual expressions when the time increments are equal.

B.4 Handling the Non-linear Terms

When trying to extend the Von Neumann scheme to include the non-linear terms, one is forced to evaluate their contributions at the unknown $j + 1$ time-level. In order to solve the finite difference equations for this time-level, the non-linear contributions must be linearized. The spatial non-linear term is handled using a standard Taylor expansion. The temporal non-linear term is linearized in a different manner, keeping in mind that it needs to accommodate the non-uniform mesh shown in Eqn. (B.18) and also fit the linearization scheme developed for the spatial term. The fully linearized system is then solved iteratively using a Newton-Raphson scheme [47].

B.4.1 Spatial non-linear term

For the spatial term, an expression must be derived which is compatible with Von Neumann's averaging method in Eqn. (B.9) for the second-order derivatives. To this end define

(using Hirsch's notation) the non-linear function H that will form the basis of an iterative scheme,

$$H = \left(\frac{\partial \mathbf{x}}{\partial \sigma}\right)^T \bar{\Gamma} \left(\frac{\partial \mathbf{x}}{\partial \sigma}\right), \tag{B.20}$$

and define a discretized form for H in terms of the average of the three time levels,

$$(H)_{i,j} \approx \lambda H_{i,j+1} + (1 - 2\lambda) H_{i,j} + \lambda H_{i,j-1}. \tag{B.21}$$

As before, the non-linear contribution at time level j is expressed implicitly in terms of the contribution at the unknown time level j+1. It can be seen, by substituting centered difference expressions for the spatial derivatives, that H yields a quadratic expression for each time level. The contributions at the j and $j-1$ level can be obtained directly, evaluating the Christoffel symbols at $\mathbf{x}_{i,j}$ and $\mathbf{x}_{i,j-1}$ along with the finite difference expressions. The $j+1$ level, however, cannot be handled directly by an implicit finite difference solver and must be linearized.

The most straightforward way to do this is through a Taylor expansion of $H^n_{i,j+1}$,

$$H^{n+1}_{i,j+1} \cong H^n_{i,j+1} + \tilde{J}\left(\mathbf{x}^n_{i,j+1}\right) \bullet \Delta \mathbf{x}^n_{i,j+1}, \tag{B.22}$$

where the upper index n is an iteration index, $\Delta \mathbf{x}^n_{i,j+1}$ represents the difference between the iterated solutions at the j+1 time-level,

$$\Delta \mathbf{x}^n_{i,j+1} = \mathbf{x}^{n+1}_{i,j+1} - \mathbf{x}^n_{i,j+1}, \tag{B.23}$$

and $\tilde{J}(\mathbf{x}^n_{i,j+1})$ is the Jacobian of the n-th iteration of $H^n_{i,j+1}$, written symbolically as,

$$\tilde{J}\left(\mathbf{x}^n_{i,j+1}\right) = \left(\frac{\partial H}{\partial \mathbf{x}}\right)^n_{i,j+1}. \tag{B.24}$$

After a sufficient number of iterations, H^{n+1} will represent the non-linear contribution at the $j+1$ time level.

These expressions are highly complex and need not be reproduced here; however, a partial result needs to be established before proceeding. The Jacobian is a matrix containing derivatives of the non-linear term with respect to the spacetime coordinates x^μ; as such, the spatial derivatives do not contribute to the Jacobian and can be factored out; only the Christoffel symbols are involved in the derivative. This operation, however, must be carried out with some care due to the discretization process (the details are provided in Hirsch [35]). To proceed, write the discrete spatial derivative using the shift operator E,

$$\left(\frac{\partial \mathbf{x}}{\partial \sigma}\right)_{i,j} = \frac{\left(E^1 - E^{-1}\right)}{2\Delta\sigma} \mathbf{x}_{i,j}, \tag{B.25}$$

where $E^{\pm 1}$ acts on $\mathbf{x}_{i,j}$, shifting it up or down by one spatial grid position. The shift operator can be used to rewrite the Jacobian,

$$\tilde{J}\left(\mathbf{x}_{i,j}\right) = \frac{\left(E^1 - E^{-1}\right)^2}{\left(2\Delta\sigma\right)^2} \mathbf{x}^T_{i,j} \frac{\partial \bar{\Gamma}}{\partial \mathbf{x}} \mathbf{x}_{i,j}, \tag{B.26}$$

where and $\frac{\partial \bar{\Gamma}}{\partial \mathbf{x}}$ represents the derivatives of the Christoffel symbols. These are analytic expressions that are given in Appendix D.

The full expression for the spatial non-linear terms is obtained by combining Eqns. (B.21) and (B.22), and expanding the shift operator in Eqn. (B.26), yielding

$$\begin{aligned} H_{i,j+1}^{n+1} \approx & \frac{\lambda}{4(\Delta\sigma)^2}\left[J(\mathbf{x}_{i+1,j}^n) \bullet \Delta\mathbf{x}_{i+1,j}^n - 2J(\mathbf{x}_{i,j}^n) \bullet \Delta\mathbf{x}_{i,j}^n\right. \\ & \left. + J(\mathbf{x}_{i-1,j}^n) \bullet \Delta\mathbf{x}_{i-1,j}^n\right] \\ & + \frac{\lambda}{4(\Delta\sigma)^2}\left[\mathbf{x}_{i+1,j+1}^n - \mathbf{x}_{i-1,j+1}^n\right]^T \bar{\Gamma}(\mathbf{x}_{i,j+1}^n)\left[\mathbf{x}_{i+1,j+1}^n - \mathbf{x}_{i-1,j+1}^n\right] \\ & + \frac{(1-2\lambda)}{4(\Delta\sigma)^2}\left[\mathbf{x}_{i+1,j} - \mathbf{x}_{i-1,j}\right]^T \bar{\Gamma}(\mathbf{x}_{i,j})\left[\mathbf{x}_{i+1,j} - \mathbf{x}_{i-1,j}\right] \\ & + \frac{\lambda}{4(\Delta\sigma)^2}\left[\mathbf{x}_{i+1,j-1} - \mathbf{x}_{i-1,j-1}\right]^T \bar{\Gamma}(\mathbf{x}_{i,j-1})\left[\mathbf{x}_{i+1,j-1} - \mathbf{x}_{i-1,j-1}\right]. \end{aligned} \tag{B.27}$$

B.4.2 Temporal non-linear term

For the temporal non-linear term

$$\left(\frac{\partial \mathbf{x}}{\partial \tau}\right)^T \bar{\Gamma}\left(\frac{\partial \mathbf{x}}{\partial \tau}\right), \tag{B.28}$$

it is again necessary to conform to the Von Neumann approach of Eqn. (B.8) and use a centered, second-order scheme. To begin, use Eqn. (B.18) to discretize Eqn. (B.28),

$$\left(\frac{\partial \mathbf{x}}{\partial \tau}\right)^T \bar{\Gamma}\left(\frac{\partial \mathbf{x}}{\partial \tau}\right) \approx \left[(D_\tau \mathbf{x}_{i,j})^T \bar{\Gamma}(\mathbf{x}_{i,j})\,(D_\tau \mathbf{x}_{i,j})\right]. \tag{B.29}$$

To make this discretization compatible with the iterative scheme developed for the spatial derivatives, make the substitution

$$\mathbf{x}_{i,j+1} = \mathbf{x}_{i,j+1}^{n+1} = \mathbf{x}_{i,j+1}^{n+1} - \mathbf{x}_{i,j+1}^n + \mathbf{x}_{i,j+1}^n = \Delta\mathbf{x}_{i,j+1}^n + \mathbf{x}_{i,j+1}^n \tag{B.30}$$

in Eqn. (B.29) and discard the term containing $\left(\Delta\mathbf{x}_{i,j+1}^n\right)^2$. This leads to

$$\begin{aligned} \left(\frac{\partial \mathbf{x}}{\partial \tau}\right)^T \bar{\Gamma}\left(\frac{\partial \mathbf{x}}{\partial \tau}\right) \approx & (D_\tau^n \mathbf{x}_{i,j})^T \bar{\Gamma}(\mathbf{x}_{i,j})\,(D_\tau^n \mathbf{x}_{i,j}) \\ & + \frac{2}{\Delta\tau_j + \Delta\tau_{j+1}} \frac{\Delta\tau_j}{\Delta\tau_{j+1}} (D_\tau^n \mathbf{x}_{i,j})^T \bar{\Gamma}(\mathbf{x}_{i,j+1}^n) \bullet \Delta\mathbf{x}_{i,j+1}^n, \end{aligned} \tag{B.31}$$

where D_τ now acts on the iterated value $\mathbf{x}_{i,j}^n$ as follows:

$$D_\tau^n \mathbf{x}_{i,j} = \frac{1}{\Delta\tau_j + \Delta\tau_{j+1}}\left\{\frac{\Delta\tau_j}{\Delta\tau_{j+1}}\left(\mathbf{x}_{i,j+1}^n - \mathbf{x}_{i,j}\right) + \frac{\Delta\tau_{j+1}}{\Delta\tau_j}\left(\mathbf{x}_{i,j} - \mathbf{x}_{i,j-1}\right)\right\}. \tag{B.32}$$

With this final result, the various pieces of the discretized equations of motion can be assembled and an iterative solution for the unknown time level can be written down.

B.5 Discretized Equations of Motion

The various results obtained in the previous section appear daunting. However, the process of assembling the various pieces into a final set of equations will yield a simple expression that can be handled numerically with relative ease.

Before proceeding with the task of assembling all results, two more adjustments must be done to ensure that all finite difference expressions are compatible with the iterative scheme. It is necessary to adjust the discretization (B.14) of the second-order spatial derivative to correctly handle the Δ-notation introduced in Eqn. (B.22). The discretization is modified to read

$$\begin{aligned}\left(\frac{\partial^2 \mathbf{x}}{\partial \sigma^2}\right)_{i,j} \approx & \frac{\lambda}{(\Delta\sigma)^2}\left(\mathbf{x}^n_{i+1,j+1} - 2\mathbf{x}^n_{i,j+1} + \mathbf{x}^n_{i-1,j+1}\right) \\ & + \frac{\lambda}{(\Delta\sigma)^2}\left(\Delta\mathbf{x}^n_{i+1,j+1} - 2\Delta\mathbf{x}^n_{i,j+1} + \Delta\mathbf{x}^n_{i-1,j+1}\right) \\ & + \frac{(1-2\lambda)}{(\Delta\sigma)^2}\left(\mathbf{x}_{i+1,j} - 2\mathbf{x}_{i,j} + \mathbf{x}_{i-1,j}\right) \\ & + \frac{\lambda}{(\Delta\sigma)^2}\left(\mathbf{x}_{i+1,j-1} - 2\mathbf{x}_{i,j-1} + \mathbf{x}_{i-1,j-1}\right), \end{aligned} \tag{B.33}$$

and similarly for the temporal second-order derivative (B.19),

$$\begin{aligned}\left(\frac{\partial^2 \mathbf{x}}{\partial \tau^2}\right)_{i,j} \approx & \frac{2}{\Delta\tau_j + \Delta\tau_{j+1}}\left\{\frac{1}{\Delta\tau_{j+1}}\left(\mathbf{x}^n_{i,j+1} - \mathbf{x}_{i,j}\right) - \frac{1}{\Delta\tau_j}\left(\mathbf{x}_{i,j} - \mathbf{x}_{i,j-1}\right)\right\} \\ & + \frac{2}{\Delta\tau_j + \Delta\tau_{j+1}}\left\{\frac{1}{\Delta\tau_{j+1}}\left(\Delta\mathbf{x}^n_{i,j+1}\right)\right\}. \end{aligned} \tag{B.34}$$

Combining results (B.33), (B.34), (B.27), and (B.31), and isolating the terms involving $\Delta\mathbf{x}^n_{i+1,j+1}$, $\Delta\mathbf{x}^n_{i,j+1}$, and $\Delta\mathbf{x}^n_{i-1,j+1}$ on the right hand side, the system of equations reduces to an equation for the components of a block-tridiagonal system of the form

$$A^n_{i-1,j+1} \bullet \Delta\mathbf{x}^n_{i-1,j+1} + B^n_{i,j+1} \bullet \Delta\mathbf{x}^n_{i,j+1} + C^n_{i+1,j+1} \bullet \Delta\mathbf{x}^n_{i+1,j+1} = d^n_{i,j+1}, \tag{B.35}$$

where $A^n_{i-1,j+1}$, $B^n_{i,j+1}$, and $C^n_{i+1,j+1}$ are 4×4 matrices and $d^n_{i,j+1}$ is a 4-vector.

The block-tridiagonal system expresses an implicit relationship between the iterated solution at all points on the spatial grid; this can best be seen by expanding the above expression for all grid points i=1,...,N:

$$\begin{aligned} B^n_{1,j+1}\Delta\mathbf{x}^n_{1,j+1} + C^n_{2,j+1}\Delta\mathbf{x}^n_{2,j+1} &= d^n_{1,j+1} \\ A^n_{1,j+1}\Delta\mathbf{x}^n_{1,j+1} + B^n_{2,j+1}\Delta\mathbf{x}^n_{2,j+1} + C^n_{3,j+1}\Delta\mathbf{x}^n_{3,j+1} &= d^n_{2,j+1} \\ \vdots \qquad\qquad \vdots & \qquad \vdots \\ A^n_{N-2,j+1}\Delta\mathbf{x}^n_{N-2,j+1} + B^n_{N-1,j+1}\Delta\mathbf{x}^n_{N-1,j+1} + C^n_{N,j+1}\Delta\mathbf{x}^n_{N,j+1} &= d^n_{N-1,j+1} \\ A^n_{N-1,j+1}\Delta\mathbf{x}^n_{N-1,j+1} + B^n_{N,j+1}\Delta\mathbf{x}^n_{N,j+1} &= d^n_{N,j+1}, \end{aligned} \tag{B.36}$$

or, as a matrix-vector product (suppressing the time step index),

$$\begin{pmatrix} B_1^n & C_2^n & & \cdots & & & \\ A_1^n & B_2^n & C_3^n & \cdots & & & \\ & \ddots & \ddots & \ddots & & & \\ & & \cdots & A_{N-2}^n & B_{N-1}^n & C_N^n \\ & & \cdots & & A_{N-1}^n & B_N^n \end{pmatrix} \begin{pmatrix} \Delta \mathbf{x}_1^n \\ \Delta \mathbf{x}_2^n \\ \vdots \\ \Delta \mathbf{x}_{N-1}^n \\ \Delta \mathbf{x}_N^n \end{pmatrix} = \begin{pmatrix} d_1^n \\ d_2^n \\ \vdots \\ d_{N-1}^n \\ d_N^n \end{pmatrix} . \tag{B.37}$$

This further reduces to the matrix expression

$$T^n \bullet \Delta \vec{\mathbf{x}}^n = \vec{d}^n , \tag{B.38}$$

where T in an $N \times N$ matrix whose elements are 4×4 matrices, and $\vec{\mathbf{x}}^n$ and $\vec{d}^n$ are vectors of length N whose elements are 4-vectors.

Using the definitions

$$\kappa := \left(\frac{\Delta \tau_{j+1} + \Delta \tau_j}{\Delta \sigma} \right) \quad , \quad \eta := \frac{\Delta \tau_j}{\Delta \tau_{j+1}} ,$$

the components of the block tridiagonal system are

$$\begin{aligned}
A_{i-1,j+1}^n &= -\lambda \kappa^2 \left(\mathbf{I} + \frac{1}{4} J \left(\mathbf{x}_{i-1,j+1}^n \right) \right) \\
B_{i,j+1}^n &= 2 \lambda \kappa^2 \left(\mathbf{I} + \frac{1}{4} J \left(\mathbf{x}_{i,j+1}^n \right) \right) + 2 \left(1 + \eta \right) \mathbf{I} \\
&+ 2 \left[\eta^2 \left(\mathbf{x}_{i,j+1}^n - \mathbf{x}_{i,j} \right) + \left(\mathbf{x}_{i,j} - \mathbf{x}_{i,j-1} \right) \right]^T \bar{\Gamma} (\mathbf{x}_{i,j}) \\
C_{i+1,j+1}^n &= -\lambda \kappa^2 \left(\mathbf{I} + \frac{1}{4} J \left(\mathbf{x}_{i+1,j+1}^n \right) \right) \\
d_{i,j+1}^n &= -2 \left\{ \left(1 + \eta \right) \left(\mathbf{x}_{i,j+1}^n - \mathbf{x}_{i,j} \right) - \left(1 + \eta^{-1} \right) \left(\mathbf{x}_{i,j} - \mathbf{x}_{i,j-1} \right) \right\} \\
&- \left[\eta \left(\mathbf{x}_{i,j+1}^n - \mathbf{x}_{i,j} \right) + \eta^{-1} \left(\mathbf{x}_{i,j} - \mathbf{x}_{i,j-1} \right) \right]^T \bar{\Gamma} (\mathbf{x}_{i,j}) \bullet \\
&\quad \left[\eta \left(\mathbf{x}_{i,j+1}^n - \mathbf{x}_{i,j} \right) + \eta^{-1} \left(\mathbf{x}_{i,j} - \mathbf{x}_{i,j-1} \right) \right] \\
&+ \lambda \kappa^2 \left(\mathbf{x}_{i+1,j+1}^n - 2 \mathbf{x}_{i,j+1}^n + \mathbf{x}_{i-1,j+1}^n \right) \\
&+ \left(1 - 2 \lambda \right) \kappa^2 \left(\mathbf{x}_{i+1,j} - 2 \mathbf{x}_{i,j} + \mathbf{x}_{i-1,j} \right) \\
&+ \lambda \kappa^2 \left(\mathbf{x}_{i+1,j-1} - 2 \mathbf{x}_{i,j-1} + \mathbf{x}_{i-1,j-1} \right) \\
&+ \lambda \kappa^2 \left(\mathbf{x}_{i+1,j+1}^n - \mathbf{x}_{i-1,j+1}^n \right)^T \bar{\Gamma} \left(\mathbf{x}_{i,j+1}^n \right) \left(\mathbf{x}_{i+1,j+1}^n - \mathbf{x}_{i-1,j+1}^n \right) \\
&+ \left(1 - 2 \lambda \right) \kappa^2 \left(\mathbf{x}_{i+1,j} - \mathbf{x}_{i-1,j} \right)^T \bar{\Gamma} \left(\mathbf{x}_{i,j} \right) \left(\mathbf{x}_{i+1,j} - \mathbf{x}_{i-1,j} \right) \\
&+ \lambda \kappa^2 \left(\mathbf{x}_{i+1,j-1} - \mathbf{x}_{i-1,j-1} \right)^T \bar{\Gamma} \left(\mathbf{x}_{i,j-1} \right) \left(\mathbf{x}_{i+1,j-1} - \mathbf{x}_{i-1,j-1} \right) ,
\end{aligned} \tag{B.39}$$

where $\mathbf{I}$ is the 4×4 identity matrix.

B.5.1 Boundary Conditions

For numerical scheme A, where the string is prescribed by the perturbation solution, the boundary conditions are

$$\begin{aligned} B^n_{1,j+1} &= \mathbf{I} \\ C^n_{2,j+1} &= 0 \\ d^n_{1,j+1} &= \mathcal{X}^n_{1,j+1} - \mathcal{X}^{n-1}_{1,j+1} \\ A^n_{N-1,j+1} &= 0 \\ B^n_{N,j+1} &= \mathbf{I} \\ d^n_{N,j+1} &= \mathcal{X}^n_{N,j+1} - \mathcal{X}^{n-1}_{N,j+1}, \end{aligned} \tag{B.40}$$

where $\mathcal{X}$ are the analytic expressions for the perturbative solutions evaluated at the discrete coordinates given by the edges of the grid, σ_1 and σ_N, and the iterated time coordinates τ^{n-1}_{j+1} and τ^n_{j+1}.

For numerical scheme B, where the string is terminated by massive particles, the boundary conditions are derived in the same manner as the temporal terms discussed above; they have the form

$$\begin{aligned} B^n_{1,j+1} &= 2\,(1+\eta)\,\mathbf{I} \\ &+ 2\left[\eta^2\,\left(\mathbf{x}^n_{1,j+1} - \mathbf{x}_{1,j}\right) + \left(\mathbf{x}_{1,j} - \mathbf{x}_{1,j-1}\right)\right]^T \bar{\Gamma}(\mathbf{x}_{1,j}) \\ C^n_{2,j+1} &= 0 \\ d^n_{1,j+1} &= -2\left\{(1+\eta)\,\left(\mathbf{x}^n_{1,j+1} - \mathbf{x}_{1,j}\right) - \left(1+\eta^{-1}\right)\,\left(\mathbf{x}_{1,j} - \mathbf{x}_{1,j-1}\right)\right\} \\ &- \left[\eta\,\left(\mathbf{x}^n_{1,j+1} - \mathbf{x}_{1,j}\right) + \eta^{-1}\,\left(\mathbf{x}_{1,j} - \mathbf{x}_{1,j-1}\right)\right]^T \bar{\Gamma}(\mathbf{x}_{1,j}) \bullet \\ &\quad \left[\eta\,\left(\mathbf{x}^n_{1,j+1} - \mathbf{x}_{1,j}\right) + \eta^{-1}\,\left(\mathbf{x}_{1,j} - \mathbf{x}_{1,j-1}\right)\right] \\ A^n_{N-1,j+1} &= 0 \\ B^n_{N,j+1} &= 2\,(1+\eta)\,\mathbf{I} \\ &+ 2\left[\eta^2\,\left(\mathbf{x}^n_{N,j+1} - \mathbf{x}_{N,j}\right) + \left(\mathbf{x}_{N,j} - \mathbf{x}_{N,j-1}\right)\right]^T \bar{\Gamma}(\mathbf{x}_{N,j}) \\ d^n_{N,j+1} &= -2\left\{(1+\eta)\,\left(\mathbf{x}^n_{N,j+1} - \mathbf{x}_{N,j}\right) - \left(1+\eta^{-1}\right)\,\left(\mathbf{x}_{N,j} - \mathbf{x}_{N,j-1}\right)\right\} \\ &- \left[\eta\,\left(\mathbf{x}^n_{N,j+1} - \mathbf{x}_{N,j}\right) + \eta^{-1}\,\left(\mathbf{x}_{N,j} - \mathbf{x}_{N,j-1}\right)\right]^T \bar{\Gamma}(\mathbf{x}_{N,j}) \bullet \\ &\quad \left[\eta\,\left(\mathbf{x}^n_{N,j+1} - \mathbf{x}_{N,j}\right) + \eta^{-1}\,\left(\mathbf{x}_{N,j} - \mathbf{x}_{N,j-1}\right)\right]. \end{aligned} \tag{B.41}$$

B.6 Discretization of the Constraints

The constraint equations, derived in Chapter 3, have the form

$$\begin{aligned} g_{\mu\nu}\left[\frac{\partial \mathcal{X}^\mu}{\partial \tau}\frac{\partial \mathcal{X}^\nu}{\partial \tau} + \frac{\partial \mathcal{X}^\mu}{\partial \sigma}\frac{\partial \mathcal{X}^\nu}{\partial \sigma}\right] &= 0, \\ g_{\mu\nu}\left[\frac{\partial \mathcal{X}^\mu}{\partial \tau}\frac{\partial \mathcal{X}^\nu}{\partial \sigma}\right] &= 0. \end{aligned} \tag{B.42}$$

They are used as checks on the solutions to the equations of motion.

With the notation introduced earlier, the constraints can be written in vector-matrix form,

$$\left(\frac{\partial \mathbf{x}}{\partial \tau}\right)^T \bar{g} \left(\frac{\partial \mathbf{x}}{\partial \tau}\right) + \left(\frac{\partial \mathbf{x}}{\partial \sigma}\right)^T \bar{g} \left(\frac{\partial \mathbf{x}}{\partial \sigma}\right) = 0, \tag{B.43}$$

and

$$\left(\frac{\partial \mathbf{x}}{\partial \tau}\right)^T \bar{g} \left(\frac{\partial \mathbf{x}}{\partial \sigma}\right) = 0. \tag{B.44}$$

where $\bar{g}$ denotes the matrix form of the metric $g_{\mu\nu}$ evaluated.

The constraint calculations should yield a zero result when applied to the solution produced by the iterative scheme described above, and are computed using the solutions at three adjacent time steps, $\mathbf{x}_{i,j-1}$, $\mathbf{x}_{i,j}$, and $\mathbf{x}_{i,j+1}$. The discretization of these equations is straightforward, using the first-ordered centered difference expressions (B.13) and (B.18). The first constraint reads

$$-(D_\tau \mathbf{x}_{i,j})^T \bar{g}(\mathbf{x}_{i,j}) (D_\tau \mathbf{x}_{i,j}) + (D_\sigma \mathbf{x}_{i,j})^T \bar{g}(\mathbf{x}_{i,j}) (D_\sigma \mathbf{x}_{i,j}) = 0. \tag{B.45}$$

The second constraint reads

$$\left(\frac{1}{2\Delta\sigma}\right) (D_\tau \mathbf{x}_{i,j})^T \bar{g}(\mathbf{x}_{i,j}) (\mathbf{x}_{i+1,j} - \mathbf{x}_{i-1,j}) = 0, \tag{B.46}$$

These expressions can be expanded in a straightforward manner to yield the final scalar-valued expressions that are used in the numerical solvers, and are not reproduced here.

Appendix C

Coding Issues

The discretized equations of motion and the corresponding numerical IBVP shown in Appendix B were coded in Fortran77, with some low-level routines coded in C. Depending on the computational complexity of the spacetime (i.e. the number and complexity of the non-zero Christoffel symbols) and the resolution requirements of the particular study, the numerical solver can be computationally intensive. In order to accommodate the full range of needs, a modular design that admitted easy modifications for different spacetimes, boundary conditions, and resolution, was adopted. The choices in coding techniques aimed to strike a balance between adaptability and efficiency, and a number of optimizations were carried out to achieve good performance on a Silicon Graphics Power Challenge computer.

The final, working version of the solver supports straight-string initial configurations and two boundary conditions (particle and perturbation solution) for Minkowski spacetime and Schwarzschild and Kerr black holes. For Schwarzschild black holes, both Schwarzschild and Eddington-Finkelstein Ingoing coordinates are supported; for Kerr black holes, Boyer-Lindquist and Kerr coordinates. These coordinate systems allow both scattering and trapping studies to be carried out, with Eddington-Finkelstein and Kerr coordinates used in the latter case. Minkowski spacetime is used to carry out accuracy and longevity tests since the numerical solution is readily compared to the known analytic solution.

This appendix presents code fragments of the more important routines of the numerical solver, and describes numerical tests that were carried out to validate its operation. Since the fully optimized solver represents approximately 10,000 Fortran77 statements, with another 1,000 or so lines of C, only a cursory look will be taken.

C.1 Overview of the Von Neumann Solver

The numerical evolution of a cosmic string in the spacetime of a black hole is governed by a set of parameters:

- **string:** length, initial position (impact parameter, distance from black hole) and velocity,

- **black hole:** mass and angular momentum,
- **numerical:** maximum number of time steps, frequency of output, constraint checks, checkpoints, type and resolution of output (ASCII, binary, low- or high-resolution).

Tasks such as output of the solution and constraint calculations are triggered on a periodic basis. The code also periodically saves a copy of its internal state to allow restarts (two consecutive time steps along with some counter values are sufficient for this purpose). Restarts are useful to recover from system failures, and are also useful checkpoints from which higher-resolution runs can be launched. This feature was used extensively to visualize the final plunge of strings into black holes. These parameters are contained in an input file that is read by the solver at the beginning of a run.

The code is built around a main routine that controls the time-stepping behaviour by which the solution is advanced. The sequence of events that take place are as follows:

VN Solver:		
	read parameter file	
	validate parameters	
	set internal variables	
	initialize two time steps	(from analytic solution or restart file)
Evolve:	compute next **time step**	
	success?	no - **shutdown**
	constraint check?	yes - compute constraint, report statistics
	output?	yes - write solution to file
	checkpoint?	yes - write restart file
	maximum time step?	yes - **shutdown**
		no - **evolve**
Shutdown:	close files	
	exit	

Each time step is computed according to the iterative formula established in Appendix B, and proceeds as follows:

Time step:		
	clear working arrays	
Iterate:	initialize Jacobian arrays	
	initialize tridiagonal arrays	
	check stability condition	
	solve tridiagonal system	
	update solution	(from d vector of tridiagonal system)
	solution converged?	no - **iterate**
		yes - flag success and **exit**
	too many steps?	yes - reduce step size, repeat **time step**
	step size too small?	yes - flag error and **exit**
Exit:	return to main program	

The initialization of the tridiagonal matrices is discussed in the next section. The solution of the block tridiagonal system is a standard numerical procedure that is accomplished using the Thomas algorithm (which carries out Gaussian elimination without pivoting). Since this final form of the finite difference expression is an iterative one, the final solution for time level j+1 is obtained when the above system yields a zero d-vector. Failure to converge triggers a time-step reduction mechanism where the time interval $\Delta\tau_{j+1}$ is reduced and the solution attempted once more. If the reduction is repeated too many times, the solution is stopped.

C.2 Initializing Block Tridiagonal Matrices

As discussed in Appendix B, the discretized equations of motion have the form of a block tridiagonal system,

$$T^n \Delta\vec{x}^n = \vec{d}^n \,, \tag{C.1}$$

that is solved iteratively (n is an iteration index, and should not be confused with the time step index j). The solution is evolved forward in time to the $j+1$ time step by carrying out the operation

$$\vec{x}^{n+1} = \vec{x}^n + (T^n)^{-1}\vec{d}^n \tag{C.2}$$

until the solution converges, i.e. $\Delta x^n / x^n \approx 0$. In practical terms, this means that

$$\frac{\Delta x^n_{\bullet,j+1}}{x^n_{\bullet,j+1}} \leq 10^{-6} \tag{C.3}$$

holds for all grid points at the new time level $(j+1)$. This value of the convergence threshold represents a compromise between speed and accuracy (it assumes that results are stored as double-precision values).

The constituents of the block tridiagonal matrix T^n are given in Appendix B, where Eqn. (B.39) applies to all grid points on the interior of the string ($1 < i < N$) and Eqns. (B.40) or (B.41) apply to the boundaries ($i = 1, N$).

The components of the A, B, and C blocks (4×4 matrices) in T are built up from the 4D identity matrix, I, the Jacobians $\tilde{J}(x_{\bullet,j+1})$, and, for block B, an expression of the form $X^T\bar{\Gamma}$.

The elements of the Jacobian matrices (indexed by μ, ν) are computed from

$$\tilde{J}\left(\mathbf{x}_{i,j}^n\right) = \frac{1}{(2\,\Delta\,\sigma)^2}\left(\mathbf{x}_{i+1,j}^n - \mathbf{x}_{i-1,j}^n\right)^T \frac{\partial \bar{\Gamma}(\mathbf{x}_{i,j}^n)}{\partial \mathbf{x}}\left(\mathbf{x}_{i+1,j}^n - \mathbf{x}_{i-1,j}^n\right), \tag{C.4}$$

which can be written as matrix elements

$$\left[\tilde{J}\left(\mathbf{x}_{i,j}^n\right)\right]_{\mu\nu} = \frac{1}{(2\,\Delta\,\sigma)^2}\frac{\partial \Gamma_{\rho\eta}^{\mu}(\mathbf{x}_{i,j}^n)}{\partial x^{\nu}}\left(x_{i+1,j}^{\rho\,n} - x_{i-1,j}^{\rho\,n}\right)\left(x_{i+1,j}^{\eta\,n} - x_{i-1,j}^{\eta\,n}\right), \tag{C.5}$$

where $\partial\,\Gamma_{\rho\eta}^{\mu}(\mathbf{x}_{i,j}^n)/\partial\,x^{\nu}$ represents the derivatives of the Christoffel symbol at the spacetime coordinate $\mathbf{x}_{i,j}^n$, and summation is implied over indices ρ and η. The order of the matrix indices is important: the Christoffel index μ is a row index, and the coordinate index ν is a row index for the Jacobian matrix. The Jacobians represent the derivatives of the solution at the heart of the Newton-Raphson scheme that linearizes the spatial term in the equations of motion.

C.2.1 Jacobian matrices

The initialization of the Jacobian matrices is carried out at the start of every iteration. As shown in Eqn. (B.39), three Jacobian matrices must be computed at each grid point, one associated with each of the A, B and C matrices for the grid point. The Jacobians are stored in three separate arrays, dimensioned as $JACA(4,4,N)$, $JACB(4,4,N)$, and $JACC(4,4,N)$, associated with the A, B, and C matrices. Each matrix is initialized by a routine represented by the code fragment

```
DO I = 1,N
   DO COL = 1,4
      DO ROW = 1,4
         DO RHO = 1,4
            DO ETA = 1,4
               SUM=SUM+DCHR(RHO,ETA,ROW,COL,X(1,I))*
                      (X(ETA,I+1)-X(ETA,I-1))
            ENDDO
            JACB(ROW,COL,I) = JACB(ROW,COL,I) +
                              SUM*(X(RHO,I+1)-X(RHO,I-1))
         ENDDO
      ENDDO
   ENDDO
ENDDO
```

where the innermost DO-loops (indexed by RHO and ETA) implement the double sum shown in Eqn. (C.5). The array X represents the current iteration of the solution at the $J+1$ time step.

The B matrices receive a contribution from the linearization of the temporal non-linear term

$$B_{\tau\, linear} = \left[\eta^2 \left(\mathbf{x}^n_{i,j+1} - \mathbf{x}_{i,j}\right) + \left(\mathbf{x}_{i,j} - \mathbf{x}_{i,j-1}\right)\right]^T \bar{\Gamma}(\mathbf{x}_{i,j}), \tag{C.6}$$

which requires operations of the form $X^T\bar{\Gamma}$. That these equations evaluate to matrix elements can be seen from the expression

$$[B_{\tau\, linear}]_{\mu\nu} = \Gamma^{\mu}_{\rho\nu}(\mathbf{x}_{i,j})\left[\eta^2 \left(x^{(n)\rho}_{i,j+1} - x_{i,1}{}^{\rho}\right) + \left(x_{i,j}{}^{\rho} - x_{i,j-1}{}^{\rho}\right)\right], \tag{C.7}$$

where summation is implied on the ρ index.

The initialization of the A, B, and C arrays is carried out as follows. As with the Jacobians, the constituents of the tridiagonal system are stored in matrices dimensioned $A(4,4,N)$, $B(4,4,N)$, and $C(4,4,N)$.

At each grid point on the string interior (DO I=2,N-1), the following operations take place (shown here for B matrix only). First, the Jacobian matrices are included,

```
DO COL = 1,BLOCK
   DO ROW = 1,BLOCK
      B(ROW,COL,I) = -CONS1*JACB(ROW,COL,I)
   END DO
END DO
```

then the identity matrix is summed in,

```
DO COL = 1,BLOCK
   B(COL,COL,I) = B(COL,COL,I)+
                  2.D0*(CONS2+(DTAU1+DTAU2)/DTAU2)
END DO
```

followed by the temporal contribution (C.7) to the B matrix,

```
DO ROW = 1,BLOCK
   DO COL = 1,BLOCK
      DO INDX=1,BLOCK
         SUM = SUM +
             ((DTAU1/DTAU2)*(X(INDX,I,UTOLD)-X(INDX,I,UT))+
              (DTAU2/DTAU1)*(X(INDX,I,UT)-X(INDX,I,UTM)))*
               CHR(ROW,COL,INDX,U(1,I,UT))
      END DO
      B(ROW,COL,I) = B(ROW,COL,I) + 2.D0*SUM*DTAU1/DTAU2
   END DO
END DO
```

The constants DTAU1 and DTAU2 represent the step sizes $\Delta\tau_j$ and $\Delta\tau_{j+1}$, respectively. The constant CONS1 represents the constant $\lambda\kappa^2/4$ and CONS2 represents $\lambda\kappa^2$, where κ and λ are defined in Appendix B.

Boundary conditions are treated in a similar manner.

The components of the $\vec{d}$-vector all evaluate to 4-vectors. Most of the elements of $d^n_{\bullet,\bullet}$ are simple differences of solutions $x_{\bullet,\bullet}$ at various grid points, along with vector-matrix products of the form $x^T\bar{\Gamma}\,x$. As shown above, expressions $x^T\bar{\Gamma}$ evaluate to 4×4 matrices, so the vector matrix products evaluate to 4-vectors.

The matrix for the $\vec{d}$-vector is dimensioned D(4,N) and individual 4-vector elements in D are initialized with expressions of the form

```
   DO ROW = 1,BLOCK
      D2SP(ROW) = KAPPA*LAMBDA*(U(ROW,I-1,UTOLD)-
     &                2.DO*U(ROW,I,UTOLD)+U(ROW,I+1,UTOLD))
   END DO
```

for difference expressions, and

```
DO ROW = 1,BLOCK
   TEMP1 = ZERO
   DO COL = 1,BLOCK
      TEMP2 =(TCONS3*(U(COL,I,UTOLD)-U(COL,I,UT))+
     &           (U(COL,I,UT)-U(COL,I,UTM))/TCONS3)
      TEMP1 = TEMP1+TEMP2*TEMP2*CHR(ROW,COL,COL,U(1,I,UT))
       END DO
       DGDT(ROW) = -TEMP1
END DO

DO ROW = 1,BLOCK
   TEMP1 = ZERO
   DO COL = 2,BLOCK
      TEMP2 =(TCONS3*(U(COL,I,UTOLD)-U(COL,I,UT))+
     &           (U(COL,I,UT)-U(COL,I,UTM))/TCONS3)
        DO INDX=1,COL-1
         TEMP1 = TEMP1+TEMP2*
     &               (TCONS3*(U(INDX,I,UTOLD)-U(INDX,I,UT))+
     &               (U(INDX,I,UT)-U(INDX,I,UTM))/TCONS3)*
     &                CHR(ROW,COL,INDX,U(1,I,UT))
          END DO
       END DO
       DGDT(ROW) = DGDT(ROW) - 2.DO*TEMP1
END DO
```

for vector-matrix products (here shown in a form that improves handling the off-diagonal Christoffel symbols). The constant KAPPA represents the constant κ^2 defined in Ap-

pendix B and TCONS3 is the ratio $\Delta\tau_j/\Delta\tau_{j+1}$. The arrays D2SP(ROW) and DGDT(ROW) are temporary arrays that are subsequently stored into the main array for the D vector along with other similar contributions.

C.3 Christoffel Symbols and their Derivatives

The above code fragments include references to Fortran functions CHR and DCHR. These functions return the values of

$$CHR(I,J,K,U) \rightarrow \Gamma^{\mu}_{\rho\eta}(x^{\lambda}) \equiv \Gamma^{k}_{ij}(x^{\lambda}) \tag{C.8}$$

and

$$DCHR(I,J,K,L,U) \rightarrow \frac{\partial\Gamma^{\mu}_{\rho\eta}(x^{\lambda})}{\partial x^{\sigma}} \equiv \Gamma^{k}_{ij,l}(x^{\lambda}) \tag{C.9}$$

evaluated at the spacetime point x^{λ}.

These functions are built up from switching logic of the form

```
IF(I.EQ.1) THEN
  IF((K.EQ.1).AND.(J.EQ.1)) THEN
     CHR = MASS/(R*R)
  ELSEIF((K.EQ.3).AND.(J.EQ.3)) THEN
     CHR = -R
  ELSEIF((K.EQ.4).AND.(J.EQ.4)) THEN
     CHR = -R*SIN(TH)*SIN(TH)
  ELSE
     CHR = 0.DO
  ENDIF
ELSEIF(I.EQ.2) THEN
  ...
ENDIF
```

shown here for a portion of FUNCTION REAL*8 CHR() in the case of Schwarzschild coordinates. The indices passed as arguments in the function call result in the selection and evaluation of the appropriate Christoffel symbol or derivative (the Christoffel symbols are listed in Appendix D).

C.4 Optimizations and Parallelization

In practical terms, due to spacetime symmetries, many elements of the A, B, C and D block matrices are identically zero, or identical to other components (for instance, in Schwarzschild spacetime there are only 9 non-vanishing Christoffel symbols; see Appendix D). Similarly, many elements of the Jacobians are identically zero, for symmetry reasons and also because the Christoffel symbols have no functional dependence on certain coordinates (both

Schwarzschild and Kerr black holes are stationary, so their Christoffel symbols have no functional dependence on the t-coordinate). So, a straightforward looping construct over all possible indices in the Christoffel symbols is, in general, quite inefficient.

Instead, the DO-statements in the initialization of the A, B, C, and D matrices are removed and the non-zero indices are explicitly listed and summed over by hard-coding specific index values (ROW and COL) into the code fragments shown above (this is a form of loop unrolling). Preserving a full looping structure generates compact code, but invokes a large number of Christoffel symbols that, in the end, contribute nothing to the tridiagonal system. This optimization lengthens the code considerably, but results in significant performance improvements. Further improvements could be obtained by in-lining the specific expressions for the Christoffel symbols, hence doing away with the functions CHR and DCHR, but this would make the resulting code virtually unreadable; instead, compiler-driven optimizations were used to further streamline the code.

There is inherent parallelism at many levels in the Von Neumann solver. The initialization of the elements of JACA, JACB, and JACC are all independent and can be done concurrently, as can the initialization of the A, B, C, and D matrices. However, the J matrices must be computed before the other matrices can be initialized, so the two initializations must be done in strict order. The tridiagonal system also has some inherent parallelism, and can be solved in parallel using a divide-and-conquer method described by Bondeli [11] for scalar tridiagonal systems and extended by the author for block-tridiagonal systems [19].

The matrix initialization routines are the most numerically intensive portions of the code, especially for the more complicated Kerr coordinate system that allows following a string into the interior of a rotating black hole. These routines are parallelized in a straightforward manner, by placing a directive at the outermost DO-loop, here shown for the Silicon Graphics parallel computers,

```
C$ DOACROSS
      DO I = 2,N-1
         ... body of routine
      ENDDO
```

Each of P processors handles a sub-range of the DO index I, representing points on the spatial grid. This means that parallelism is expressed within each iteration of a time step, and nowhere else. No significant gains are realized by parallelizing the tridiagonal solver; this parallelization is only effective for very large linear systems (i.e. grids on the order of 10^5 points) which have not, to date, been required.

The code was parallelized and runs on a number of platforms, but most production work is carried out on an 8-processor SGI Power Challenge. Typical execution speeds for geodesic boundary conditions are roughly 4000 time steps per hour for non-rotating black holes on 4 processors (grid of 8000 points), and 2000 time steps per hour on 8 processors for rotating black holes (grid of 8000 points). The optimum number of processors for each version of the code is determined from speed-up curves, such as the one shown in Fig. C.1.

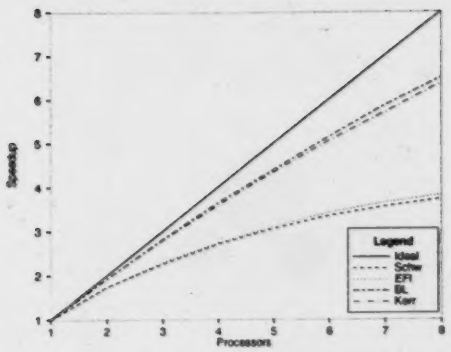

Figure C.1: Scalability graph for SGI Power Challenge.

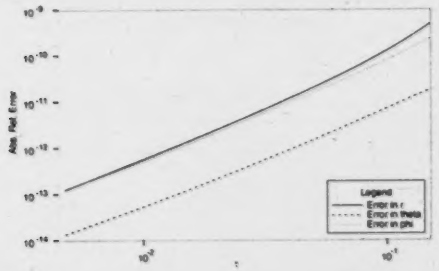

Figure C.2: Accuracy of Solver.

C.5 Testing Accuracy and Longevity

The analytic expression that is used to initiate solutions in black hole spacetimes can also be used to test the solver. It was mentioned earlier that the Christoffel symbols in empty spacetime under Cartesian coordinates are identically zero; however, this is not the case in spherical polar coordinates where there are 6 distinct, non-zero Christoffel symbols. This fact was used to test the non-linear portions of the solver by producing a test version that encodes empty-space spherical polar coordinates and reports the difference between numerical and analytic solutions. The results are shown in Fig. C.2, where the absolute relative error $(|(\mathbf{x}_{num} - \mathbf{x}_{analyt})/\mathbf{x}_{analyt}|)$ averaged over the spatial grid is plotted as a function of string proper time, τ. The graph covers roughly 10,000 time steps, and the slope confirms that the method is second-order accurate in the time step size $\Delta\tau$. Additional tests were carried out for uniformly accelerated strings based on the solutions in Ref. [28] that produced similar accuracy curves. Other means were used to validate the code, and these are described in Chapter 4.

Although formal tests were not carried out in the strongly non-linear regime, the convergence and consitency of the numerical method was verified implicitly in the course of

studying near-critical scattering (see Chapter 5), where low-resolution runs were supplemented by high-resolution runs with the same physical parameters (initial velocity and impact parameter). In each case where high- and low-resolution data sets were combined, the agreement between the data sets was complete at the level of accuracy required to generate the graphs shown in Chapter 5, with the high-resolution data set filling in the gaps in the low-resolution data set. This is a strong indication that the numerical solver is well behaved under extremely non-linear conditions at the chosen grid sizes.

Appendix D

Metrics and Christoffel Symbols

The following are lists of the various metrics and Christoffel symbols. These expressions, along with the derivatives of the Christoffel symbols, were generated and verified using Mathematica and the package TTC [14] and coded directly as FORTRAN-77 functions for use in the Von Neumann solver. In this form, they are invoked in the set-up of the block-tridiagonal matrices and in the computation of the components of the induced metric for the constraint calculations.

The spacetime metric is written as

$$ds^2 = g_{\mu\nu} dx^\mu dx^\nu , \tag{D.1}$$

and the Christoffel symbols are derivatives of the metric components, $g_{\mu\nu}$,

$$\Gamma^\nu_{\rho\sigma} = \frac{1}{2} g^{\nu\mu} \left(g_{\rho\mu,\sigma} - g_{\sigma\rho,\mu} + g_{\mu\sigma,\rho} \right) , \tag{D.2}$$

which are symmetric in the lower indices,

$$\Gamma^\nu_{\rho\sigma} = \Gamma^\nu_{\sigma\rho} . \tag{D.3}$$

D.1 Minkowski Metric

The metric of flat spacetime is used in finding solutions to the equations of motion of the cosmic string that are used as the basis for initial data in numerical calculations and as background solutions to perturbation calculations.

D.1.1 Cartesian Coordinates

Coordinates: $(X^0, X^1, X^2, X^3) \equiv (T, X, Y, Z)$

Metric components:

$$-g_{00} = g_{11} = g_{22} = g_{33} = 1 \tag{D.4}$$

Christoffel Symbols: $\Gamma^{\nu}_{\rho\sigma} \equiv 0$

D.1.2 Spherical-Polar Coordinates

Coordinates: $(X^0, X^1, X^2, X^3) \equiv (t, r, \theta, \phi)$

Metric components:

$$g_{00} = -1,\ g_{11} = 1,\ g_{22} = r^2,\ g_{33} = r^2 \sin^2\theta \tag{D.5}$$

Non-vanishing Christoffel Symbols:

$$\Gamma^1_{22} = -r,\ \Gamma^1_{33} = -r\sin^2\theta,\ \Gamma^2_{12} = \frac{1}{r},\ \Gamma^2_{33} = -\frac{\sin(2\theta)}{2},\ \Gamma^3_{13} = \frac{1}{r},\ \Gamma^3_{23} = \cot\theta \tag{D.6}$$

D.2 Schwarzschild Metric

The Schwarzschild metric describes static, spherically symmetric solutions to the Einstein equations of General Relativity. The Schwarzschild metric describes a black hole of mass M with an event horizon located at $r_g = 2M$ (also known as the gravitational radius). Schwarzschild coordinates are an extension of the spherical-polar coordinates of flat spacetime; the Christoffel symbols in this metric are discontinuous at the event horizon. The Eddington-Finkelstein Ingoing coordinate system fixes this coordinate singularity by transforming the time coordinate. The Isotropic coordinate system, which is an extension of the Cartesian coordinates of flat spacetime, is used as the basis of perturbative expansions. Due to the large number of non-zero Christoffel symbols (and hence many non-zero derivatives), this last coordinate system is numerically inefficient and is not used. Instead, numerical solutions are generated using, usually, the EFI coordinate system and related to perturbative results using the coordinate transformations of Appendix E.

D.2.1 Schwarzschild Coordinates

Coordinates: $(X^0, X^1, X^2, X^3) \equiv (t, r, \theta, \phi)$

Metric Components:

$$g_{00} = -\left(1 - \frac{2M}{r}\right),\ g_{11} = \left(1 - \frac{2M}{r}\right)^{-1},\ g_{22} = r^2,\ g_{33} = r^2\sin^2\theta \tag{D.7}$$

Non-vanishing Christoffel Symbols:

$$\Gamma^0_{01} = \frac{M}{r^2}\left(1 - \frac{2M}{r}\right)^{-1},\ \Gamma^1_{00} = \frac{M}{r^2}\left(1 - \frac{2M}{r}\right),\ \Gamma^1_{11} = -\frac{M}{r^2}\left(1 - \frac{2M}{r}\right)^{-1} \tag{D.8}$$

$$\Gamma^1_{22} = -r\left(1-\frac{2M}{r}\right), \Gamma^1_{33} = -r\left(1-\frac{2M}{r}\right)\sin^2\theta, \Gamma^2_{12} = \frac{1}{r}$$

$$\Gamma^2_{33} = -\frac{\sin(2\theta)}{2}, \Gamma^3_{13} = \frac{1}{r}, \Gamma^3_{23} = \cot\theta$$

D.2.2 Eddington-Finkelstein Coordinates

Coordinates: $(X^0, X^1, X^2, X^3) \equiv (\tilde{V}, r, \theta, \phi)$, $\tilde{V} = t + r + 2M \ln\frac{r}{2M} - 1$

Metric components:

$$g_{00} = -\left(1-\frac{2M}{r}\right), g_{01} = 1, g_{22} = r^2, g_{33} = r^2\sin^2\theta \tag{D.9}$$

Non-vanishing Christoffel Symbols:

$$\Gamma^0_{00} = \frac{M}{r^2}, \Gamma^0_{22} = -r, \Gamma^0_{33} = -r\sin^2\theta \tag{D.10}$$

$$\Gamma^1_{00} = \frac{M}{r^2}\left(1-\frac{2M}{r}\right), \Gamma^1_{01} = -\frac{M}{r^2}, \Gamma^1_{22} = -r\left(1-\frac{2M}{r}\right)$$

$$\Gamma^1_{33} = -r\left(1-\frac{2M}{r}\right)\sin^2\theta, \Gamma^2_{12} = \frac{1}{r}, \Gamma^2_{33} = -\frac{\sin(2\theta)}{2}$$

$$\Gamma^3_{13} = \frac{1}{r}, \Gamma^3_{23} = \cot\theta$$

D.2.3 Isotropic Coordinates

Coordinates: $(X^0, X^1, X^2, X^3) \equiv (T, X, Y, Z)$

Metric components:

$$g_{00} = -\left(\frac{1-\frac{M}{2r}}{1+\frac{M}{2r}}\right)^2, g_{11} = g_{22} = g_{33} = \left(1+\frac{M}{2r}\right)^4 \tag{D.11}$$

where $r = \sqrt{X^2+Y^2+Z^2}$.

Non-vanishing Christoffel Symbols:

$$
\begin{aligned}
\Gamma^0_{0i} &= \frac{MX^i}{r^3}\frac{1}{1-\left(\frac{M}{2r}\right)^2} \\
\Gamma^i_{00} &= \frac{MX^i}{r^3}\frac{\left(1-\frac{M}{2r}\right)}{\left(1+\frac{M}{2r}\right)^7} \\
\Gamma^i_{kj}\,\delta^k_i &= -\frac{MX^j}{r^3}\frac{1}{\left(1+\frac{M}{2r}\right)} \\
\Gamma^i_{jj} &= \frac{MX^i}{r^3}\frac{1}{\left(1+\frac{M}{2r}\right)}\,(i\neq j)
\end{aligned}
$$

where $i, j = 1, 2, 3$.

D.3 Kerr Metric

The Kerr metric describes stationary, axisymmetric solutions to the Einstein equations of General Relativity. The Kerr metric describes a rotating black hole of mass M and specific angular momentum $a = J/M$ with an event horizon located at $r_+ = M + \sqrt{M^2 - a^2}$. Boyer-Lindquist coordinates are an extension of the Schwarzschild coordinates; the Christoffel symbols in this metric are discontinuous at the event horizon. The Kerr In-going coordinate system fixes this coordinate singularity by transforming the time coordinate and angular coordinate ϕ.

D.3.1 Boyer-Lindquist Coordinates

Coordinates: $(X^0, X^1, X^2, X^3) \equiv (t, r, \theta, \phi)$

Metric Components:

$$
\begin{aligned}
g_{00} &= -\left(1 - \frac{2Mr}{\Sigma}\right) \\
g_{03} &= -\frac{4aMr\sin^2\theta}{\Sigma} \\
g_{11} &= \frac{\Sigma}{\Delta} \\
g_{22} &= \Sigma \\
g_{33} &= \frac{A\sin^2\theta}{\Sigma}
\end{aligned}
$$

where

$$
\Delta := r^2 - 2Mr + a^2
$$

$$\Sigma := r^2 + a^2 \cos^2\theta$$
$$A := \left(r^2 + a^2\right)^2 - a^2 \sin^2\theta\, \Delta$$

Non-vanishing Christoffel Symbols:

$$\begin{aligned}
\Gamma^0_{01} &= -\frac{p\,b^2}{\Delta} \\
\Gamma^0_{13} &= \frac{a \sin^2\theta}{\Delta}\left(p\,b^2 + 2\,q\,r\right) \\
\Gamma^0_{20} = \Sigma\,\Gamma^2_{00} &= \frac{q\,a^2}{\Sigma}\sin(2\theta) \\
\Gamma^0_{32} &= -\frac{q\,a^3}{\Sigma}\sin^2\theta\,\sin(2\theta) \\
\Gamma^1_{00} &= -\frac{\Delta\,p}{\Sigma} \\
\Gamma^1_{03} &= \frac{a\,\Delta\,p \sin^2\theta}{\Sigma} \\
\Gamma^1_{11} &= \frac{r}{\Sigma} + \frac{M - r}{\Delta} \\
\Gamma^1_{12} = \Gamma^2_{22} = -\Delta\,\Gamma^2_{11} &= -\frac{a^2\,\sin(2\theta)}{2\,\Sigma} \\
\Gamma^1_{22} &= -\frac{r\,\Delta}{\Sigma} \\
\Gamma^1_{33} &= -\frac{\Delta \sin^2\theta}{\Sigma}\left(r + p\,a^2 \sin^2\theta\right) \\
\Gamma^2_{03} &= -\frac{q\,a\,b^2\,\sin(2\theta)}{\Sigma^2} \\
\Gamma^2_{12} &= \frac{r}{\Sigma} \\
\Gamma^2_{33} &= -\frac{\sin(2\theta)}{2\,\Sigma}\left[b^2 - 2\,a^2\,q \sin^2\theta\left(2 + \frac{a^2 \sin^2\theta}{\Sigma}\right)\right] \\
\Gamma^3_{01} &= -\frac{a\,p}{\Delta} \\
\Gamma^3_{02} &= \frac{2\,q\,a}{\Sigma}\cot\theta \\
\Gamma^3_{13} &= \frac{r}{\Delta}\left(1 + 2\,q\right) + a^2\,p\,\frac{\sin^2\theta}{\Delta} \\
\Gamma^3_{23} &= \frac{\cot\theta}{\Delta}\left[\left(1 + 2\,q\right)\left(b^2 - 2\,q\,a^2 \sin^2\theta\right) - 2\,q\,a^2\,b^2\,\Sigma^{-1}\sin^2\theta\right]
\end{aligned}$$

where

$$b^2 := r^2 + a^2$$

$$
\begin{aligned}
p &:= \Sigma^{-2} M \left(\Sigma - 2r^2\right) \\
q &:= (2\Sigma)^{-1} (-2Mr)
\end{aligned}
$$

D.3.2 Kerr Coordinates

Coordinates: $(X^0, X^1, X^2, X^3) \equiv (\tilde{V}, r, \theta, \tilde{\phi})$

Metric Components:

$$
\begin{aligned}
g_{00} &= -\left(1 - \frac{2Mr}{\Sigma}\right) \\
g_{01} &= -1 \\
g_{03} &= -\frac{2aMr\sin^2\theta}{\Sigma} \\
g_{13} &= -a\sin^2\theta \\
g_{22} &= \Sigma \\
g_{33} &= \sin^2\theta \frac{(r^2+a^2)^2 - \Delta a^2 \sin^2\theta}{\Sigma}
\end{aligned}
$$

where

$$
\begin{aligned}
\Delta &:= r^2 - 2Mr + a^2 + Q^2 \\
\Sigma &:= r^2 + a^2\cos^2\theta
\end{aligned}
$$

Non-vanishing Christoffel Symbols:

$$
\begin{aligned}
\Gamma^0_{00} &= Mb^2 \frac{\Sigma_-}{(\Sigma)^3} \\
\Gamma^0_{02} &= -\frac{a^2 Mr \sin 2\theta}{(\Sigma)^2} \\
\Gamma^0_{12} &= -\frac{a^2 \sin 2\theta}{2\Sigma} \\
\Gamma^0_{22} &= -\frac{b^2 r}{\Sigma} \\
\Gamma^0_{03} &= -\frac{aMb^2\Sigma_- \sin^2\theta}{(\Sigma)^3} \\
\Gamma^0_{13} &= \frac{ar\sin^2\theta}{\Sigma} \\
\Gamma^0_{23} &= \frac{a^3 Mr \sin 2\theta \sin^2\theta}{(\Sigma)^2}
\end{aligned}
$$

$$
\begin{aligned}
\Gamma^0_{33} &= -\frac{b^2\sin^2\theta}{8(\Sigma)^3}\left(a^4M+3a^4r-4a^2Mr^2+8a^2r^3+8r^5\right.\\
&+ \left.4a^2r\left(a^2+r(M+2r)\right)\cos 2\theta - a^4(M-r)\cos 4\theta\right)\\
\Gamma^1_{00} &= M\Delta\frac{\Sigma_-}{(\Sigma)^3}\\
\Gamma^1_{01} &= -M\frac{\Sigma_-}{(\Sigma)^2}\\
\Gamma^1_{12} &= -\frac{a^2\sin 2\theta}{2\Sigma}\\
\Gamma^1_{22} &= -\frac{r\Delta}{\Sigma}\\
\Gamma^1_{03} &= -\frac{aM\Delta\Sigma_-\sin^2\theta}{(\Sigma)^3}\\
\Gamma^1_{13} &= \frac{a\sin^2\theta}{(\Sigma)^2}\left(r^2(r+M)+a^2\cos^2\theta(r-M)\right)\\
\Gamma^1_{33} &= -\frac{\Delta\sin^2\theta}{8(\Sigma)^3}\left(a^4M+3a^4r-4a^2Mr^2+8a^2r^3+8r^5\right.\\
&+ \left.4a^2r\left(a^2+r(M+2r)\right)\cos 2\theta - a^4(M-r)\cos 4\theta\right)\\
\Gamma^2_{00} &= -\frac{a^2Mr\sin 2\theta}{(\Sigma)^3}\\
\Gamma^2_{12} &= \frac{r}{\Sigma}\\
\Gamma^2_{22} &= -\frac{a^2\sin 2\theta}{2\Sigma}\\
\Gamma^2_{03} &= \frac{aMrb^2\sin 2\theta}{(\Sigma)^3}\\
\Gamma^2_{13} &= \frac{a\sin 2\theta}{2\Sigma}\\
\Gamma^2_{33} &= -\frac{\sin 2\theta}{16(\Sigma)^3}\left(3a^6+10a^4Mr+11a^4r^2+16a^2Mr^3+16a^2r^4\right.\\
&+ \left.8r^6+4a^2\Delta\left(a^2+2r^2\right)\cos 2\theta + a^4\Delta\cos 4\theta\right)\\
\Gamma^3_{00} &= \frac{aM\Sigma_-}{(\Sigma)^3}\\
\Gamma^3_{02} &= -\frac{2aMr\cot\theta}{(\Sigma)^2}\\
\Gamma^3_{12} &= -\frac{a\cot\theta}{\Sigma}\\
\Gamma^3_{22} &= -\frac{ar}{\Sigma}
\end{aligned}
$$

$$
\begin{aligned}
\Gamma^3_{03} &= -\frac{a^2 M \sin^2\theta \Sigma_-}{(\Sigma)^3} \\
\Gamma^3_{13} &= \frac{r}{\Sigma} \\
\Gamma^3_{23} &= \frac{\cot\theta}{8(\Sigma)^2}\left(3a^4 + 8a^2 Mr + 8a^2 r^2 + 8r^4 + 4a^2\Delta\cos 2\theta + a^4\cos 4\theta\right) \\
\Gamma^3_{33} &= \frac{a\sin^2\theta}{(\Sigma)^3}\left(\cos^2\theta\left(2a^2 r b^2\right.\right. \\
&+ \left.\left. a^4(M-r)\sin^2\theta\right) + r\left(r^4 - a^4 + a^2(a^2 - Mr)\sin^2\theta\right)\right)
\end{aligned}
$$

where

$$
\begin{aligned}
b^2 &:= r^2 + a^2 \\
\Sigma_- &:= r^2 - a^2\cos^2\theta
\end{aligned}
$$

Appendix E

Spacetime Coordinate Transformations

This appendix lists the coordinate transformations that were used to map between various coordinate systems. These transformations were used to perform coordinate transformations for visualization of numerical data and to generate initial data for the various versions of the Von Neumann solver.

The numerical worldsheets are computed and stored in the basic coordinates of the chosen spacetime. Graphics are generated based on a 3D Cartesian box. Although the displays used in this document simply discard the time coordinate, the transformation functions map the time coordinate as well for completeness.

Some of the coodinate transformations shown here are also used to transform the initial data for the numerical solutions, which are expressed in Cartesian coordinates, to the correct spacetime coordinates used by the numerical solver.

E.1 Transformations for Schwarzschild and Boyer-Lindquist Coordinates

Schwarzschild coordinates and Boyer-Lindquist are effectively equivalent (no rotational transformation is applied in Boyer-Lindquist), so the mapping to display coordinates is simply a Spherical-Polar coordinate transformation.

The coordinates are designated as

$$(X^0, X^1, X^2, X^3) \equiv (T, R, \theta, \phi)\,, \tag{E.1}$$

and transform as

$$\begin{aligned} T &= T \\ X &= R\sin\theta\cos\phi \\ Y &= R\sin\theta\sin\phi \\ Z &= R\cos\theta\,, \end{aligned} \tag{E.2}$$

and

$$\begin{aligned} T &= T \\ R &= \sqrt{X^2+Y^2+Z^2} \\ \theta &= \arctan\frac{\sqrt{X^2+Y^2}}{Z} \\ \phi &= \arctan\frac{Y}{X}. \end{aligned} \tag{E.3}$$

E.2 Transformations for Eddington-Finkelstein In-going Coordinates

Eddington-Finkelstein In-going coordinates are slightly more complicated in that the time coordinate is remapped to an ingoing null coordinate $\tilde{V}$. The coordinates are designated as [40]

$$(X^0, X^1, X^2, X^3) \equiv (\tilde{V}, R, \theta, \phi) \tag{E.4}$$

and transform as,

$$\begin{aligned} T &= \tilde{V} - R - 2M\log\left|\frac{R}{2M}-1\right| \\ X &= R\sin\theta\cos\phi \\ Y &= R\sin\theta\sin\phi \\ Z &= R\cos\theta, \end{aligned} \tag{E.5}$$

and

$$\begin{aligned} \tilde{V} &= T + R + 2M\log\left|\frac{R}{2M}-1\right| \\ R &= \sqrt{X^2+Y^2+Z^2} \\ \theta &= \arctan\frac{\sqrt{X^2+Y^2}}{Z} \\ \phi &= \arctan\frac{Y}{X}. \end{aligned} \tag{E.6}$$

E.3 Transformations for Kerr In-going Coordinates

Kerr In-going coordinates are slightly more complicated still, remapping both the time coordinate to an ingoing null coordinate $\tilde{V}$ and transforming to a co-rotating frame of reference. The coordinates are designated as [40]

$$(X^0, X^1, X^2, X^3) \equiv (\tilde{V}, R, \theta, \tilde{\phi}), \tag{E.7}$$

and transform as

$$\begin{aligned} T &= \tilde{V} - R - M\log|\Delta| \\ &- \frac{M^2}{\sqrt{M^2-a^2}}\log\left|\frac{R-M-\sqrt{M^2-a^2}}{R-M+\sqrt{M^2-a^2}}\right| - M\left(1-\log|4M^2|\right) \\ X &= R\sin\theta\cos\phi \\ Y &= R\sin\theta\sin\phi \\ Z &= R\cos\theta, \end{aligned} \tag{E.8}$$

where $\Delta := R^2 - 2MR + a^2$ and

$$\phi = \tilde{\phi} - \frac{a}{2\sqrt{M^2-a^2}}\log\left|\frac{R-M-\sqrt{M^2-a^2}}{R-M+\sqrt{M^2-a^2}}\right|. \tag{E.9}$$

These transformations are derived by integrating the infinitesimal relations [40]

$$\begin{aligned} d\tilde{\phi} &= d\phi + \frac{a}{\Delta}\,dr \\ d\tilde{V} &= dT + \frac{r^2+a^2}{\Delta}\,dr\,. \end{aligned} \tag{E.10}$$

It can be readily verified that these transformations reduce to those for EFI coordinates in the limit $a \to 0$.